Sebastian Klamor

Production of Neutral Pions in Ultra-Relativistic d+Au Collisions Measured by the PHENIX Experiment

— 2010 —

Experimentelle Physik

Production of Neutral Pions in Ultra-Relativistic d+Au Collisions Measured by the PHENIX Experiment

Diplomarbeit
vorgelegt von
Sebastian Klamor

Westfälische Wilhelms-Universität
Institut für Kernphysik
— 2010 —

Contents

1. Introduction

"A prima descendit origine mundi causarum series."
"The chain of causes dates back to the first origin of the world."

Lucanus, Bellum civile (Pharsalia) 6. 611-612

The origin of the world and the development from the big bang to the earth as we know it today has been and is subject of scientific research. One interesting aspect of today's research are the conditions of matter shortly after the big bang. It is expected that an unusual state of matter, a so-called *Quark Gluon Plasma* (QGP), has existed the first microseconds after the big bang, in which quarks and gluons are the relevant degrees of freedom.
Heavy ion physics offers the possibility to study matter under these extreme conditions characterised by high densities, temperatures, and pressures. In particle colliders, heavy ions, for example of lead or gold, are accelerated at high energies and collided. In these collisions a possible QGP can be created and examined.
The PHENIX[1] experiment at RHIC[2] investigates such heavy ion collisions via the measurement of particle production for various types of collision: Au+Au, p+p, Cu+Cu, d+Au, and different centre-of-mass energies.
The comparison of particle production in different reaction systems gives evidence for the existence of a QGP. One of the key signatures was the observation of a suppression of particles with high transverse momentum in central Au+Au collisions compared to peripheral collisions and to expectations from p+p results [Adc02, Adl03c]. This effect is expected to originate from energy loss of hard scattered partons in a hot and dense medium. However, particle production is also influenced by effects of cold nuclear matter. To study such possible effects, deuteron-gold collisions are analysed. They offer an insight to the nuclear structure function and provide a useful baseline for Au+Au collisions.
This thesis contains an analysis of neutral pion production in d+Au collisions at $\sqrt{s_{\mathrm{NN}}} = 200$ GeV. The data is taken from the RHIC Run 8 in 2008 which offers a 30 times increase in the integrated luminosity and thus in the total number of sampled events compared to Run 3 in 2002/2003. This reduces statistical uncertainties,

[1] **P**ioneering **H**igh **E**nergy **N**uclear **I**nteractions e**X**periment
[2] **R**elativistic **H**eavy **I**on **C**ollider

especially at high transverse momenta.

This thesis is organised as follows. First, some basics of nuclear matter and quantum chromodynamics with a focus on QGP are presented in Chapter 2. Moreover, ultra-relativistic collisions and possible signatures of a QGP are outlined. In Chapter 3, the setup of the PHENIX experiment and some basic detection principles are explained. Chapter 4 contains the information on processing the measured data. The different analysis steps which lead to the spectra of neutral pions are presented in Chapter 5. The final results of this analysis are summarised and discussed in Chapter 6. Finally, a summary of the main results is outlined in Chapter 7.

2. Theoretical Background

2.1 Basic Constituents of Matter

At the beginning of the 20th century, the modern model of the atom, consisting of a dense core surrounded by an electron cloud, was developed. In general, this point of view was experimentally established by Rutherford, Geiger, and Marsden (1911-1913) who scattered helium nuclei (α-particles) off a gold foil and confirmed the existence of a positively charged region, the nucleus, where the majority of the atomic mass is concentrated [Gei13]. In 1919, Rutherford proved the proton to be the positive component of the nucleus. The picture of the nucleus was completed in 1932 when Chadwick detected the neutral component of the nucleus: the neutron [Cha32]. Moreover, the postulation of the neutrino was made in 1930 to save the conservation laws of energy, momentum, and angular momentum for the β-decay. It was thought that all elementary particles had been determined, until particle accelerator physics in the late 60s and 70s offered a more detailed view of the basic constituents of matter. Deep inelastic scattering experiments exposed that the nucleons, i.e. protons and neutrons, themselves are a composition of smaller particles, the so-called quarks [Pov06].

The Standard Model

The fundamental interactions and basic structures of matter can be well described within the *Standard Model* (SM). In the SM, there are two fundamental groups of components of matter:
On the one hand, there are the *leptons*, including the electron and neutrino. On the other hand, there are the *quarks*. Both groups are fermions because they have spin 1/2, in units of $\hbar$. Gell-Man and Zweig introduced the idea of the quarks being the fundamental component of which *hadrons*, subdivided in *baryons*[1] and *mesons*[2], are formed [GM64, Zwe64a, Zwe64b].
Every particle has an anti-particle with the same properties in mass and spin and opposing additive quantum numbers, e.g. the charge, the baryon number, and lepton

[1] Baryons consist of three quarks.
[2] Mesons consist of a quark and an anti-quark.

	particles	**charge**	**mass**	**spin**
1st Generation	e	-1 e	0.511 MeV/c^2	$\frac{1}{2}$
	ν_e	0	$\leq$ 2.3 MeV/c^2	
2nd Generation	μ	-1 e	105.658 MeV/c^2	$\frac{1}{2}$
	ν_μ	0	$\leq$ 0.19 MeV/c^2	
3rd Generation	τ	-1 e	1776.840 MeV/c^2	$\frac{1}{2}$
	ν_τ	0	$\leq$ 18.2 MeV/c^2	

Table 2.1: Properties of leptons [APDG09].

	quark flavours	**charge**	**mass**	**spin**
1st Generation	u	$\frac{2}{3}e$	$1.5 - 3.3$ MeV/c^2	$\frac{1}{2}$
	d	$-\frac{1}{3}e$	$3.5 - 6.0$ MeV/c^2	
2nd Generation	c	$\frac{2}{3}e$	$1.16 - 1.34$ GeV/c^2	$\frac{1}{2}$
	s	$-\frac{1}{3}e$	$70 - 130$ MeV/c^2	
3rd Generation	t	$\frac{2}{3}e$	171.3 GeV/c^2	$\frac{1}{2}$
	b	$-\frac{1}{3}e$	$4.13 - 4.37$ GeV/c^2	

Table 2.2: Quark flavours, charges and masses [APDG09].

number. The SM is built up of 24 elementary fermions, as far as we know today. In contrast to atoms, nuclei, and hadrons, no states of excitation of the fundamental fermions are known. They appear to be elementary particles and are grouped into three generations, in ascending masses, as shown in Table 2.1 and Table 2.2.
Besides the fundamental particles there are four fundamental interactions: the *strong interaction*, the *weak interaction*, the *electromagnetic interaction*, and the *gravitation*. The gravitation is not part of the SM. An overview of the four forces is presented in Table 2.3.

Forces between particles are mediated by gauge bosons (gluons, photons, $W^{\pm}/Z^0$-bosons, and gravitons; see Table 2.3). The gauge boson of the gravitational force, the graviton, has not yet been discovered. In the SM, leptons only interact through the weak interaction and, if they are charged, through the

form of interaction	**gauge boson**	**mass** (Gev/c^2)	**Spin**
strong	8 gluons (g)	0	1
electromagnetic	Photon (γ)	0	1
weak	W^+-boson	80.4	1
	W^--boson	80.4	1
	Z^0-boson	91.2	1
gravity	graviton	0	2

Table 2.3: The four fundamental interactions and their properties.

electromagnetic force. The quarks interact through the weak, electromagnetic, and the strong interaction. Gravitation is not included in the standard model. Furthermore, the standard model includes the theory of the electroweak interaction. This theory describes the electromagnetic and weak force as two aspects of a uniform interaction, developed by Salam and Weinberg [Cot07].

2.2 QCD and Quark Gluon Plasma

2.2.1 Quantum Chromodynamics

Constituents of an atomic nucleus are protons and neutrons which in turn consist of partons (quarks and gluons). Gluons are the force-carrying particles of the strong force. The theory that describes the strong interaction is quantum chromodynamics (QCD). In general, its structure is comparable to the theoretical description of the electromagnetic interaction, quantum electrodynamics (QED). Photons mediate the electromagnetic force between charged particles in QED. In contrast, in QCD there are eight different gluons which carry the strong force and mediate between *colour charged* particles. Thus quarks have, in addition to the flavour degrees of freedom (see Table 2.2), also the colour degrees of freedom (red, green, blue) [Nam60, Gre64]. Anti-quarks carry anti-colour. A striking difference between QED and QCD are the properties of its gauge bosons. Whereas the photon is neutral in charge and is thus not subject to the electromagnetic force, the gluons carry colour and anti-colour and can interact among themselves. The theoretical motivation for this can be found in the colour SU(3) algebra for QCD and the U(1) algebra for QED, for more detailed

information see [Yan54]. Another argument for the new quantum number colour is Pauli's exclusion principle which predicts a total anti-symmetric wave function for identical fermions. Regarding the Baryon $\Delta^{++} = |u^{\uparrow}u^{\uparrow}u^{\uparrow}\rangle$ which shows a symmetric spin, spatial, and flavour wave function, all quarks and their quantum numbers look identical except for the colour which causes a total anti-symmetric wave function and saves the Pauli exclusion principle.

Confinement in QCD describes the phenomenon that single colour charged particles cannot be directly observed. Therefore, only combinations of quarks which are colour neutral can exist. The quarks are confined in colour neutral hadrons. All three colours are represented in baryons and result in a colourless (white) particle, whereas quark and anti-quark in mesons carry colour and the associated anti-colour.

Two important characteristics of quark-gluon dynamics are provided by QCD. The strong interaction becomes weak at high energies or low distances while at low energies and high distances the interaction becomes strong. This phenomenon is described as the *asymptotic freedom* and was introduced by Gross, Wilczek and Politzer [Gro73, Pol73]. In first order of the QCD perturbation theory[3], the coupling between two quarks, depending on the momentum transfer Q^2, can be described as:

$$\alpha_s(Q^2) = \frac{12\pi}{(33 - 2n_f) \cdot \ln(\frac{Q^2}{\Lambda^2})}, \tag{2.1}$$

where n_f represents the number of involved quark flavours ($3 \leq n_f \leq 6$) and Λ represents a scale parameter in QCD.

The confinement of quarks in hadrons can be described via the potential of a quark-anti-quark pair. This potential can be approximated with:

$$V_{q\overline{q}} = -\frac{4}{3}\frac{\alpha_s(r)}{r} + k \cdot r \ . \tag{2.2}$$

The formula describes the asymptotic behaviour of the potential $\mathrm{V}(r \to 0) \propto 1/r$ and $\mathrm{V}(r \to \infty) \propto \infty$. The factor of 4/3 is a result of three possible quark colours. The field between two quarks is formed like a string due to the interaction between gluons. At long distances the string breaks and the generation of a new quark-anti-quark pair and two strings takes place. From this point of view the constant k in Equation 2.2 can be interpreted as a string tension.

At short distances, the quarks can be regarded as quasi-free particles due to asymptotic freedom and at long distances an infinite amount of energy is necessary for the

[3]This is valid for $\alpha_s \ll 1$ or $Q^2 \gg \Lambda^2$, respectively; for calculations with lower momentum transfers *lattice gauge theory* is used.

separation of a quark-anti-quark pair [Pov06, Yag05].
Another important aspect of QCD is the interpretation of mass differences between quarks and hadrons that will be briefly discussed in the following. Here, a fundamental property of QCD, the so-called chiral symmetry, plays an important role. Quarks show a mass of a few MeV and can be approximated as massless particles. Exact chiral symmetry implies that only quarks with the same chirality or helicity[4] can interact. Thus left and right handed fermions remain left and right handed in all reference systems. The emission and absorption of gluons leaves the chirality unchanged which implies a conservation of the number of baryons B_{R} for right handed quarks and B_{L} for left handed quarks. The chiral symmetry is *explicitly* broken because quarks do have a finite mass and only the number of quarks $B = B_{\mathrm{R}} + B_{\mathrm{L}}$ is conserved. An important aspect for the understanding of the hadron masses is the ground state of the vacuum [Kha02]. In the ground state of the vacuum, the expectation value of $\langle q\overline{q}\rangle$ becomes non vanishing. It is unstable against the production of quark-anti-quark pairs because of the attractive force between quarks and anti-quarks. More precisely, the non vanishing value implies that left and right handed quarks and anti-quarks can be converted into each other. This is denoted as the spontaneous breaking of the chiral symmetry because the Lagrangian does not explicitly have this property [Rey04, BM09]. This phenomenon is similar to a ferromagnet where a macroscopic magnetisation appears below a critical temperature. It was first recognised in QCD by Nambu [Nam60, Nam61a, Nam61b].
A more detailed description can be found in [Tho01].

2.2.2 Quark-Gluon Plasma

At high temperatures and/or densities a phase transition occurs. In this new phase of matter, the quarks and gluons become the relevant degrees of freedom and are not confined in hadrons anymore. This new state of matter is called Quark-Gluon-Plasma (QGP).
At the phase transition and in the QGP close to the phase transition, the scale of α_s is ≈ 1. Therefore, it is not possible to perform the perturbation theory to describe the phase transition, instead one models the QCD processes with a discrete space-time lattice, introduced by Creutz [Cre77]. Lattice calculation for a vanishing

[4]The helicity is the projection of the spin s on the direction of the momentum of a particle. If the spin is parallel to the momentum, the particle is called *right handed* and if the spin is anti-parallel to the momentum, the particle is called $left$ *handed*.

baryochemical potential μ_b, in particular for equal numbers of baryons and anti-baryons, predict the dependence of the temperature of thermodynamic quantities [Kar02]. In this context a reduced energy density ϵ/T^4 is used to compare deviations from an ideal gas which is described by the Stefan-Boltzmann-law. Results from lattice gauge theory calculations show a phase transition from hadronic matter to QGP at a certain critical temperature[5] $T_c \approx 175$ MeV as a sudden rise in the energy density ϵ/T^4 (see Figure 2.1). The associated critical energy density $\epsilon(T_c)$ is denoted as 700 ± 300 MeV/fm^3 which is in terms of energy densities of heavy nuclei roughly five times higher. Moreover, the broken chiral symmetry is expected to be restored near T_c [BM09].

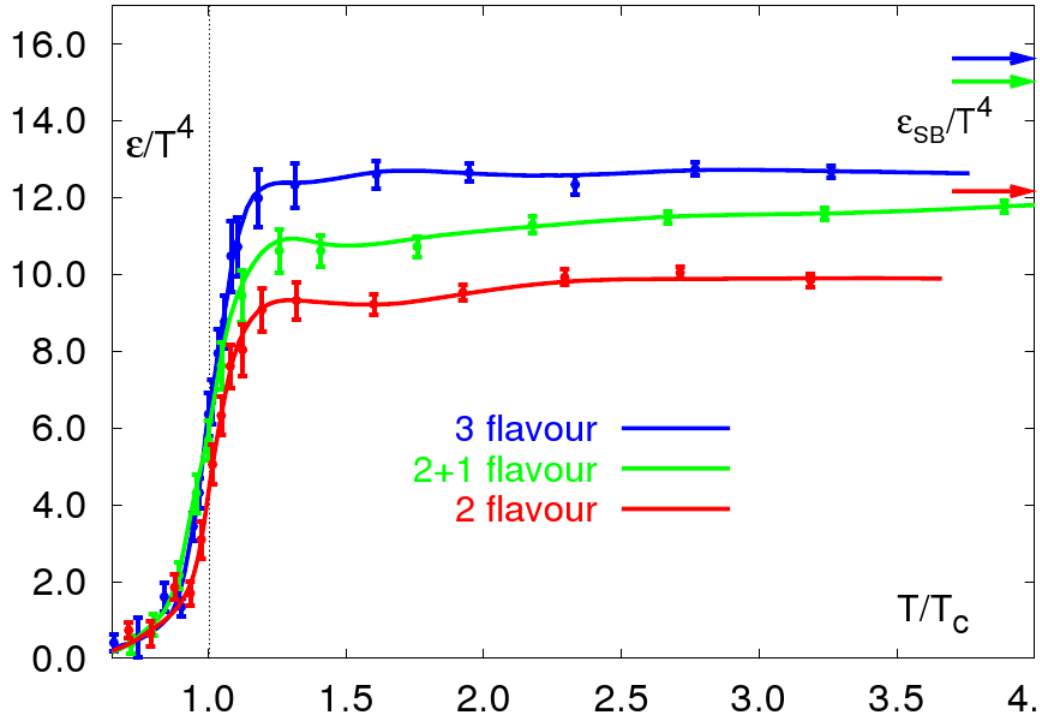

Figure 2.1: Results from a lattice QCD calculation from [Kar02]. The Phase diagram depicts the dependence of the energy density ϵ on the temperature for three different quark configurations. The Stefan Boltzman limit, i.e. the expectations for an ideal gas with gluon and quark degrees of freedom, is also shown.

The formation of a QGP at high temperatures (*hot* QGP) can be described as follows: The QCD vacuum in a certain spatial area is heated. Hadrons are thermally

[5] In this thesis, temperatures T are multiplied by the Boltzmann constant $k = 8.617 \cdot 10^{-5}$eV K^{-1}. For example a temperature of 50 MeV is $\approx 1.16 \cdot 10^{11}$ K.

excited from the vacuum. The generated hadrons are mainly light mesons, i.e. pions. Because of the limited area, the hadrons, which are all roughly of the same size (1 fm), start to overlap at a critical temperature T_c. Above this critical temperature the hadronic system dissolves into a system of quarks and gluons with equal numbers of quarks and anti-quarks ($\mu_b = 0$).
A *cold* QGP can be produced via adiabatic ($\Delta T = 0$) compression of hadronic matter. Baryons start to overlap and at a critical baryon density a system of quarks and gluons where the number of quarks is larger than the number of anti-quarks is formed [Yag05].
The phase diagram for finite baryon densities is determined via the bag model[6] because lattice calculation for finite baryon densities $\mu_b > 0$ turn out to be difficult [Kar00].
The phase diagram for hadronic matter as a function of the baryon density μ_b and the temperature T is shown in Figure 2.2. The sketch shows the transition of hadronic matter into the deconfined state, the QGP. The dotted line implies a crossover in the phase transition until it reaches the critical point for increasing baryon density and decreasing temperature. At this point a phase transition of second order is expected. For further increasing baryon densities, a phase transition of first order occurs [Rey04, Yag05, BM09].
The QGP is expected to have occurred and to occur in three places:

1. the early universe,
2. in the core of neutron stars,
3. in ultra-relativistic heavy ion collisions.

The deconfined phase of matter is expected to have existed at some 10 picoseconds after the cosmic big bang and lasted 10 microseconds (1) [BM07]. Nowadays, the QGP is expected to exist in the core of neutron stars where high densities exist (2), but it is also out of reach for direct experimental studies. The tool to form and study the QGP are heavy ion collisions at ultra-relativistic energies (3). The energy regimes are reached in colliding heavy ions and are experimentally realised at the Relativistic Heavy Ion Collider (RHIC) at BNL and the Large Hadron Collider (LHC) at CERN.

[6]The (MIT) bag model describes hadrons as a bag where partons are confined. For more details see [Cho74, Won94, BM96].

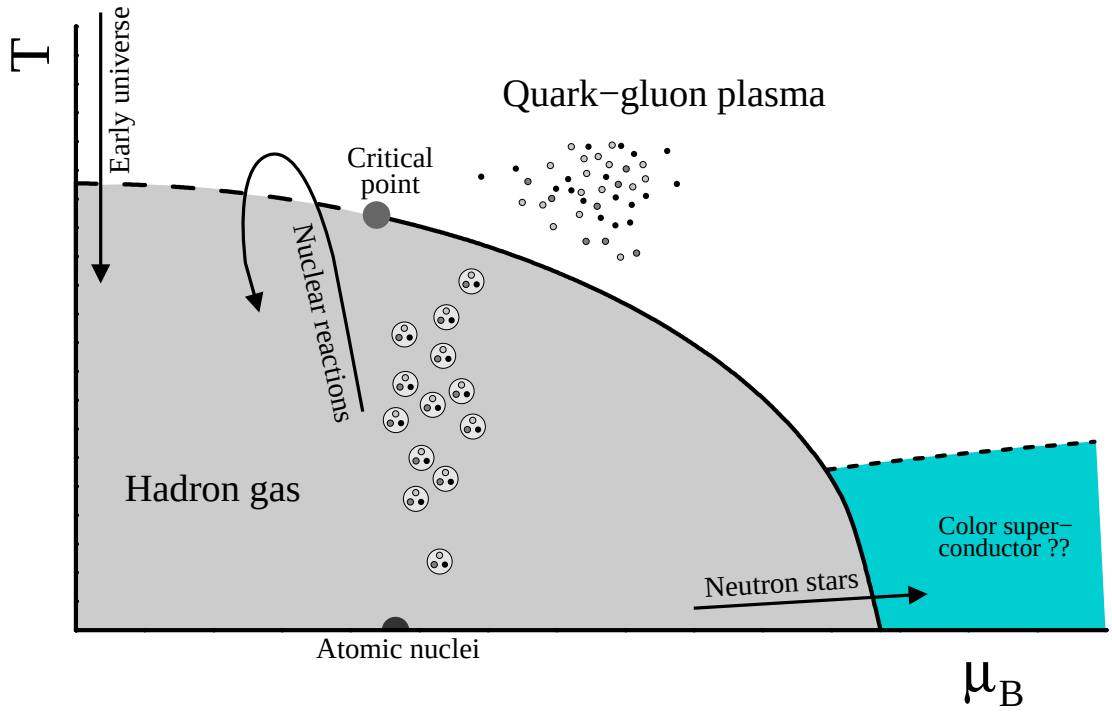

Figure 2.2: A sketch of the predicted phase diagram. A crossover phase transition is expected to occur for low baryon densities μ_b and high temperatures. The phase transition for high baryon densities and lower temperatures the phase transition is of first order. For even larger baryon densities phenomena like colour superconductivity could appear [KB04].

2.3 Ultra-Relativistic Heavy Ion Collisions

In this diploma thesis, ultra-relativistic nucleus-nucleus collisions are studied. Therefore, it is essential to understand and explain the processes in nucleon-nucleon collisions. Phenomenological extrapolations of nucleon-nucleon collisions are necessary for comparisons and expectations for heavy ion collisions.
Reactions with a centre-of-mass energy $\sqrt{s_{\mathrm{NN}}} \geq 10$ GeV are called *ultra-relativistic*.

2.3.1 Nucleon-Nucleon Collisions

In nucleon-nucleon collisions, no high energy densities that would lead to the formation of a QGP are expected. An important parameter of each collision is the total cross section σ_{tot}. The total cross section is composed of an elastic and inelastic part whereas the inelastic cross section is much larger than the elastic for $\sqrt{s_{\mathrm{NN}}} > 1$ GeV. Moreover, the total cross section changes little for higher values for

the centre-of-mass energy $\sqrt{s}$ in p+p collisions and has a value of about $\sigma_{tot} \approx 40$ mb above $\sqrt{s} \approx 10$ GeV [Cas98].
In the collision process, the nucleons lose a large fraction of their energy which is used to produce particles. An inelastic reaction therefore is characterised by particle production, dominated by pion production (80-90% of the produced particles). The remaining particles produced in inelastic collisions are heavier mesons, baryons, anti-baryons, and other particles. The total number of particles produced in a collision is called the *multiplicity* of a collision.
Among the produced particles, the production of particles is separated in *soft* and *hard* processes. These processes are characterised by the observable transverse momentum[7] p_{T}. In soft processes, which dominate the multiplicity of a collision, the produced particles have roughly a transverse momentum of $p_{\mathrm{T}} < 2$ GeV/c. The total Lorentz-invariant cross section[8] $\frac{\mathrm{d}\sigma}{\mathrm{d}p_{\mathrm{T}}^2}$ of soft processes can be parametrised with an exponential function:

$$\frac{\mathrm{d}\sigma}{\mathrm{d}p_{\mathrm{T}}^2} \sim \exp(-\frac{p_{\mathrm{T}}}{T}) \qquad \text{with} \;\; T \approx 160 \text{ MeV}. \tag{2.3}$$

On the other hand, there are *hard* processes where particles are produced with $p_{\mathrm{T}} > 2$ GeV/c. These realms cannot be described as in Equation 2.3. Hard processes can be parametrised with a power law instead:

$$\frac{\mathrm{d}\sigma}{\mathrm{d}p_{\mathrm{T}}^2} \sim p_{\mathrm{T}}^{-n}. \tag{2.4}$$

In this context, it is important to emphasise the difference between the description of soft and hard processes. Soft processes, with low Q^2, belong to the realm of nonpertubative QCD, because the quarks inside the hadron cannot be treated as asymptotically free, while hard processes with large Q^2 are well described by pertubative QCD. Due to the difficulty in describing nonpertubative dynamics in QCD, phenomenological models are used, e.g string fragmentation models [Won94]. These models are equal to the depictions in Section 2.2.1 whereas in nucleon-nucleon collisions, strings are built in form of quarks and diquarks ($q - qq$). They fragment into new particles with increasing distance. For hard particle productions, the description can be based on elementary parton-parton processes and the inelastic cross section can be described as a convolution of the parton distribution function of the collid-

[7] For the definition of the transverse momentum, see Appendix A.
[8] The definition of the invariant cross section is given in Appendix B.

ing nuclei (PDF), the non-pertubative fragmentation function (FF) of the scattered partons, and pertubative parton-parton scattering (pQCD calculation):

$$E\frac{\mathrm{d}^3\sigma^{\mathrm{hard}}}{\mathrm{d}p^3} = \int PDF \otimes pQCD \otimes FF. \tag{2.5}$$

The partons in the colliding nucleons scatter and interact via gluon or quark exchange and disperse with high energy and large scattering angles about 180°, i.e. large p_{T}, before they fragment in a narrow cone of hadrons, so-called *jets*.

For comparing the cross section of different particle species the transverse mass is introduced:

$$m_{\mathrm{T}} = \sqrt{p_{\mathrm{T}}^2 + m_0^2}. \tag{2.6}$$

The parametrisation of particle spectra with a function depending on the transverse mass shows an identical shape for different particle species. This is the so-called m_{T}-scaling.

2.3.2 Development of Heavy Ion Collisions

Collisions of heavy ions can be regarded as a superposition of nucleon-nucleon collisions and the wave-like properties of particles become negligible above $\sqrt{s} = 10$ GeV. A collision is characterised by the impact parameter b which separates the Lorentz-contracted[9] nucleons of the colliding nuclei into two groups:
Nucleons lying in the geometrical overlap region are called *participants* and nucleons which are arranged outside the overlap region are denoted as *spectators*. Furthermore, the measured energy of the spectators gives information about the parameter b. The participant-spectator model is shown in Figure 2.3. This model implies that only the participants take part in the collision and that the released energy due to the collision process produces a hot and dense fireball in the overlap region. The evolution of this created medium is described from two points of view which are characterised by the nuclear *stopping* [Bus84, Bow86]. On the one hand, the reaction with a centre-of-mass energy of $\sqrt{s} = 5 - 10$ GeV, is described by the Landau scenario. In this scenario, the participants are completely stopped and a fireball with high baryon density is produced. On the other hand, there is the Bjorken scenario [Bjo83]. The participants become transparent for each other if the centre-of-mass

[9]Objects appear contracted in length for the spectator dependent on the object's velocity.

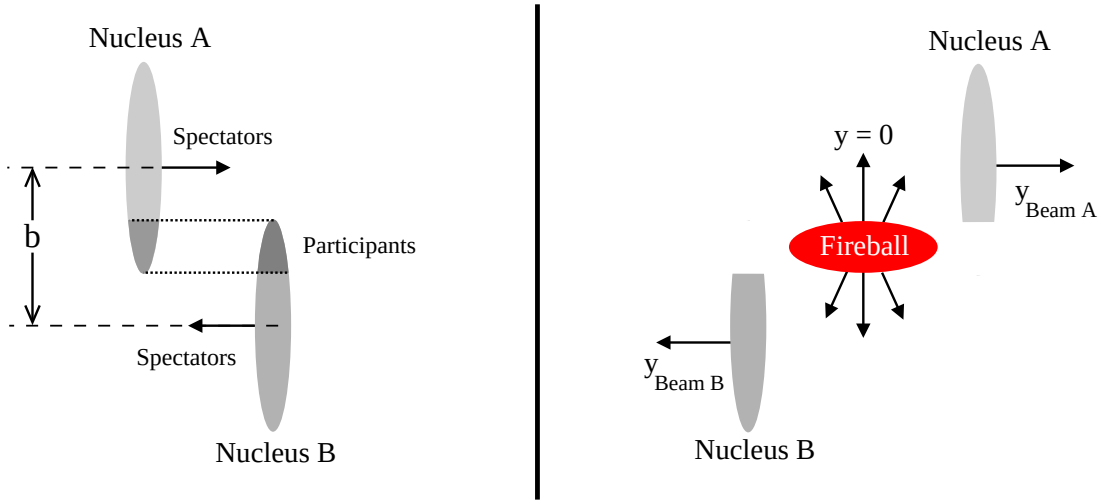

Figure 2.3: The sketch shows the geometrical participant-spectator model with the schematic development of the collision of Lorentz-contracted nuclei. The impact parameter b is the distance between the centres of the nuclei. The rapidity directions of the generated fireball and nuclei are shown [KB04].

energy is above $\sqrt{s} = 100$ GeV. For this condition the stopping is limited and the participants can interpenetrate. A fireball with low baryon density and high temperature is produced. The two different scenarios can also be distinguished through the rapidity[10] distribution of produced particles. For the Landau scenario a maximum at mid-rapidity is expected while the Bjorken scenario predicts a flat rapidity distribution in the region between the rapidity of the two colliding nuclei (see Figure 2.4). The space-time evolution of the fireball will be briefly described in the following. As discussed above, the colliding nucleons are stopped and the transformation of the energy into particle production takes place. The reaction zone is characterised by high temperature and particle density. In the beginning, the fireball is in the state of preequilibrium and additional partons from quark and gluon interactions are created. Further interactions lead to a thermalisation of the fireball and a QGP is generated. The pressure in the QGP rises because of additional interaction of the partonic matter. Thus the system expands and cools down. The quarks start to recombine into hadrons, the so-called *hadronisation*, and further expansion finally causes the *freeze-out* where the hadrons completely decouple and do not interact

[10] See Appendix A.

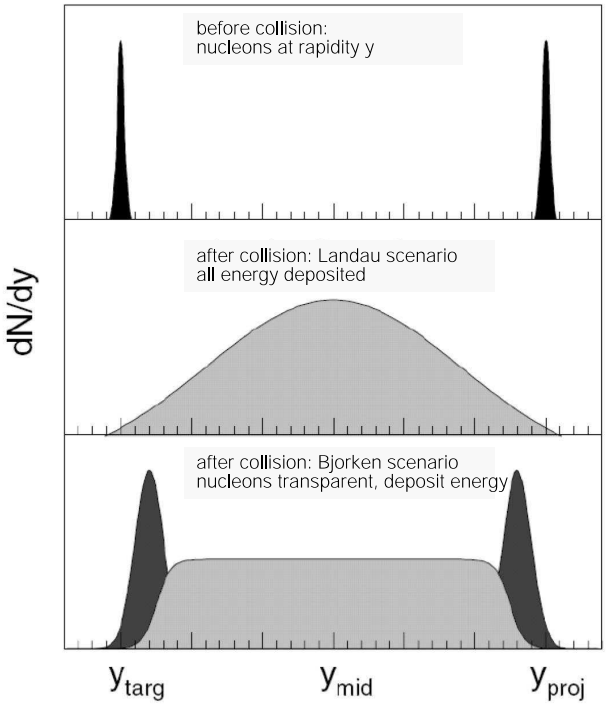

Figure 2.4: The rapidity distribution in the Bjorken and Landau scenario [Wes09].

with each other anymore. A mixed phase is expected to occur in the process of hadron gas formation where also domains of QGP co-exist. A sketch of the space-time evolution is shown in Figure 2.5. The created fireball in nuclear collisions in the

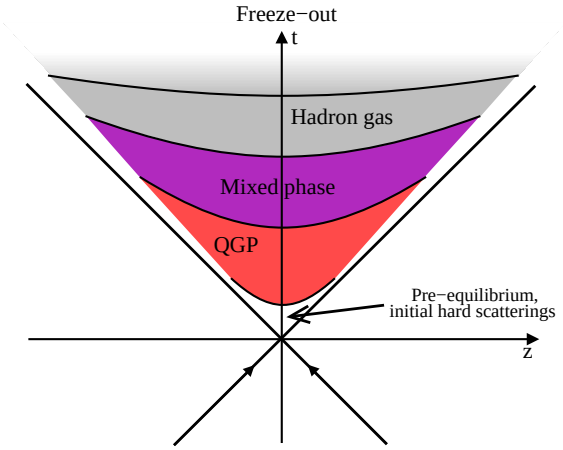

Figure 2.5: Sketch of the space-time evolution of a nucleus-nucleus collision [KB04].

laboratory lives much shorter and has lower energies compared to the deconfined state of matter in the early universe. The QGP phase transforms back into confined (hadronic) matter only after 10^{-22} s [BM07].

2.4 Signatures and Variables

To detect the deconfined phase of the QGP, different signatures can be measured. The detection of products of the interaction are useful diagnostic tools. In general, no single unique signal exists which provides an unobjectionable identification of the QGP phase. Therefore, one needs to observe as many possible products emitted during the evolution of a collision, i.e. particles and radiation, and reconstruct the formation processes via the measured data. Single signatures can also appear in a hadron gas and thus only the sum of all signatures provides an acceptable identification of the production of a QGP.
Hadrons cover useful information about the early collision process. Nevertheless they are afflicted with final state and initial state interactions which mask information about the early phase. This will be a major part of this thesis and will be presented in Section 2.6. The several signatures will be discussed in the following.

2.4.1 Photons and Leptons

Photons and leptons are a good probe to examine the interior of a hot plasma because they are not affected by the strong force and can basically escape the reaction zone without any further interaction.
In particular, photons are divided into *direct photons* and *decay photons*. Decay photons are mainly generated by the 2γ decay of the light mesons π^0 and η. Direct photons consist of prompt photons, mainly produced in quark-gluon Compton scattering $qg \rightarrow \gamma q$ and quark-anti-quark annihilation $q\bar{q} \rightarrow g\gamma$, and of thermal photons which are generated by the thermalised QGP. Prompt photons become the significant part of direct photons for high transverse momenta whereas thermal photons are dominant at small p_{T}. Additional direct photons can be produced by interaction of the jets with the surrounding medium in terms of emission of Bremsstrahlung which complicate a direct photon analysis, for a more detailed description see [KB04]. However, not only a possibly created QGP is emitting thermal photons, a hadron gas is also a source of thermal photons. So, the spectra of direct photons of QGP and hadron gas are very similar and thus cannot be a good signature on their own. A principle measurement of the temperature of the medium with thermal photons is very difficult because of the changes in temperature in different phases.
Leptons, especially dileptons, are produced by quark-anti-quark annihilation $q\bar{q} \rightarrow l^+l^-$. To use dileptons as a signal for the deconfined phase, the production

must be distinguished from other processes resulting in dilepton production, e.g. the Drell-Yan process [Dre70], the decay of charm particles, or from other hadrons and resonances. Hence, the yield of dileptons from quark-anti-quark annihilation must be greater or comparable to dileptons yields from non-QGP sources, for more information see [Won94].
Dileptons also allow the study of neutral vector mesons, such as $\rho, \omega, \Phi, J/\Psi$ which can also be used as a probe for the QGP.

2.4.2 Charm and Strange Quarks

In heavy ion collisions where a QGP might be generated, an enhancement of strangeness is expected. This is due to the production of $s\bar{s}$ pairs via gluon fusion where the energy threshold for $gg \rightarrow s\bar{s}$ is about 200 MeV [Yag05]. Compared to hadronic matter, the production of strangeness has a higher threshold of about 700 MeV, e.g in the nucleon reactions $p + p \rightarrow p + K^+ + \Lambda^0$ or $p + n \rightarrow n + K^+\Lambda^0$. Thus the production of hadrons consisting of light quarks u and d instead of s quarks has a higher probability for hadronic matter.
For the condition of deconfinement, a suppression of J/Ψ is predicted for RHIC energies. J/Ψ particles are produced in the initial state in nucleus-nucleus collisions. If a QGP is formed, the bound state of $c\bar{c}$ will be broken and the string tension becomes zero. Charm and anti-charm quark just show the *Coulomb-type* colour interaction. In this context, the Debye screening[11] becomes important to describe the phenomenon of screening c quarks by other gluons and quarks of the QGP. The Debye screening length[12] λ_D is inversely proportional to the temperature and therefore decreases with increasing temperature. Hence, at high temperatures the range of interaction between c and $\bar{c}$ becomes so small that no bound state can be formed [Won94]. Finally, the charm and anti-charm quarks hadronise in mesons with light quarks, e.g $D(c\bar{u}$ and $c\bar{d})$ or $\bar{D}(\bar{c}u$ and $\bar{c}d)$. The result will be a suppressed final yield of J/Ψ in the presence of a QGP. Nevertheless, the charm production depends on the energy of a collision. Thus at LHC energies more charm-anti-charm quarks will be produced and the probability for a c quark to find a partner $(\bar{c})$ at freeze-out will be much higher than at RHIC energies [BM07]. Thus an J/Ψ enhancement is expected to occur at LHC energies.

[11] Screening of an electromagnetic field in a plasma caused by the presence of electric charges.
[12] Length or distance over which charge separation can appear.

2.4.3 Hydrodynamic and Kinematic Signatures

Thermodynamic variables like entropy, energy density, and pressure as a function of baryochemical potential and temperature show characteristics reflecting the phase transition.
A crucial feature of a phase transition in QCD is the change in the number of degrees of freedom. This affects the dependence of the energy density on the temperature. To estimate the entropy, energy density, and temperature, the average transverse momentum $\langle p_{\mathrm{T}} \rangle$ as a function of the hadron multiplicity dN/dy at mid rapidity and the transverse energy dE_T/dy is determined.
The hydrodynamic collective flow of particle production due to the pressure gradient in the reaction zone covers information about the condition of hadronic matter in comparison to theoretical predictions. The study of the collective flow provides information about the equation of state of the produced medium. Particularly modifications in the flow behaviour due to an arising pressure gradient in the medium, e.g. the elliptic flow, can be studied to determine the equation of state and hydrodynamical properties.
In addition the space-time structure of the reaction zone can be investigated via the Hanbury Brown-Twiss interferometry (HBT) of identical particles.

2.4.4 Restoration of Chiral Symmetry

The restoration of the chiral symmetry is another probe for a phase transition. Here the phenomena of broken chiral symmetry up to the critical energy density are used, as described in Section 2.2.1. The creation of the so-called disoriented chiral condensate (DCC) can be a possible signature for the restoration of chiral symmetry. If a transition of a QGP back to hadronic matter takes place, an energetic unfavourable state can be populated in the DCC compared to usual nuclear matter. Signatures for the occurrence of the disoriented chiral condensate is the ratio of the distribution of pions (π^+, π^-, π^0) which differ from the usual value $\pi^X/(\pi^+ + \pi^- + \pi^0) \approx 1/3$. Further, a modification of the masses and widths of the vector mesons $\rho, \omega,$ and Φ, detected via their decay channel in $e^- e^+$, can provide another direct link for the restoration of the chiral symmetry [Pei97].

2.5 Jets and Jet Quenching

Initial state particle production with high transverse momentum in a parton-parton collision can be used as a signature for a formation of a QGP. As discussed in Section 2.3.1, different particles are produced in so-called *jets* where a large fraction is built by pions. If the energy density is high enough and a QGP is created, the scattered partons have to travel through the medium. Reactions take place due to the strong force resulting in a suppression of particle production (*jet quenching*) and distortion of the back-to-back correlation of jets. In more detail, the partons lose energy via interaction with other partons. The effect of energy loss depending on the path length of the parton in the medium can be described in analogy to the occurrence of Bremsstrahlung in QED. During the transition of the medium, the quark loses energy via gluon radiation. If the distances between the scattering centres become small, multiple scattering takes place before the gluon has left the first scattering partner. Hence, destructive interference causes suppression of the energy loss. Additionally, the Landau-Pomeranchuk-Migdal (LPM) effect influences the energy loss depending on the passed path length L. The gluon gets additional transverse momentum which increases with path length and therefore the coherence length decreases and less gluons interfere. In consequence, the energy loss shows a quadratic dependence on the path length L [Bai97a, Bai97b, Gyu94].
Thus the tomography of hadron jets offers information on the properties of the produced medium (see Figure 2.6).

2.5.1 Nuclear Modification Factor

An access to a quantitative analysis of the particle production and possible suppression gives the nuclear modification factor R_{AB}.
The parameter R_{AB} is the ratio of number of particles $\mathrm{d}N^h_{AB}$ for different transverse momentum in a collision of nuclei A and B, normalised to the number of particles in proton-proton collisions $\mathrm{d}N_{pp}$, scaled by the average of the number of expected elementary nucleon-nucleon collisions $\langle N_{\mathrm{coll}} \rangle_f$ with centrality f:

$$R_{AB} = \frac{\mathrm{d}N^h_{AB}}{\mathrm{d}N^h_{pp} \cdot \langle N_{\mathrm{coll}} \rangle_f}. \tag{2.7}$$

The measures $\mathrm{d}N^h_{AB}$ and $\mathrm{d}N^h_{pp}$ are the so-called *yields*[13] of particle species h in a collision of nuclei A+B and p+p, respectively.

[13] For more details see Appendix A.

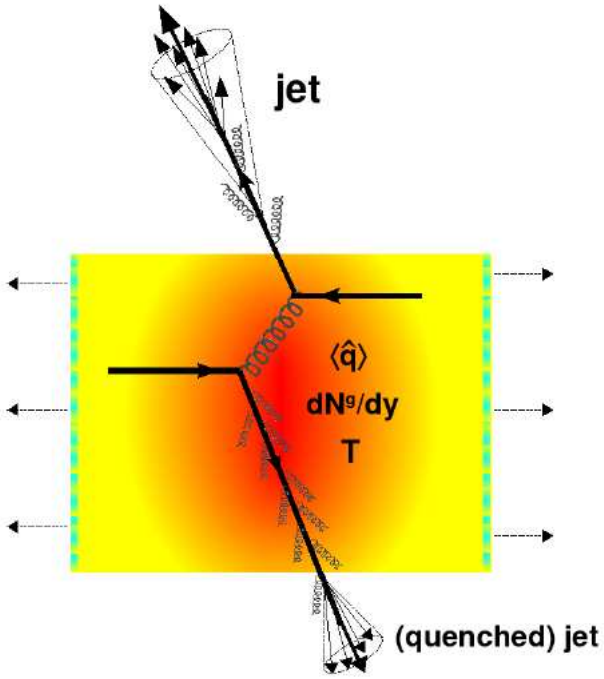

Figure 2.6: Sketch of jet production, propagation and energy loss in the produced medium of a nucleus-nucleus collision [d'E09].

The parameter N_{coll} is connected to the average of the nuclear overlap function $\langle T_{AB} \rangle$ and the inelastic cross section $\sigma^{in}_{\mathrm{NN}}$ as follows:

$$\langle N_{\mathrm{coll}} \rangle_f = \sigma^{in}_{\mathrm{NN}} \cdot \langle T_{AB} \rangle_f. \tag{2.8}$$

In other words, the nuclear overlap function T_{AB} can be characterised as a nucleon luminosity[14] (see Figure 2.7).

Calculations to evaluate a value of N_{coll} and T_{AB}, respectively, are determined with Monte Carlo Glauber simulations [Mil07] whereas the inelastic nucleus-nucleus cross section is about $\sigma^{in}_{\mathrm{NN}} \approx 42$ mb. For a more detailed view see for example [Rey03a]. The nuclear modification factor can be rewritten as:

$$R_{AB} = \frac{\mathrm{d}N^h_{AB}}{\sigma^{in}_{\mathrm{NN}} \cdot < T_{AB} >_f}. \tag{2.9}$$

In absence of medium effects, the value of R_{AB} is expected to be unity and if hadrons are suppressed, the result should be $R_{AB} < 1$.

[14] The luminosity L gives exposure of the event rate $\mathrm{d}N/\mathrm{d}t$ and is defined with the cross section of the process σ: $\dot{N} = \sigma \cdot L$.

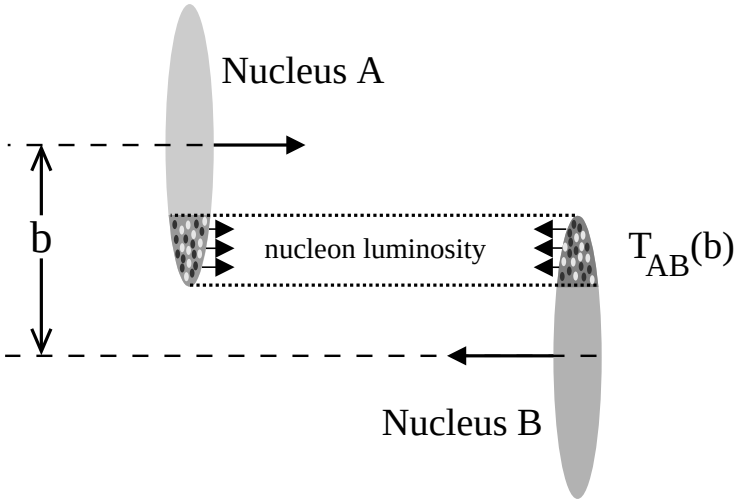

Figure 2.7: Geometrical illustration of the nuclear thickness T_{AB} [KB04].

Nevertheless there are other effects that can influence the modification factor which have to be studied to justify value $R_{AB} < 1$ as a signature in terms of jet quenching.

2.5.2 Effects of Cold Nuclear Matter

Effects of cold nuclear matter can be responsible for variations of the modification factor without any connection to the produced medium in nucleus-nucleus collisions. Moreover, the nuclear structure and interaction processes in the cold medium can also have an effect on particle production. The different effects are presented in the following.

Cronin Effect

Comparisons of measurements have shown that proton-proton and proton-nucleus collisions do not simply scale with the number of nucleons A in the nucleus [Cro75, Ant79]. Hence, the scaling of the cross section for given p_{T} is shown in the following equation:

$$\underbrace{E\frac{\mathrm{d}^3\sigma}{\mathrm{d}p^3}(p_{\mathrm{T}}, A)}_{(p+A)} = \underbrace{E\frac{\mathrm{d}^3\sigma}{\mathrm{d}p^3}(p_{\mathrm{T}}, 1) \cdot A^{\alpha(p_{\mathrm{T}})}}_{(p+p)}, \tag{2.10}$$

with $\alpha > 1$ for $p_{\mathrm{T}} \gtrapprox 2$ GeV/c.
This effect can be explained with multiple soft scattering of the incoming parton. The

radiation of soft gluons causes an additional transverse momentum for the parton before the process of hard scattering. The Cronin effect results in $R_{AB} > 1$.

Colour Glass Condensate

Saturation effects may influence the parton density inside a nucleus. Therefore, the fractional momentum[15] x becomes important. x describes the fraction of the whole momentum of a hadron carried by a quark or gluon. Measurements from deep inelastic positron-proton scattering at HERA (DESY) showed a strong increase in the number of gluons for small fractional momentum x which becomes much larger than the number of quarks and anti-quarks. In addition, the number of quarks increases at fixed x for increasing momentum transfer Q^2 [Che03].
The *colour glass condensate* (CGC) provides a description for small x scales below a saturation momentum Q_{sat}. The model predicts a fusion of gluons $gg \rightarrow g$ for high gluon densities which are characterised by a small coupling constant $\alpha_s \ll 1$. The gluon fusion basically limits the gluon density for small x.
In a nucleus gluons can interact with different nucleons. In conclusion, for a fixed x, the saturation momentum Q_{sat} increases depending on the mass number A according to $Q^2_{\text{sat}} \approx A^{\frac{1}{3}}$. For a detailed overview see [Ian03]. The formation of a CGC in an incoming nucleus can reduce the nuclear modification factor. It is an initial state effect and would therefore cause a similar influence on R_{AB} in p+A or d+A collisions where no formation of a QGP is expected.

Nuclear Shadowing

Nuclear effects can also have an impact on the particle production processes. In this context, the focus is put on the parton distribution function (PDF) or structure function $F_2(x, Q^2)$ which can be determined by extraction of the cross sections of deeply inelastic scattering processes [Pov06]. The parton distribution function provides the probability density to find a particle with momentum fraction x at a momentum transfer Q^2. Experiments have shown that PDFs for free nucleons and nucleons bounded in nuclei are different. Therefore, the medium of nuclei affects the momentum distribution of quarks [Arn94].
Nuclear effects can be described by the ratio $R^A_{F_2}$ of a quark distribution function in a nucleus $F_2^A(x, Q^2)$ and in a free nucleon $F_2^p(x, Q^2)$. For nucleon PDFs, deuteron

[15] x is also denoted as the Bjorken scaling variable.

PDFs $F_2^d(x, Q^2)$ are used which correspond to the average PDF of a nucleon neglecting Fermi-motion. The ratio is given as $R_{F_2}^A = F_2^A(x, Q^2)/F_2^d(x, Q^2)$ [Pil00]. The effects are denoted as:

1. *nuclear shadowing*: $R_{F_2}^A < 1$ for $x \lesssim 0.1$,
2. *anti-shadowing*: $R_{F_2}^A > 1$ for $0.1 \lesssim x \lesssim 0.2$,
3. *EMC effect*: $R_{F_2}^A < 1$ for $0.3 \lesssim x \lesssim 0.8$,
4. *Fermi motion*: $R_{F_2}^A > 1$ for $x \to 1$.

3. The PHENIX Experiment

The PHENIX experiment is part of the RHIC collider complex at the Brookhaven National Laboratory (BNL) on Long Island. The research facility started collisions of gold nucleons June 14th 2000. The whole complex is shown in Figure 3.1. The accelerator facility is designed to study properties of nuclear matter under extreme conditions and to explore global characteristics of the phase diagram and fundamental features of the strong interaction. A prime goal is to produce a deconfined state of matter (a Quark-Gluon-Plasma (QGP)) and to study its properties. Moreover, the PHENIX spin programme investigates the spin structure of the proton through longitudinally and transversely polarised proton collisions.

3.1 Accelerators

Relativistic energies for heavy ions cannot be achieved by a single accelerator. Therefore, a series of different accelerators are used. The accelerator setup consists of a *Tandem van de Graaff*, a *Booster Synchrotron*, the *Alternating Gradient Synchrotron* (AGS), and so-called *stripping foils* which are used to pre-accelerate and to ionise heavy ions before the injection into the collider, respectively (see Figure 3.1). For injecting and accelerating gold ions, a pulsed sputter ion source creates negative charged gold ions. They are accelerated first by the Tandem van de Graaff to approximately 1 A GeV. Electrons are partly stripped off by a foil in the high voltage terminal. The positive ions are transferred to the Booster Synchrotron where the ions are captured, accelerated up to 78 A MeV, and grouped into three bunches. After further complete stripping of the electrons the gold ions are injected into the AGS. The AGS accelerates the gold ions further to 10.8 GeV per nucleon before they are injected into RHIC [Yag05].

3.2 RHIC

The collider is composed of two independent non-circular concentric superconducting magnet rings which have a length of 3834 m each. Colliding species in the ring are accelerated in opposite directions. The setup allows an energy per nucleon in each

tube up to 100 GeV/nucleon for heavy ions and energies up to 250 GeV for protons. 1740 magnets, including dipole, quadrupole, and other correction magnets are cooled to $\lesssim 4.6$ K. The quadrupole and dipole magnets guide and focus the beam of ions in each pipe into well defined orbits. The colliding particles are not equally distributed over the whole ring, they are grouped in so-called *bunches*. The collider provides six crossing points where the bunches of the opposing beams can collide. Experiments are built up at four collision points to explore the physical nature of produced conditions and properties of particles. In this analysis, deuteron-gold collisions at $\sqrt{s_{\mathrm{NN}}} = 200$ GeV are studied. An overview of all PHENIX runs is given in Appendix G.

3.3 RHIC experiments

Besides PHENIX, the RHIC complex consists of three other major experiments, two of them were decommissioned between 2005 and 2006.

3.3.1 STAR

A massive detector with a weight of 1,200 tons is the Solenoidal Tracker at RHIC (STAR) [Ack03]. Its main component is the large Time-Projection Chamber (TPC) with a length and diameter of 4 m. It covers a pseudo-rapidity region of $|\eta| < 1.8$. The TPC is situated inside the solenoid magnet. It allows the simultaneous tracking and identification of a huge amount of charged particles produced in heavy ion collisions. Additional tracking information is provided by the Silicon Vertex Detector (SVD) which improves the momentum resolution.
The STAR physics program at RHIC is used to study high energy QCD and to measure the spin structure function of the proton. Another part is the survey of photon and pomeron[1] interactions from electromagnetic fields of the passing ions at RHIC.

3.3.2 BRAHMS

The Broad Range Hadron Magnetic Spectrometer (BRAHMS) [Ada03] was one of the smaller detectors in the RHIC collider complex. BRAHMS was used to study

[1]The pomeron is a hypothetical particle which is still unknown but needed to explain the slow rising cross section of hadronic collisions at high energies [Lev98].

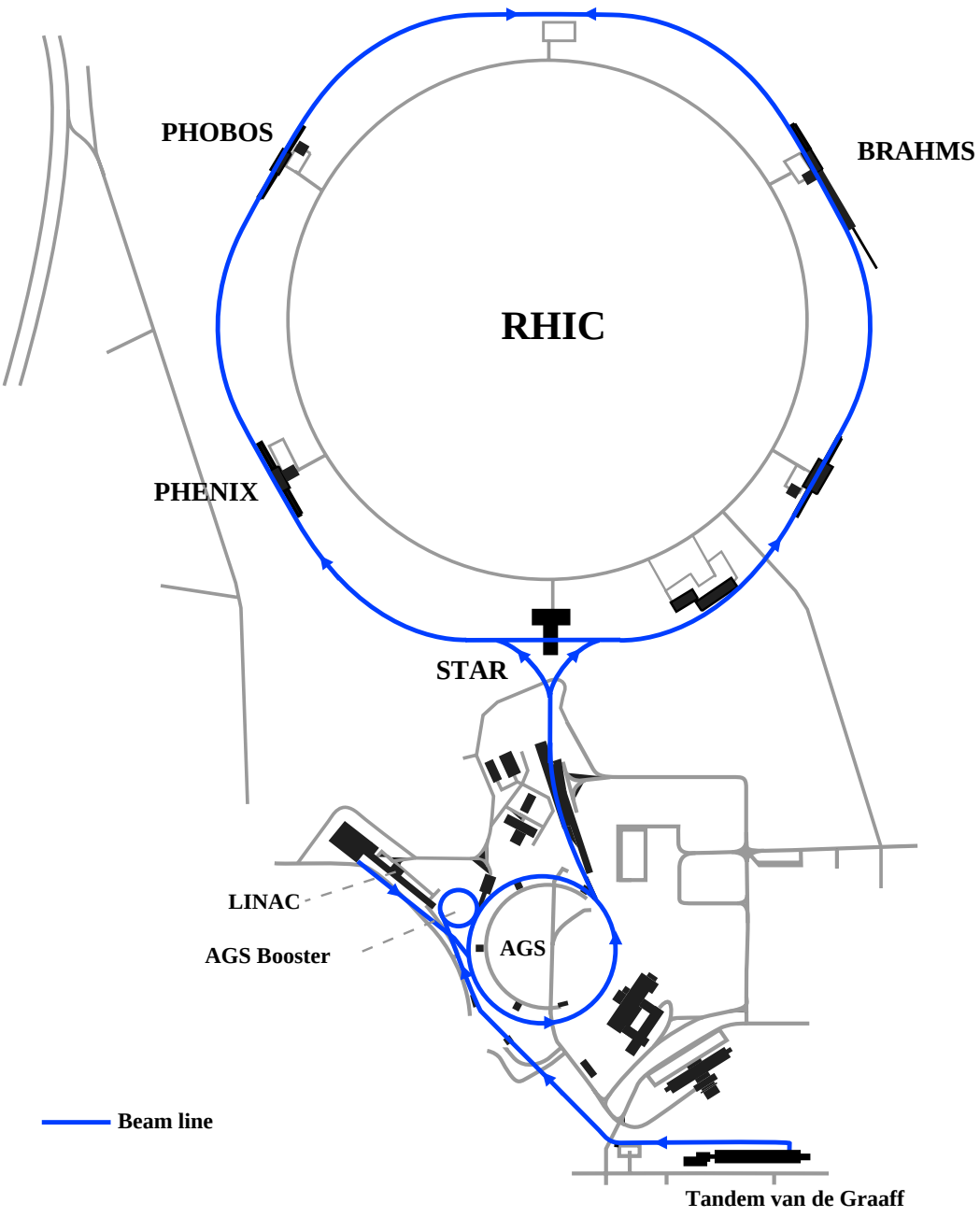

Figure 3.1: BNL birds-eye-view over the accelerators and the RHIC collider with the four major experiments [KB04].

the behaviour of charged hadrons as they pass through the experimental setup and to investigate reaction mechanisms over a wide range of rapidity and transverse momentum. The detector completed taking data in June 2006.

3.3.3 PHOBOS

PHOBOS[2] [Bac03] was also one of RHIC's smaller detectors. The detector was designed to explore and examine a very large number of gold ion collisions. Thus the detector gives a global overview of the consistency of the collision. Moreover, detailed information about a small subset of the nuclear fragments which were rejected from the high energy-density region is provided. This detector has been inoperative since 2005.

3.4 The PHENIX detector

PHENIX consists of different detector types. The experimental setup for Run 8 is shown in Figure 3.2 and can be subdivided into three global parts [Adc03b]:

- the inner detector system,
- the central spectrometers,
- detectors of the muon arms.

The setup of the two central arms is demonstrated in Figure 3.2. The central arm is divided into the west arm and the east arm. The detectors of the muon arms and the central spectrometers are displayed in Figures 3.2 and 3.3.

3.4.1 The Inner Detector System

The Inner detector system performs the task of event characterisation and consists of the *Zero-Degree-Calorimeter* (ZDC), the *Beam-Beam-Counters*(BBC), and the *Reaction Plane Detector* (RxNP). These detectors cover the whole azimuth.

[2]no acronym

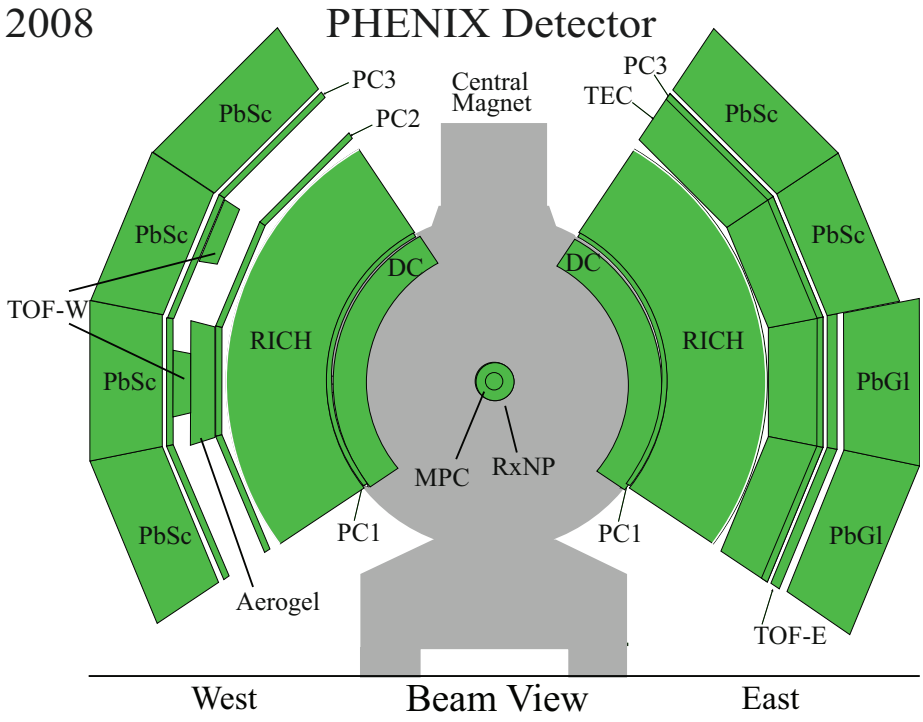

Figure 3.2: Sketch of the beamview of the PHENIX detector an its components [phe09].

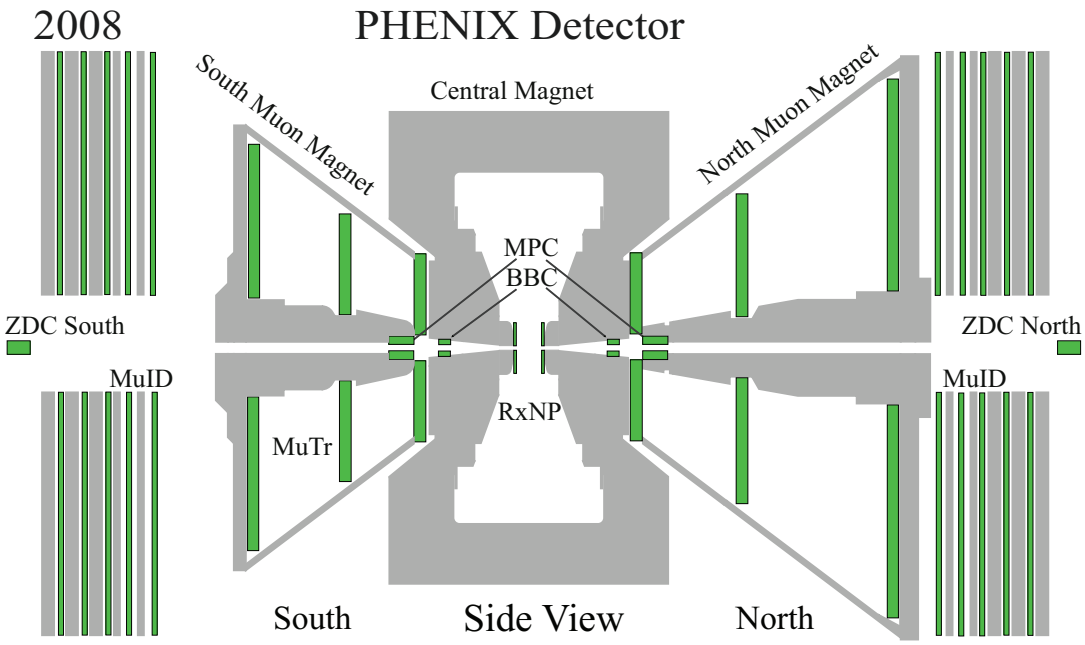

Figure 3.3: Sketch of the sideview of the PHENIX detector [phe09].

Beam Beam Counter (BBC)

The BBC consists of two identical detectors which are placed 144 cm from the interaction vertex outside the central magnets and surround the beam pipe [All03]. Each detector consists of 64 quartz Cherenkov detectors with a diameter of 3 cm, respectively. The pseudo-rapidity range covered by the BBC goes from 3.1 to 3.9. Every single element of the BBC has a time resolution of (52 $\pm$ 4) ps [All03]. The BBC detector is important for the centrality and collision-vertex determination. Moreover, the trigger condition for collisions depends on this detector system (see Section 3.8.1). Additional, the BBC is used as a start counter for the time of flight (TOF) measurement of particles in forward direction which is important for hadron separation.

Zero Degree Calorimeter (ZDC)

The ZDCs are situated along the beam axis. These hadron calorimeters are able to detect particles in the 'zero degree' region. These detectors are designed to measure neutrons and their total energy along both beam directions from grazing collisions. Furthermore, this subsystem has the purpose to determine the multiplicity and to form a trigger for peripheral collisions [Adl00]. The ZDCs are located at $\pm$18.25 m from the primary vertex, between the dipole magnets of the RHIC magnet system in forward rapidities ($|\eta| > 6$) (see Figure 3.2). Moreover, this detector is installed in all RHIC experiments and therefore it provides a control for the beam-luminosity. The ZDC has an energy resolution of about 25% for single neutrons. In addition, the signal of the ZDC in correlation with the BBC can be used for measuring the centrality and for the determination of the collision-vertex.

Reaction Plane Detector (RxNP)

The Reaction Plane Detector (RxNP) is an upgrade of the PHENIX experiment and was installed in 2007. The detector covers the rapidity region $1.0 < |\eta| < 2.8$. The RxNP is composed of plastic scintillators and PMTs divided into 12 $\times$ 2 sectors in each north and south side. This detector is very useful to study the anisotropy of events. Therefore, the measurement of the elliptical flow is improved with the help of the RxNP. In addition, the reaction plane resolution is improved by the factor of two [Mik09].

3.4.2 Central Arm Spectrometers

The PHENIX tracking system which consists of Pad Chambers (PC), Drift Chambers (DC), and the Time-Expansion-Chamber (TEC) [Adc03a] is a part of the central arm spectrometers. These three detectors offer the ability of identifying particles, of reconstructing invariant masses of electron and kaon pairs, and of measuring momentum of charged particles. Furthermore, the Time-of-Flight (TOF), Ring-Imaging-Cherenkov (RICH), and Aerogel Cherenkov detectors in the central arms also provide particle identification. All the detector systems cover an azimuthal angle of 180°, a pseudo-rapidity range of $|\eta| < 0.35$, and have a concentric arrangement around the beam pipe at different distances from the vertex. Besides the tracking system, TOF, RICH, and Aerogel, the central arms comprise electromagnetic calorimeters (EMCal) which are the outermost detectors. The EMCal is important for this analysis and will be explained in more detail in the next section.

Drift Chambers

At a distance between 2 m and 2.4 m from the z axis, the *Drift Chambers* are located. The detector setup is identical in each arm and measures the deflection of charged particles in the magnetic field caused by the central magnet (CM). It determines the trajectory in r-ϕ-direction to calculate the momentum of charged particles (and the invariant mass of particle pairs). The resolution of the DC is approximately 150 μm (in r-ϕ direction) and about 2 mm in z direction [Adc03a].

Pad Chambers (PC)

The Pad Chambers (PC) are multiwire proportional chambers with three separate layers in the PHENIX setup. They perform 3D spatial point measurements. Moreover, this subsystem is important for pattern recognition and longitudinal momentum reconstruction. The innermost pad chamber plane (PC1) is located between the DC and the RICH in both east and west arms. The PC2 layer is situated behind the RICH and is only present in the west arm whereas the pad plane PC3 is attached in front of both EMCal detectors. The detector has a resolution of ± 1.7 mm in z direction [Adc03a].

Ring Imaging Cherenkov Detector

The *Ring Imaging Cherenkov Detector* (RICH) is located radially behind the PC1 in both arms. The RICH has a volume of 40 m^3 and is filled with CO_2. 48 composite mirror panels form two intersecting spherical surfaces in each detector. The total reflecting area has a size of 20 m^2. Produced Cherenkov light is focused on a total of 2560 photomultipliers to detect the signal.
Particles passing through the medium produce Cherenkov light if their velocity is higher than the speed of light in the medium. Due to the low mass of electrons compared to pions, the detector provides a good separation of electrons and pions because the Cherenkov threshold of pions is about $p = 4.65$ GeV/c compared to $p = 18$ MeV/c for electrons in CO_2. The setup produces an average of 12 photons per ring[3] for particles with $\beta = 1$ and a path length of 1.2 m [Aiz03].

Time Expansion Chamber

Another part of the PHENIX tracking system is the TEC. This subsystem is mounted between the RICH detector and the pad plane PC3 and can be found in the west arm only. The TEC is composed of a set of 24 multiwire tracking chambers in four sectors. Each sector consists of six chambers and subtends $\frac{\pi}{8}$ in azimuth. It aids with measuring particle tracks in addition to the information provided by the PCs and DCs. Besides track reconstruction, the TEC is able to improve the momentum resolution for $p_T \geq 4$ GeV/c. It measures ionisation energy losses $\frac{dE}{dx}$ of charged particles and enables the separation of electrons and pions at high multiplicity [Adc03a]. Since Run 3, the TEC was upgraded by adding radiators just in front of the drift region to a *Transition Radiation Detector* (TRD). This upgrade extends the momentum range of electron identification and helps to discriminate electrons from pions up to tens of GeV/c.

Time of Flight

The PHENIX *Time of Flight* (TOF-E) system is placed 5.1 m from the collision vertex between the lead glass calorimeters and the pad chamber (PC3) in the east arm. It consists of 960 slats of scintillators and photomultiplier tubes for read out and covers $\pi/4$ of the azimuth. The TOF measures the time of flight of particles and provides a time resolution of 100 ps to achieve a separation of pions and kaons up to

[3] The Cherenkov light is emitted in the form of a ring, see Figure 3.6.

2.4 GeV/c and a separation of kaons and protons up to 4 GeV/c [Aiz03]. In 2006, two TOF detectors using *Multi-Gap Resistive Plate* (MRPC) technology were mounted in the west arm of PHENIX. One of the detectors was placed between the Aerogel Cherenkov Detector (ACC) and the pad chamber PC3, the other one between the pad chambers PC2 and PC3. With an intrinsic timing resolution performance of 70 ps, the setup of the TOF-W performs pion-kaon separation up to 3 GeV/c and proton identification up to 5 GeV/c. In conjunction with ACC and RICH, the range for particle identification and separation of pion, kaon, and proton is improved up to 9 GeV/c [Lov09].

Aerogel Cherenkov Detector

Another detector which performs the task of particle identification is the *Aerogel Cherenkov Detector* (ACC). The ACC is placed between the pad chamber PC2 and the TOF-W detector in the west arm. The detector enlarges the momentum region for particles to be identified. The aerogel detector is built up of 160 cells and is situated at a distance of 4.5 m from the collision vertex. A single cell of the aerogel counter consists of three parts, an integration air gap, the aerogel part, and two PMTs for readout. The PMTs are mounted at the side surfaces of the integration air gap part. For the aerogel radiator, the hydrophobic silica aerogel was chosen which has a refractive index of n = 1.011 [Sus03]. The capabilities of the detectors for particle identification are shown in Figure 3.4.

		Pion-Kaon separation	Kaon-Proton separation
TOF	σ~100 ps	0 - 2.5	- 5
RICH	n=1.00044 γth~34	5 - 17	17 -
Aerogel	n=1.01 γth~8.5	1 - 5	5 - 9

Figure 3.4: PID capabilities for Aerogel, RICH and additional TOF [Vel05].

In this context, it is important to emphasise that the setup of the particle identification detectors (RICH, AEROGEL, TOF) is chosen to act as a conjunction. This means that the regions of particle separation of the individual setups sum up to cover the whole momentum region. The same statement is valid for the PHENIX tracking system.

3.5 Electromagnetic Calorimeters

The *Electromagnetic Calorimeter* (EMCal) consists of eight sectors in the outermost region of the central arms of the PHENIX setup. Every sector covers a pseudo-rapidity region of -0.35 $< |\eta| <$ 0.35 and an azimuthal angle of $\Delta\phi = 22.5°$.
The EMCal system is built of six Pb-scintillator (PbSc) calorimeters and two Pb-glass (PbGl) calorimeters and is used to measure the energy and spatial position of photons, positrons, and electrons produced in heavy ion collisions. Furthermore, the measurement of neutral mesons is possible via the invariant mass reconstruction of the decay photon pairs. Due to their different properties in timing resolution, granularity, and energy resolution, the setup of these two different calorimeters offers the advantage of independent cross checks of measurements in the same experiment. The two Pb-glass calorimeters are installed in the sectors E0 and E1 in the east arm. The two Pb-scintillators are mounted in the sectors E2 and E3 in the east arm and the other four Pb-scintillators are placed in the sectors W0, W1, W2 and W3 in the west arm. The arrangement of the detectors is shown in Figure 3.5.

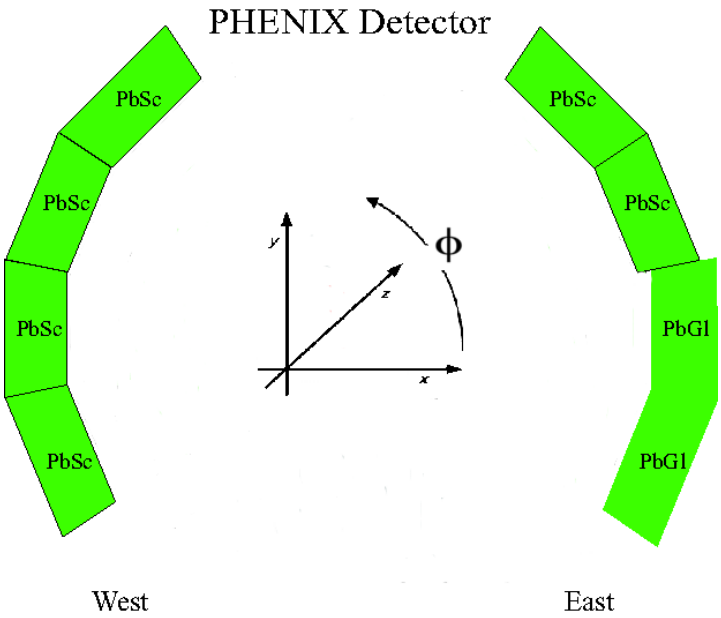

Figure 3.5: The sketch shows the arrangement of the electromagnetic calorimeters in the detector arms.

3.5.1 Lead-Glass Calorimeter

Modes of Operation

The physical phenomenon called *Cherenkov radiation* is the emission of light through charged particles whose velocity v is larger than the phase velocity of light $\frac{c}{n}$ in a medium where n is the refraction index of the medium. If a charged particle passes through an electric insulating medium (insulator), e.g. lead glass, it will produce a polarisation of the electron shell of an atom and induce a time-variant dipole moment, emitting electromagnetic waves [Dem05]. Cherenkov radiation is produced at a specific angle ϑ_c against the flight direction of the charged particle where the photons constructively interfere and intensify the radiation if the condition $v > \frac{c}{n}$ is fulfilled (see Figure 3.6). This effect plays a major role for the PbGl. The angle is given by:

$$\cos\vartheta_c = \frac{\frac{c}{n}}{v} = \frac{1}{\beta \cdot n}, \qquad (3.1)$$
$$\text{with} \quad \beta = \frac{v}{c}.$$

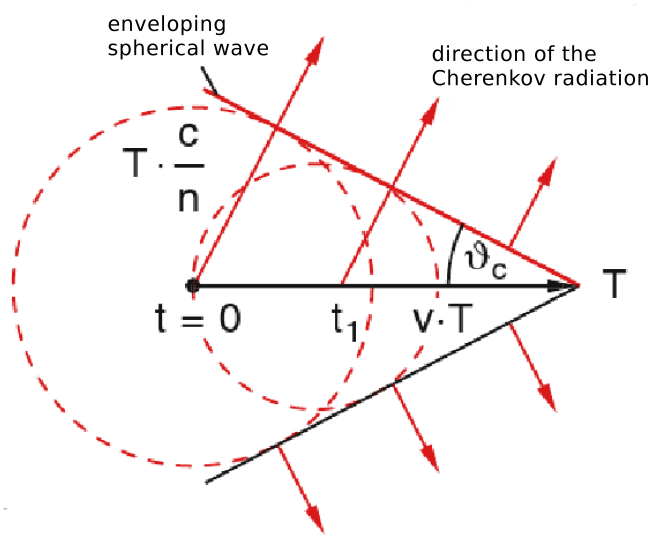

Figure 3.6: The sketch shows the production of the Cherenkov radiation in the specific angle ϑ_c against the flight direction.

High energetic photons entering a PbGl material principally produce electron-positron pairs[4]. Because of the interaction of the electron and positrons with the electric field of nuclei, Bremsstrahlung is emitted which also produces e^+e^- pairs. Thus an *electromagnetic shower* evolves which continues until the energy of single particles falls below a certain energy E_c where ionisation becomes the dominant process.

PbGl Setup

The *Lead-Glass Calorimeter* (PbGl) [Aph03b], situated in the two lower sectors of the east arm, is a Cherenkov calorimeter. The PbGl is mounted at a radial distance of 5.4 m from the collision vertex. A so called *module* is the smallest detector unit. A module has the dimension of 4 cm × 4 cm × 40 cm and is wrapped in aluminised mylar foil and shrink tube. 4 × 6 modules form a *supermodule* (SMD) which is glued together with carbon fibre and epoxy resin, forming a self-supporting SMD (see Figure 3.7).
Each module is read out with a photomultiplier. Every sector comprises 192 SMDs in an array of 12 SMDs high and 16 SMDs wide. A gain monitoring system based on a set of three LEDs is mounted on every end of each SMD. This monitoring system provides the function to simulate an electromagnetic shower to calibrate and test the supermodule and the readout system.
Attached to the SMD is a photodiode together with a preamplifier to monitor the LEDs, as shown in Figure 3.7.
The PbGl calorimeter uses the Cherenkov effect, as described above. Due to the fact that the amount of emitted Cherenkov photons is proportional to the energy of the incident photon, the detection of Cherenkov radiation can be used to measure the energy of photons. Furthermore, the setup of the PbGl is suited to suppress hadrons. First of all, the interaction length is approximately the thickness of the detector so hadrons are not likely to interact or they just deposit a small fraction of their total energy in the calorimeter. Secondly, only Cherenkov light is observed and the thresholds for muons, pions, and protons are 81, 106, and 715 MeV/c, respectively, which is explicitly higher than the Cherenkov threshold for electrons produced in electromagnetic showers. The radiation length X_0 is the distance where the energy of an electron is reduced by the factor $\frac{1}{e}$. The PbGl has a radiation length of 2.8 cm [Aph03b].

[4]Compton scattering and photo effect play a minor role in this energy regime.

The initial energy and position resolution of the PbGl calorimeter is given by:

$$\frac{\sigma(E)}{E} = \frac{[5.9 \pm 0.1]\%}{\sqrt{\frac{E}{\mathrm{GeV}}}} \oplus [0.8 \pm 0.1]\%, \tag{3.2}$$

$$\sigma_x(E) = \frac{[8.4 \pm 0.3]\ \mathrm{mm}}{\sqrt{\frac{E}{\mathrm{GeV}}}} \oplus [0.2 \pm 0.1]\ \mathrm{mm}. \tag{3.3}$$

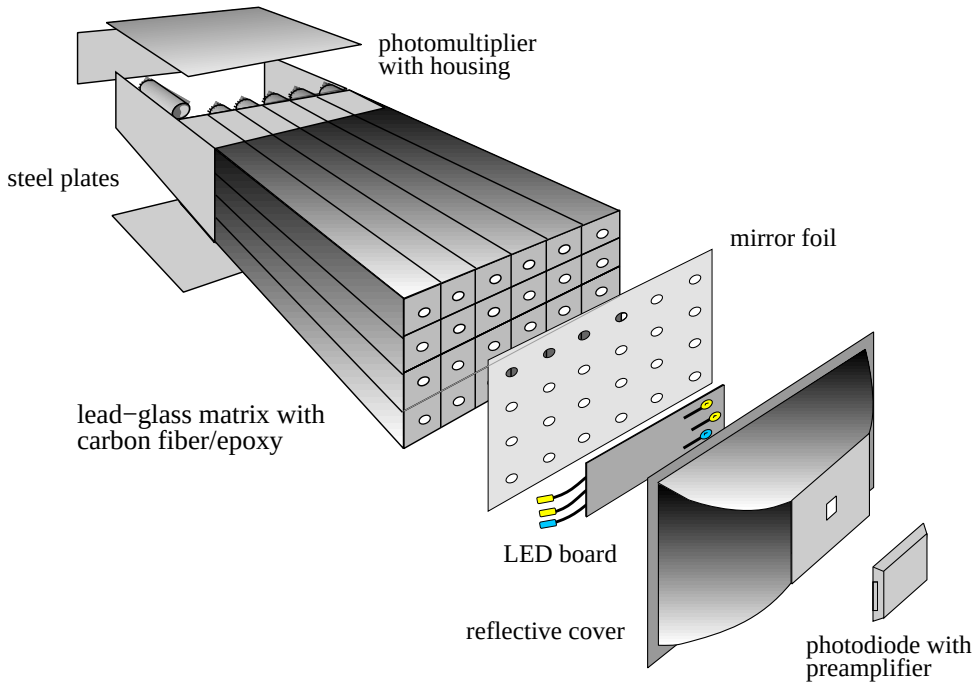

Figure 3.7: Sketch of a lead glass supermodule consisting of 24 modules with the reference system [Aph03b].

3.5.2 Lead-Scintillator Calorimeter

The *Lead-Scintillator Calorimeter* (PbSc) is a sandwich calorimeter where the energy deposit of a particle is determined via collecting scintillation light produced at various depths of the detector. The smallest detector unit, a PbSc *tower*, is made

of 66 sampling cells consisting of alternating tiles of Pb (0.15 cm) and scintillator (0.4 cm) with a volume of 5.535 cm × 5.535 cm × 37.5 cm. The scintillator contains an organic scintillator and a fluorescent additive. Every tile is plated with Al and the cells are optically connected to 36 longitudinally penetrating wavelength shifting fibres to collect the light [Aph03b]. Photomultipliers situated at the back of the towers are responsible for light readout. Four towers are grouped together and form a so-called *module* as shown in Figure 3.8. A *supermodule* consists of 36 modules. 18 supermodules form a *sector* which covers an area of 2 × 4 m^2 which corresponds to an array of 36 towers high and 72 towers wide. In conclusion, one supermodule contains 144 towers and is read out by one Front End Module (FEM) where the Front End Electronic (FEE) is integrated. The radiation length of the PbSc is about 2.02 cm.

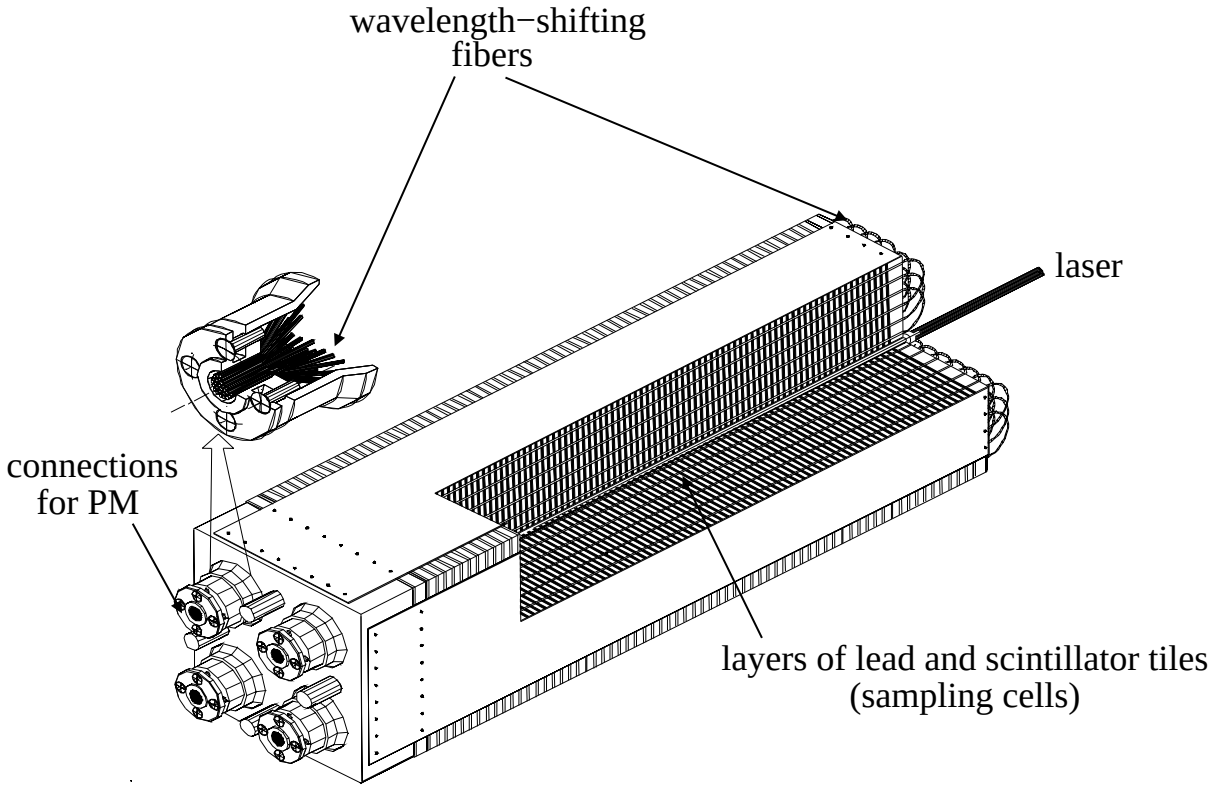

Figure 3.8: One PbSc module consisting of four towers, each read out by one photomultiplier. Additionally, the sampling cells of the module and the wavelength shifting fibres are sketched [Aph03b].

The PbSc is monitored and calibrated via an UV laser (YAG). Light is injected into a plastic fibre, running in the middle of one module, and simulates an electromagnetic shower of 1 GeV in the four surrounding towers.
The initial energy resolution of the PbSc calorimeter is given by:

$$\frac{\sigma(E)}{E} = \frac{8.1\%}{\sqrt{\frac{E}{\mathrm{GeV}}}} \oplus 2.1\%. \tag{3.4}$$

The position resolution is angular dependent and described by the formula:

$$\sigma_x(E, \phi) = \sigma_0(E) \oplus \Delta \times \sin\phi, \tag{3.5}$$

with a position resolution for normal incidence:

$$\sigma_0(E) = \frac{5.7 \text{ mm}}{\sqrt{\frac{E}{\mathrm{GeV}}}} \oplus 1.55 \text{ mm}, \tag{3.6}$$

and $\Delta \sim X_0 = 2.02$ cm.

3.6 Muon Spectrometers

Detectors of the muon arms consist of the *muon tracker*, the *muon identifier*, and the *muon piston calorimeter* in the north and south arm of the PHENIX experiment. Through reconstruction of the trajectory, the momentum of muons can be determined. The measurement of muons provides additional information for the investigation of the QGP properties and allows the separation of mesons, in particular the identification of J/Ψ, Ψ', and lighter mesons. In the following the detector characteristics will be explained.

Muon Piston Calorimeter (MPC)

A new electromagnetic calorimeter which has been integrated into the muon forward spectrometers is the muon piston calorimeter (MPC). The MPC was installed in the south muon piston hole (-3.7 $< \eta <$ -3.1) in 2006 and the other in the north muon piston hole (3.1 $< \eta <$ 3.9) in 2007 [Mer09]. Both calorimeters cover an azimuthal angle of 2π and are mounted at a distance of 220 cm from the nominal interaction point. The MPC uses $PbWO_4$ scintillator crystals with Avalanche Photodiode (APD) readout [Chi07].

Furthermore, the detector setup offers the possibility to measure nuclear modification factors in the forward and backward directions as well as azimuthal correlations of di-hadron pairs at different pseudo-rapidities via energy deposit. The detector allows the exploration of low-x parton distributions.

Muon Tracker (MuTr)

The muon tracker (MuTr) is comprised of three stations of cathode-strip readout chambers. The chambers are mounted inside the conical-shaped moun magnet (see Figure 3.3). Muons at rapidities of $1.2 < |\eta| < 2.4$ can be detected over the full azimuth. The detector has a spatial resolution of 100 μm and provides a relative mass resolution $\sigma(M)/M$ of $6\%/\sqrt{M}$, where M is in GeV. These properties allow a good separation of heavy mesons like J/Ψ and Ψ' or lighter mesons like ρ/ω and ϕ. Moreover, the detection of muons with high momentum can be used to study Z- and W-boson production [Aki03].

Muon Identifier (MuID)

The muon identifier (MuID) is situated in the outermost part of the muon arms. This detector covers the same rapidity and azimuthal ranges as the muon tracker. Behind the muon magnet backplate with a thickness of 30 cm, a segmentation of four steel absorbers of thicknesses 10, 10, 20, and 20 cm is chosen. The five gaps created by the absorbers are instrumented with the MuID detecting panels, streamer tubes were chosen as the detector technology. A very important requirement is the suppression of the background, dominated by mis-identified pions and also muons from pion decay. A pion suppression of $2.0 \cdot 10^{-4}$ to $3.9 \cdot 10^{-3}$ in the momentum range of 2.0 GeV/c to 10.0 GeV/c is reached with this setup [Aki03].

3.7 Data Acquisition

A huge challenge for the PHENIX setup is to handle the amount of information produced in heavy ion collisions during operations. The large interaction rate and therefore the event production varies in Au+Au collisions from a rate of a few kHz to 500 kHz in p+p collisions [Adl03a]. The *data acquisition* (DAQ) has to provide a fast conversion of the information given by the different subsystems, select rare events, and mark events with interesting characteristics before storage.

In the following section, the processing of the data amount will be discussed briefly, for more information see [Adl03a].
Every detector subsystem is read out by *Front-End-Modules* (FEM). They digitise the analog signal and forward them to the *Level1-Trigger System* (LVL-1) where the decision of rejection or transmission of the collected data is made.
The Level1 Trigger System consists of two components. On the one hand, there is the *Local Level-1 System* (LL1) which performs the task of converting the data from the detector subsystems (ZDC, BBC, EMCal etc.) into a bit pattern. On the other hand, there is the *Global Level-1 System* (GL1) which receives the data from the LL1 and summarises it. In case of fulfilling the trigger conditions, the GL1 generates a *raw* trigger. If the PHENIX DAQ has free capacity, the raw trigger becomes a *live* trigger otherwise a *busy* signal is sent out.
In the next step, the bit pattern is compared to a scale down counter. This step is necessary to handle the still huge number of events. In this context, scale down means that for instance every tenth live trigger is processed if the scale factor is ten. Finally, if this process generates an accept, a so called *scaled* trigger is set and the readout of the FEMs is initiated via the *Granule Timing Module* (GTM).
Event data accepted by the LVL1 is transferred from the FEMs over about 350000 channels to the *Data Collection Modules* (DCM). The DCMs compress and format the data and offer the ability of buffering data up to five events.
In the *Event Builder* (EvB), the data streams are forwarded to the Assembly Trigger Processors (ATP) and are merged into one event output. Afterwards, the event outputs are summarised in *data summary tables* (DSTs) and transferred to the High Performance Storage System (HPSS). Additionally, the use of Level-2-Triggers is possible in the framework of the EvB. In contrast to the hardware-based, parallel and full pipelined Level-1 triggers, the Level-2-Triggers are software-based. In this analysis, no Level-2-Triggers are used.
The access to the event data base in form of the HPSS is performed by the so-called analysis taxis. The gateway for the analysis software is interfaced via the Fun4all framework [CVS09].

3.8 Triggers

In the PHENIX experiment the amount of produced data is too large to be completely processed. Triggers offer the opportunity to choose specific physical interest-

ing events. Therefore, in PHENIX, a trigger system is applied to make fast decisions if an event should be accepted or refused.

3.8.1 Minimum Bias Trigger

The *Minimum Bias Trigger* (MinBias) is set if an inelastic collision has taken place. For d+Au collisions the BBC detector is used as the MinBias condition. In case one single photomultiplier in each BBC has measured a particle, the trigger condition is fulfilled. This is different to Au+Au collisions where a further particle detection in the ZDC is required to fulfil the MinBias trigger condition. The reason for this difference is due to the lower multiplicity and the asymmetric reaction. An additional requirement is the position of the collision vertex (z-vertex) that should lie in the region -30 cm $< z <$ 30 cm.
In d+Au collisions, $\sim$ 88% of the geometrical cross section is measured [Adl03b].

3.8.2 EMCal RICH Trigger

A part of the Level 1 trigger system is the EMCal RICH Trigger (ERT). The ERT is used to trigger on events with high energetic photons or electrons. For this analysis an ERT trigger in coincidence with the MinBias condition of the BBC (BBCLL1) is employed.
All events containing high-energy photons or electrons are recorded with the use of the ERT trigger. The ERT proves the deposited energy in an array of 4×4 modules[5], the so-called 4×4 tiles, which must exceed a certain threshold to be counted as an ERT event. The detected energy in an array of 2×2 modules, each module read out by one PMT, is processed by one ASIC chip situated in the FEE. The sum of 2×2 modules is built by the ASIC chip and a copy is forwarded to the three adjacent ASIC chips. A reason for this procedure is to be found in the properties of the electromagnetic shower which is not always confined to a single 2×2 tile. Hence, the deposited energy does not exceed the claimed threshold although the particle shower itself contains enough energy to fulfil the trigger condition. Therefore, the sum of 4×4 PMTs is built (see Figure 3.9).
Three different thresholds for the ERT trigger are available and are presented in Table 3.1. In this analysis the ERTLL1_4×4b&BBCLL1 is used.

[5]In this context and in the following tower, module always means the smallest detector unit for both EMCal systems PbGl and PbSc.

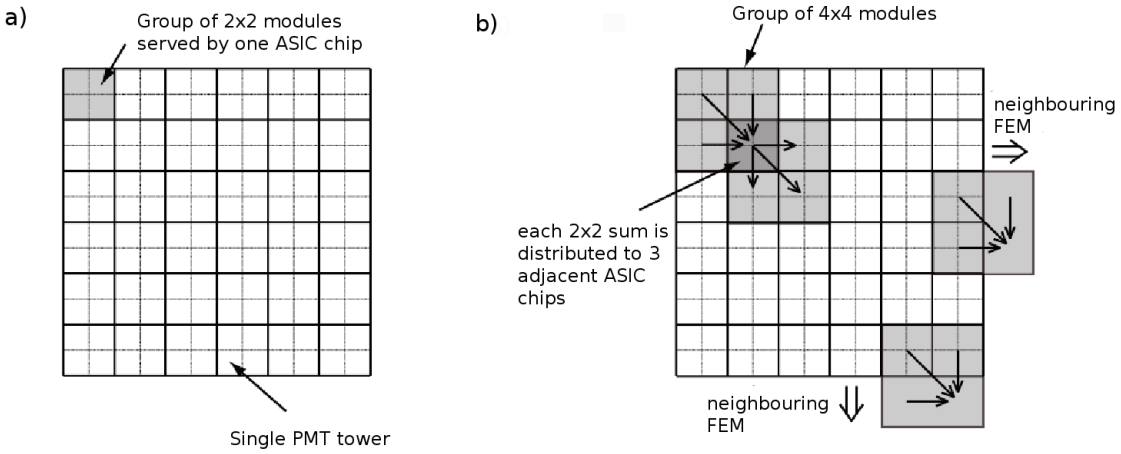

Figure 3.9: Sketch of the ERT trigger logic with the sum over 4 × 4 modules [Zau07].

Trigger	PbSc	PbGl
ERTLL1_2×2	0.8 GeV	0.6 GeV
ERTLL1_4×4a	2.8 GeV	2.1 GeV
ERTLL1_4×4b	3.5 GeV	2.8 GeV
ERTLL1_4×4c	2.1 GeV	1.4 GeV

Table 3.1: Table of the ERT thresholds (DAC values) for PbGl and PbSc.

4. Data Analysis

The physical quantities such as momentum and position of particles must be extracted from the PHENIX raw data format (PRDF) first. Respective values for each detector are written into DSTs. The DSTs are subdivided into *micro*, *nano*, and *pico*DSTs. MicroDSTs contain a reduced set of information compared to the DSTs which is basically the data for a certain type of analysis. Up to this point, all information is still kept in one file. In the next step, nanoDSTs are produced which contain information for a requested focus and are split into different files. This thesis is based on the analysis of nanoDSTs for the EMCal. A detailed description of DST production is given in [KB04].

4.1 Data Sets

In this thesis, data from d+Au collisions at $\sqrt{s_{\mathrm{NN}}} = 200$ GeV are analysed which contain two different types of events. On the one hand, there are minimum bias (MinBias) events which are only affected by the BBC trigger condition, i.e. the BBC efficiency, and on the other hand, there are ERT triggered events. The MinBias data set contains $1.6 \cdot 10^9$ events and the ERT triggered data set includes $2.6 \cdot 10^8$ events. The two different sets are used to cover a broad range of transverse momenta of the detected particles and are combined to obtain results over the whole range. For combining the data of two different trigger conditions, one has to pay attention to the rejection of data during the data acquisition. In particular, there are three different types of data:

1. MinBias events (number of events: N^{mb}),
2. MinBias & ERT triggered events (number of events: $N^{\mathrm{mb\&ERT}}$),
3. ERT triggered events (ERT) (number of events: N^{ERT}).

Note that MinBias&ERT triggered events are a subset of minimum bias events ($N^{\mathrm{mb\&ERT}} \subseteq N^{\mathrm{mb}}$). ERT triggered events also fulfil the minimum bias trigger condition but the minimum bias scaled trigger, as discussed in Section 3.7, was not set. During the data acquisition, a certain amount of minimum bias events were rejected

due to limited disk space. This rejection is not effective for ERT events and therefore a scale down must be applied to achieve the number of underlying minimum bias events $N^{\mathrm{mb}}_{\mathrm{ERT}}$. The *rejection factor* $\epsilon^{\mathrm{ERT}}_{\mathrm{trig}}$ is calculated as the fraction of MinBias events and of events for which the ERT trigger as well as the MinBias condition are fulfilled:

$$\epsilon^{\mathrm{ERT}}_{\mathrm{trig}} = \frac{N^{\mathrm{mb}}}{N^{\mathrm{mb\&ERT}}}. \tag{4.1}$$

Thus the number of underlying minimum bias events can be determined from the number of ERT events:

$$N^{\mathrm{mb}}_{\mathrm{ERT}} = \epsilon^{\mathrm{ERT}}_{\mathrm{trig}} \cdot N^{\mathrm{ERT}}. \tag{4.2}$$

The ERT triggered data set corresponds to a number of about $130 \cdot 10^9$ underlying MinBias events with a rejection factor of about $\epsilon^{\mathrm{ERT}}_{\mathrm{trig}} \approx 500$. Note that the rejection factor and therefore $\epsilon^{\mathrm{ERT}}_{\mathrm{trig}}$ depends on the centrality of the collision (see Table 4.1) because the multiplicity and consequently the number of MinBias and ERT triggered particles increases with increasing centrality. As an example, the so-called raw yield[1] of π^0's for d+Au MinBias events (0-88%) for the different trigger conditions with and without taking the rejection factor into account is shown in Figure 4.1. The analysis steps to obtain the yield from the DSTs will be discussed in Chapter 5.

4.2 Centrality Determination

Collisions are classified in centralities to distinguish between peripheral and central events. The determination of the centrality within PHENIX is done with the response of the BBC located in the *Au-going*, i. e. south side, under the assumption that the detected signal is related to the number of participants in the gold nucleus [Nag09, Dre03, Bat03].
An example of the BBC normalised charge distribution in context of the centrality determination is shown in Fig. 4.2.

For the analysis of d+Au collisions, four different centrality classes are chosen. 00-20% are the most central events, 60-88% are the most peripheral events, and 00-88% indicates MinBias events[2].

[1] The yield without any corrections applied.

[2] Dependent on the context the denotation minimum bias (MinBias) means either the trigger or the centrality class.

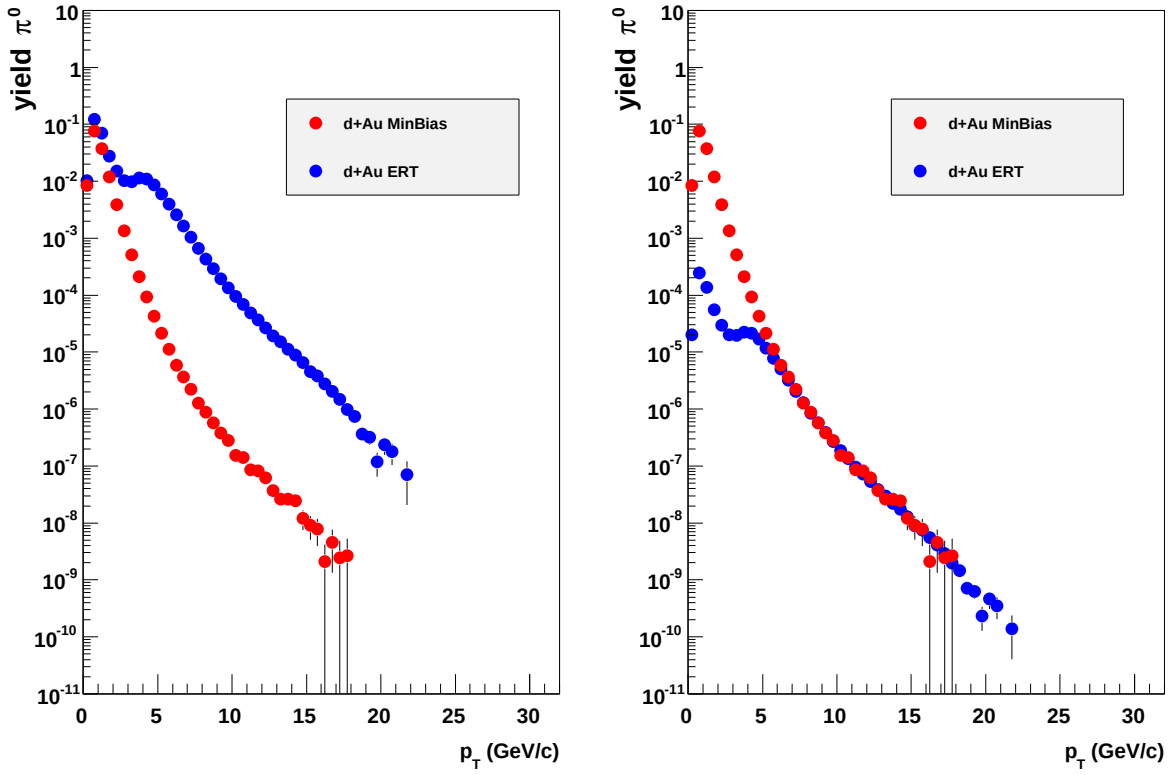

Figure 4.1: An example of the raw yield of π^0's for ERT and MinBias trigger condition with scaled (right diagram) and without scaled ERT triggered events (left diagram) for PbSc EMCal sectors. The turn-on in the ERT data is due to the trigger settings described in Section 3.8.2. At least one decay photon exceeds the certain energy threshold.

centrality class	centrality class	rejection factor
00-20%	central (cent)	274.591
20-40%	semicentral (semi)	410.149
40-60%	semiperipheral (midd)	639.597
60-88%	peripheral (peri)	1366.160
00-88%	minimum bias (MinBias)	507.558

Table 4.1: Classification of the centralities and their notation as well as the associated rejection factor.

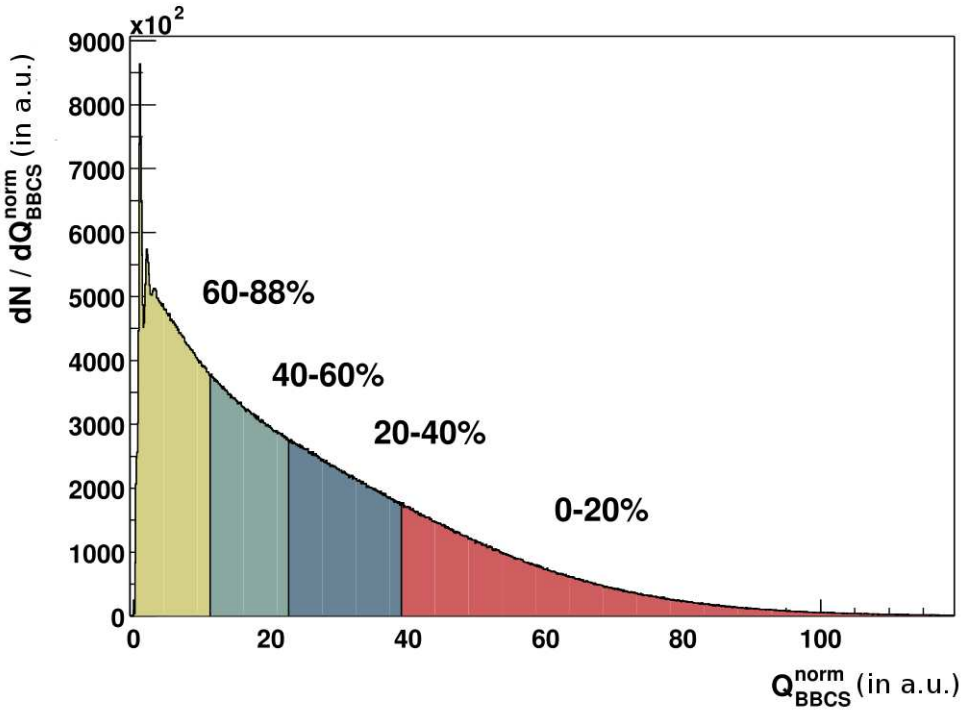

Figure 4.2: Distribution of the normalised charge in BBCs. The normalisation is done in a way that the normalised charge corresponds to the number of hits [Bat03].

4.3 DST processing

To obtain the spectra of the neutral pions, further corrections and cuts are applied to the information given in the analysed DSTs. The determination of the π^0's is done via two decay photons. There are several conditions the two photons have to fulfil before further analyzation. The corrections and cuts are presented in the following.

4.3.1 Identification of Bad Modules

In the EMCal, some modules are defect and must be excluded from the analysis. Modules without any signal are marked as dead because they would produce an energy for a cluster that is too low. Additionally, there are modules, the so-called *hot towers*, which systemically produce an excessively large signal and are marked as bad. Because of the extension of a cluster over more than one module, towers adjacent to dead or bad ones are also excluded from the analysis. To reject clusters

which suffer from leakage effects at the edges of a sector, the edge modules are also not used in the analysis. All information about rejected towers is summarised in the so-called *bad module map* which is used to exclude these areas of the EMCal from the analysis process. The bad module maps as well as the hit maps of the individual EMCal sectors are shown in Appendix D. The thresholds for determining modules as hot towers is obtained via the average number of hits per tower in each EMCal sector and the variance σ of the hit number distribution. In particular, modules that exceed the average number of hits by $\pm 7\sigma$ are rejected from the analysis.

4.3.2 Cuts

Photon measurements through electromagnetic showers in the EMCal are affected by showers produced by hadrons. More precisely, there is no or little influence on the clusters themselves but the photons and hadrons can be mixed. To reduce this background, several cuts are applied.
Further, the invariant mass is calculated for all possible photon-photon combinations which leads to large combinatorial background. Methods to reduce this background are described below.

Photon identification

Two photon identification (PID) cuts and the combination of them are used to reduce the background caused by hadrons.
A difference between the showers created by photons and hadrons is their lateral extension. Hadronic showers spread over more modules than electromagnetic showers. To quantify this phenomenon for the PbGl calorimeter, the focus is put on the dispersion D. The dispersion is a quality for the width of the shower in one direction:

$$D_{\mathrm{x}} = \frac{\sum_{\mathrm{i}} E_{\mathrm{i}} x_{\mathrm{i}}^2}{\sum_{\mathrm{i}} E_{\mathrm{i}}} - \left(\frac{\sum_{\mathrm{i}} E_{\mathrm{i}} x_{\mathrm{i}}}{\sum_{\mathrm{i}} E_{\mathrm{i}}} \right)^2 , \tag{4.3}$$

whereas x_i is the position within a sector and E_i is the deposited energy.
An electromagnetic shower usually spreads over more than one module. The information is passed to the *clusterroutine*[3], which summarises associated areas of modules

[3]The clusterroutine describes an algorithm containing several routines which have to be passed to define a cluster with a certain energy and apply all necessary corrections. A detailed overview is given in [KB04].

into the so-called *clusters*. Because of the finite size of the modules, a correction must be applied:

$$D_{\mathrm{corr}} = D_{\mathrm{x}} - \left(\left| \frac{\sum_{\mathrm{i}} E_{\mathrm{i}} x_{\mathrm{i}}}{\sum_{\mathrm{i}} E_{\mathrm{i}}} \right| - \left(\frac{\sum_{\mathrm{i}} E_{\mathrm{i}} x_{\mathrm{i}}}{\sum_{\mathrm{i}} E_{\mathrm{i}}} \right)^2 \right). \tag{4.4}$$

Equations 4.3 and 4.4 are also valid for the y-direction.
A threshold for the dispersion D_{thres} is set so that showers, electromagnetic as well as hadronic, are rejected when they exceed this limit in x- or y-direction. The threshold depends on the incident angle θ of the particles and is determined as a function of the angle:

$$D_{\mathrm{thres}} = 0.27 - 0.145 \cdot \theta + 0.00218 \cdot \theta^2 \quad [\mathrm{KB00}], \tag{4.5}$$

with the angle θ given in degree.
In the PbSc calorimeter, a different approach is used. The shower shape cut is based on a comparison of the deposited energy in each module of the measured cluster to the expectation for a cluster formed by an electromagnetic shower of the same cluster energy. To measure the variation of the energy deposit from the expectation, the χ^2 distribution is determined. Clusters in the PbSc are only analysed if $\chi^2 < 3$. The determination for the χ^2 is discussed in [KB04].
Another cut to reject hadrons is the energy cut. Only particles above a threshold energy of $E > 0.2$ GeV are considered. In this analysis, four PID definitions are used and are summarised in Table 4.2.

		PbGl	**PbSc**
PID 0	no cut		
PID 1	energy cut	E > 0.2 GeV	E > 0.2 GeV
PID 2	shower-shape cut	dispersion cut	χ^2 cut
PID 3	energy + shape cut	PID 1 & PID 2	PID 1 & PID 2

Table 4.2: The table lists the four different PID definitions which are used in the analysis for the PbSc and the PbGl sector.

5. Pion Analysis

In this analysis, neutral pions in deuteron-gold collisions at $\sqrt{s_{\mathrm{NN}}} = 200$ GeV are studied. This chapter includes the several analysis operations and corrections that are used to obtain the invariant yield of neutral pions over a large p_{T} range from the information described in Chapter 4.

5.1 Pions

The π-mesons are the lightest mesons in particle physics and consist of two quarks. The pions form an isospin-triplet of three pions: π^0, π^+, π^-. The composition in the quark model for the π^+ is an up and an anti-down quark while the π^- is composed of a down and an anti-up quark. Both have a mass of 139.57 MeV/c^2. Moreover, the π^0 is a superposition of the down anti-down and up anti-up quark combination. Thus a neutral pion is its own anti-particle. Its mass is 134.98 MeV/c^2:

$$|\pi^+\rangle = |u\bar{d}\rangle, \tag{5.1}$$

$$|\pi^-\rangle = |\bar{u}d\rangle, \tag{5.2}$$

$$|\pi^0\rangle = \frac{1}{\sqrt{2}}[|u\bar{u}\rangle - |d\bar{d}\rangle]. \tag{5.3}$$

The pions show different lifetimes due to different decay processes. On the one hand, the π^+ and π^- mainly decay through the weak interaction into an anti-muon + muon neutrino and muon + muon anti-neutrino (99.9877%), respectively. On the other hand, the π^0 decays into two photons (98.798%) and into a photon and an electron-positron pair (1.198%) via the electromagnetic interaction. The charged pions have a mean lifetime of $2.6 \cdot 10^{-8}$ s. Neutral pions have a mean lifetime of $8.4 \cdot 10^{-17}$ s [APDG09].
In this analysis only neutral pions are studied via the measurement of their decay photons in the EMCal: $\pi^0 \rightarrow \gamma + \gamma$. Due to its very short lifetime, the particle decays before escaping from the collision point. Thus the π^0 can be reconstructed via the measurement of the decay photons with the EMCal.

5.2 Invariant mass of π^0

Particles with a short lifetime, like the neutral pion, can be measured via the reconstruction of the invariant mass if the momentum and the energy of the decay particles are known. The decay particles in the case of π^0's are two massless photons. Their energy and opening angle θ are known by the measurement with the EMCal. The invariant mass M_{π^0} can be calculated with the four momentum P and the fact that photons are massless particles via the following equation:

$$M_{\pi^0}^2 = (\sum_{\mathrm{i}} P_{\mathrm{i}})^2 = (P_{\gamma_1} + P_{\gamma_2})^2 = 2 \cdot E_{\gamma_1} E_{\gamma_2} (1 - \cos(\theta)),$$
$$M_{\pi^0} = \sqrt{2 \cdot E_{\gamma_1} E_{\gamma_2} (1 - \cos(\theta))}. \tag{5.4}$$

5.3 Asymmetry Cut

Two photons are combined to calculate the invariant mass. There are combinations of photons which do not originate from the decay of a single π^0. Hence, because of the combination of all possible photon-photon pairs, a huge combinatorial background results.

A possibility to reduce the background is to regard the phase space distribution of the decay photons of the neutral pion. In this context, the asymmetry between the energies of the decay photons is determined:

$$\alpha = \left| \frac{E_1 - E_2}{E_1 + E_2} \right|, \tag{5.5}$$

where E_1 and E_2 are the energies of the two decay photons.

The asymmetry distribution is expected to be flat whereas the distribution of uncorrelated photons exhibits a non flat distribution. Particles show a steep falling spectrum which leads to a higher probability for pair combinations containing a low energetic photon. Thus the distribution for photons with large asymmetry will increase.

Cutting off pair combinations with an asymmetry above a certain value would reject such uncorrelated pairs. Nevertheless correlated pairs will be discarded but overall the amount of uncorrelated pairs is still much larger. In this analysis an asymmetry cut is applied where only pair combinations with $\alpha < 0.7$ are accepted. This value offers a good signal to background ratio and is chosen based on older analyses, e.g. [Awe01a].

5.3.1 Sector Combinations

Information in the DSTs is processed using different sectors of the EMCal to determine the π^0 spectra for special sector combinations. The sectors and sector combinations of the EMCal, for which the invariant mass has been generated, are shown in Figure 5.1 and Table 5.1.

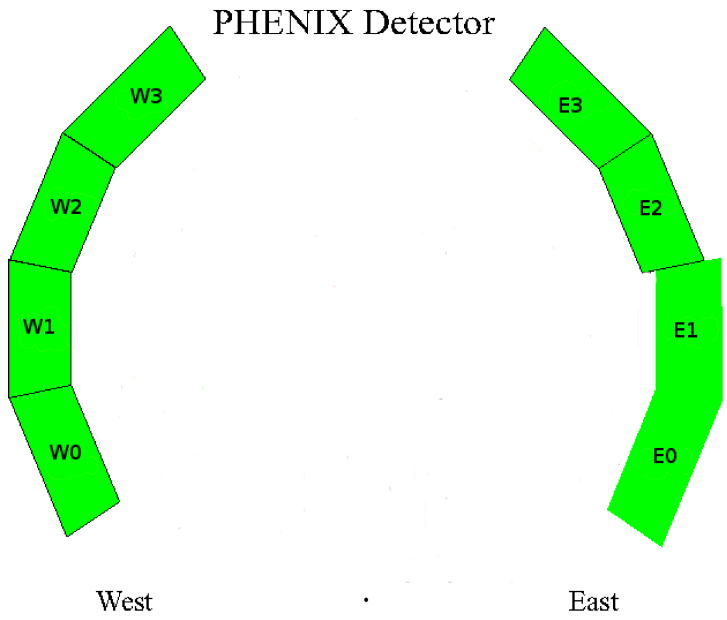

Figure 5.1: Beamview of the EMCal and sector denotation.

The analysis of the π^0's is done for the PbGl and PbSc separately and neither combinations between the east and west arm nor combinations between PbSc and PbGl are considered. Due to different properties of the two EMCal setups, the separate analysis offers the opportunity to compare the results for PbSc and PbGl as a cross check.

5.4 π^0 Yield Extraction

The analysis for the extraction of π^0-mesons is done with the same program as presented in [Awe01b] and [KB03]. The necessary information about the reaction system and centrality classification has been implemented and added to the existing macros.
The information in the DSTs is extracted with respect to all possible sector combinations, PID cuts, and the asymmetry cut and are merged into various histograms.

	E0	E1	E2	E3	W0	W1	W2	W3		sector	number
E0	**1**	**3**	8	8	7	7	7	7		**E0**	**1**
E1	**3**	**2**	8	8	7	7	7	7		**E1**	**2**
E2	8	8	**4**	**4**	7	7	7	7		**E0E1**	**3**
E3	8	8	**4**	**4**	7	7	7	7		**ScE**	**4**
W0	7	7	7	7	**5**	**5**	**5**	**6**		**W012**	**5**
W1	7	7	7	7	**5**	**5**	**5**	**6**		**W3W012**	**6**
W2	7	7	7	7	**5**	**5**	**5**	**6**		EW	7
W3	7	7	7	7	**6**	**6**	**6**	**6**		ScGl	8

sector	combinations	number
PbGl	**E0, E1, E0E1**	**1, 2, 3**
PbSc	**ScE, W012,W3W012**	**4, 5, 6**

Table 5.1: Overview of the analysed sector combinations and the composition of PbGl and PbSc.

In addition this classification is done for real as well as for mixed events which will be discussed in Section 5.4.1. Two examples of a control output are shown in Figures 5.2 and 5.3. The important analysis steps will be discussed in the following subsections.

5.4.1 Event Mixing Method

The photon invariant mass distribution contains a huge fraction of background which must be subtracted. In order to eliminate the combinatorial background, it must be described as realistic as possible. A well-established method to describe the combinatorial background is the event mixing method. Photons of different events cannot be correlated. Therefore, the combination of two photons from different events gives a distribution of uncorrelated photon pairs which is very similar to the combinatorial background from pairs of the same real event. Hence, the invariant mass distributions are calculated for *real* events, two photons combined from the same event, and for *mixed* events, two photons from two different events. To describe the combinatorial background correctly, it is important that the events used for the mixing have similar properties to the real event. For the event mixing in PbSc and PbGl, five

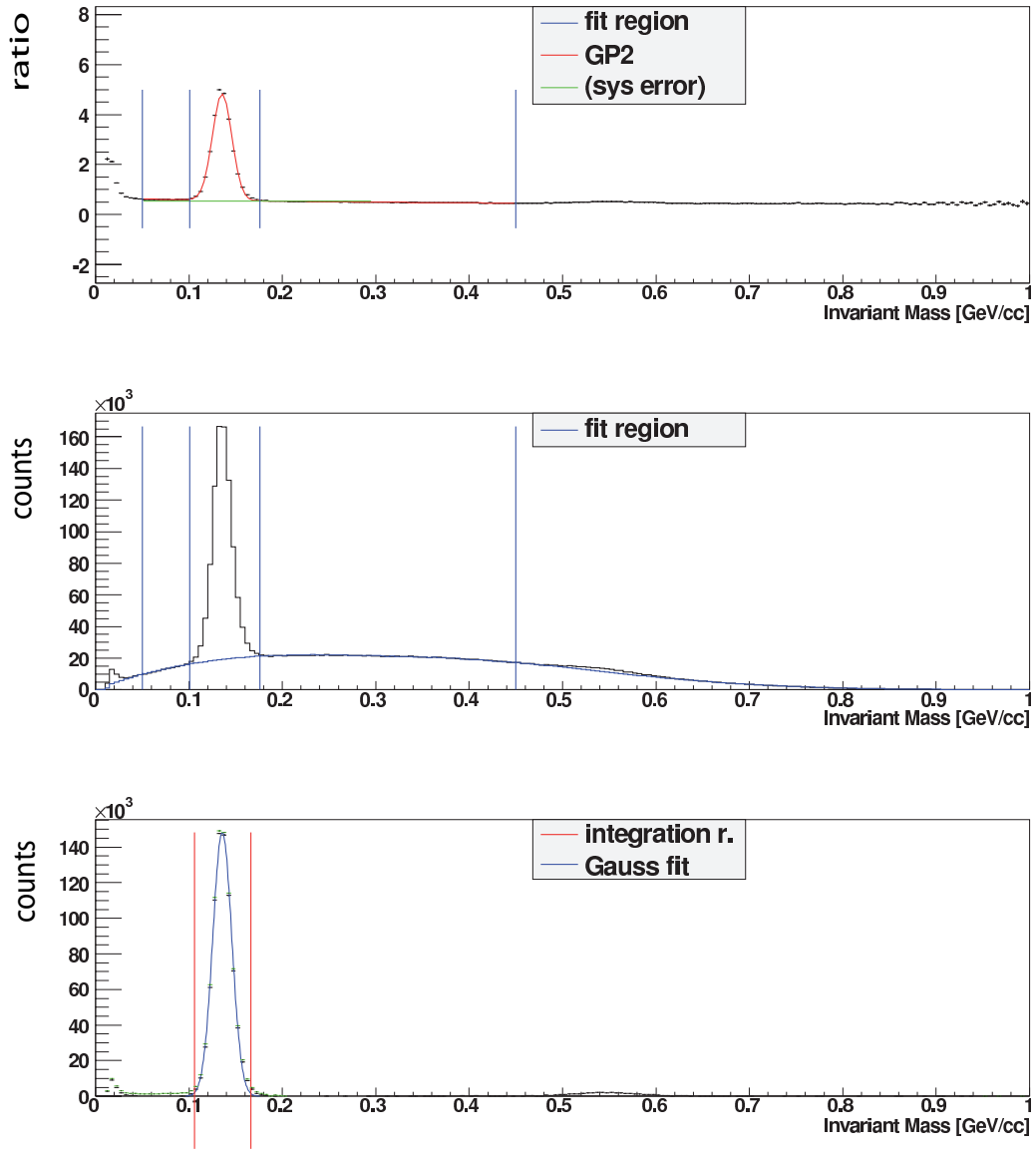

Figure 5.2: Sample control output of the program for π^0 extraction for minimum bias triggered data of the PbGl for 2 GeV/c < p_{T} < 2.5 GeV/c. In the top panel, the real/mixed events ratio is shown. The middle panel shows the invariant mass distribution for real events and for the scaled background from mixed events. The bottom panel shows the π^0-peak and integration region after the background subtraction.

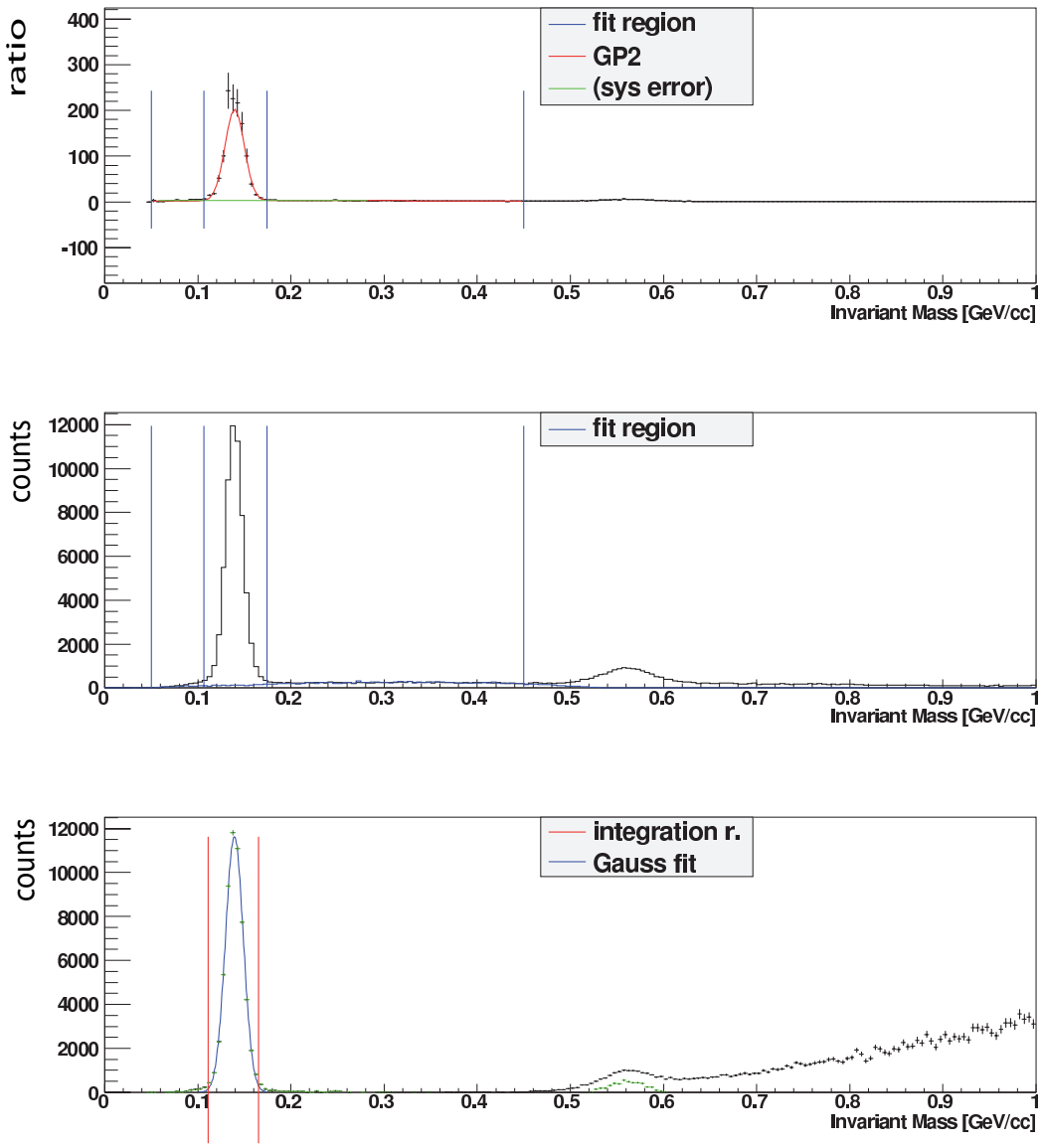

Figure 5.3: Sample control output of the program for π^0 extraction for ERT triggered data of the PbSc for 8 GeV/c < p_{T} < 8.5 GeV/c. In the top panel, the real/mixed events ratio is shown. The middle panel shows the invariant mass distribution for real events and for the scaled background from mixed events. The bottom panel shows the π^0-peak and integration region after the background subtraction.

vertex classes are defined. If events from different vertices were used, a significant difference between the true combinatorial and the constructed background would occur due to opening angles between photon pairs larger than the maximum opening angle from one event. Therefore, events are only mixed within the same vertex class. The momenta of the photons are recalculated for the determination of the invariant mass with respect to the mixed vertex z_{m}:

$$z_{\mathrm{m}} = \frac{z_{\mathrm{old\_event}} + z_{\mathrm{current\_event}}}{2}. \tag{5.6}$$

5.4.2 π^0 Peak Extraction

The data contains information about the invariant mass, the transverse momentum, and the number of counts for 0 GeV/c < p_{T} < 32 GeV/c. At first, the π^0-peaks must be extracted. This is realised with the projection of the number of counts of a certain transverse momentum range on the invariant mass axis. Afterwards, the background needs to be extracted to determine the π^0-peak.
The combinatorial background is estimated via the event mixing method as described above.
Real and mixed events show a different number of pair combinations per event:

$$\frac{n_{\gamma,\mathrm{i}} \cdot (n_{\gamma,\mathrm{i}} - 1)}{2} \quad \rightarrow \text{ real events,} \tag{5.7}$$

$$n_{\gamma,\mathrm{i}} \cdot n_{\gamma,\mathrm{j}} \quad \rightarrow \text{ mixed events.} \tag{5.8}$$

The mixed events distribution has to be subtracted from the distribution of real events. First the distribution of the real events is divided by the mixed event distribution to estimate the scaling of the background. This ratio is shown in Figure 5.2 and Figure 5.3 in the top panel. A π^0-peak can be seen in the invariant mass region of about 138 MeV/c^2 which is close to the mass of the neutral pion.
The peak maximum is shifted to a higher value (compared to m_{π^0}=134.98 MeV/c^2 [APDG09]) because of detector effects which cause energy smearing and because of the steep falling spectrum. This smearing of the photon energies occurs due to the energy resolution of the detector. The result is a broadened signal of the neutral pion.
The ratio of real and mixed events is fitted by a second order polynomial together with a Gaussian function (red line) in the region marked by the outermost blue vertical lines. The interval of the background adaption is limited to the region between 0.05 MeV/c^2 and 0.45 MeV/c^2, as shown in Figures 5.2 and 5.3. Just

the polynomial part of the whole fit function is interesting for the background scaling and therefore only the parameters of the polynomial are used to scale the background. This parametrisation is chosen because the background is falling from lower to higher invariant mass values. The curvature towards the peak position is taken into account via the Gaussian function. Furthermore, different approaches showed that the used fit function describes the background slightly better than just a simple second order polynomial or a linear fit.

To obtain the systematic uncertainty[1] that occurs due to the background scaling, the spectrum is further fitted with a linear function (green line in the top panel) instead of the Gaussian together with a second order polynomial. Therefore, the peak region must be excluded. The depleted area intervals depend on two input parameters: the pion peak position m and its width σ. The peak region of $m - 3.5\sigma$ and $m + 4\sigma$ is excluded for the fit, marked by the inner vertical blue lines[2]. The values for m and σ are derived from fitting the mass m and the width σ of the measured π^0's as a function of the transverse momentum for certain centrality classes and sector combinations. Hence, the values are estimated for the first peak extraction run and the final values are derived from the fittings of the functions described above. Therefore, at least one peak extraction needs to be run to get the right parameters for the position and width of the neutral pion. This procedure is used in preference to extrapolation processes because these provided values describe the real data more precisely.
In order to achieve satisfactory parameters, this procedure passes an iterative process.

At higher transverse momentum ranges, one can see that the background vanishes and an estimation via the fit would lead to large uncertainties. For these p_{T} ranges, the fit is replaced by the ratio of the number of pair combinations of the real and the mixed events distribution in the normalisation region.
The distribution of mixed events is scaled with the fit parametrisation or with the constant for high p_{T}, respectively. The real event distribution together with the scaled mixed events distribution is shown in the middle panel of Figures 5.2 and 5.3.

[1] The systematic uncertainty will be discussed in Section 5.6.2.

[2] This region is also excluded when the background is scaled with a polynomial of second and lower orders.

Finally, the real event distribution with subtracted background is presented in the lower panel of Figures 5.2 and 5.3. The number of neutral pions is determined via counting the content of a predefined integration interval. The integral of the invariant mass distribution is determined in the region of $m = \pm 3\sigma$.
In this analysis, the peak extraction is done with different binning in p_{T}. Towards the final spectrum, this procedure is useful to obtain results up to highest p_{T}. At low p_{T}, a large amount of π^0's is available and a fine binning is used, while at higher p_{T}, a larger binning is preferred due to a small number of π^0's. The finest bin width is chosen as 0.5 MeV/c, it is increased up to a bin width of 2 MeV/c.

5.5 Corrections

After the peak extraction, the number of pions is determined and the raw yield for a range of 0 GeV/c $< p_{\mathrm{T}} <$ 32 GeV/c is generated. However, several corrections have to be applied to get reliable results. The geometry and therefore the acceptance and the efficiency of reconstructing neutral pions have to be considered and corrected towards the final spectrum, relating to the EMCal. In addition, physical phenomena such as the probability of the conversion of a photon into an e^+e^--pair between the vertex and the EMCal, the merging of cluster towards high transverse momenta, and the branching ratio of the π^0's must be included in the analysis. A bin-shift correction is necessary because the spectra of the neutral pions are falling steeply with increasing p_{T}. Finally, a so-called centrality bias correction must be taken into account as discussed in [Tan03, Dre03]. All necessary corrections and their implementation into the analysis will be discussed in the following.

5.5.1 Monte Carlo Simulation

To calculate the geometrical acceptance and the reconstruction efficiency of the PHENIX EMCal, a *Fast Monte Carlo Simulation*[3] (fastMC) is used with the routines of the JetSet library [Sjo94]. The fastMC simulates particles with the following characteristics:

- a linear rapidity distribution: $f(y) = 19.75 - 2.5 \cdot y$ with $|y| \leq 0.45$ [Aph03a],

[3] A Monte Carlo Simulation simulates events with given parameters and properties with the aid of random numbers

- a flat vertex distribution with -30 cm $\leq z \leq 30$ cm,
- a flat p_{T} distribution with: 0 GeV/c $< p_{\mathrm{T}} <$ 32 GeV/c,
- a uniform ϕ distribution.

The rapidity distribution of π^0's is described with a linear function because of the asymmetric system of deuteron and gold ions.

In order to simulate the properties of the detector in the right way, the detector effects like energy smearing or the PID cuts have to be considered in the fastMC. Therefore, it is essential to include information on the shape of the spectrum of the measured data in the simulation.
For a correct simulation, an input spectrum is required which is the real spectrum of the d+Au measurement. Moreover, the information on the peak position and peak width of the measured data is implemented to obtain the same integration window as in the real data. The simulations of the following corrections are done separately for the PbSc and the PbGl and for the MinBias and ERT events, respectively.

Acceptance

The application of the acceptance correction $a_{\pi^0}(p_{\mathrm{T}})$ takes two properties of the detector into account. First, the detector coverage is limited. The EMCal only covers a rapidity range of $-0.35 < y < 0.35$ and π in azimuth. Second, not every module is active and provides measured data as discussed in Section 4.3.1. To determine the acceptance of the EMCal, the fraction of all π^0's that hit the detector surface must be determined and must be normalised to the number of emitted π^0's in the respective phase space interval. In detail, the acceptance is given by the fastMC where the fraction of the probability of two photons hitting the active area[4] $f_{\mathrm{active}}(p_{\mathrm{T}})$ and a flat p_{T} distribution of the neutral pions $f_{\mathrm{emit}}(p_{\mathrm{T}})$ is calculated:

$$a_{\pi^0}(p_{\mathrm{T}}) = \frac{f_{\mathrm{active}}(p_{\mathrm{T}})}{f_{\mathrm{emit}}(p_{\mathrm{T}})}. \tag{5.9}$$

The results of the geometrical acceptance calculation are shown in Figure 5.4. A strong dependence of the acceptance on the transverse momentum is observed. An

[4]The active area includes the information on bad modules as well as the geometric detector information.

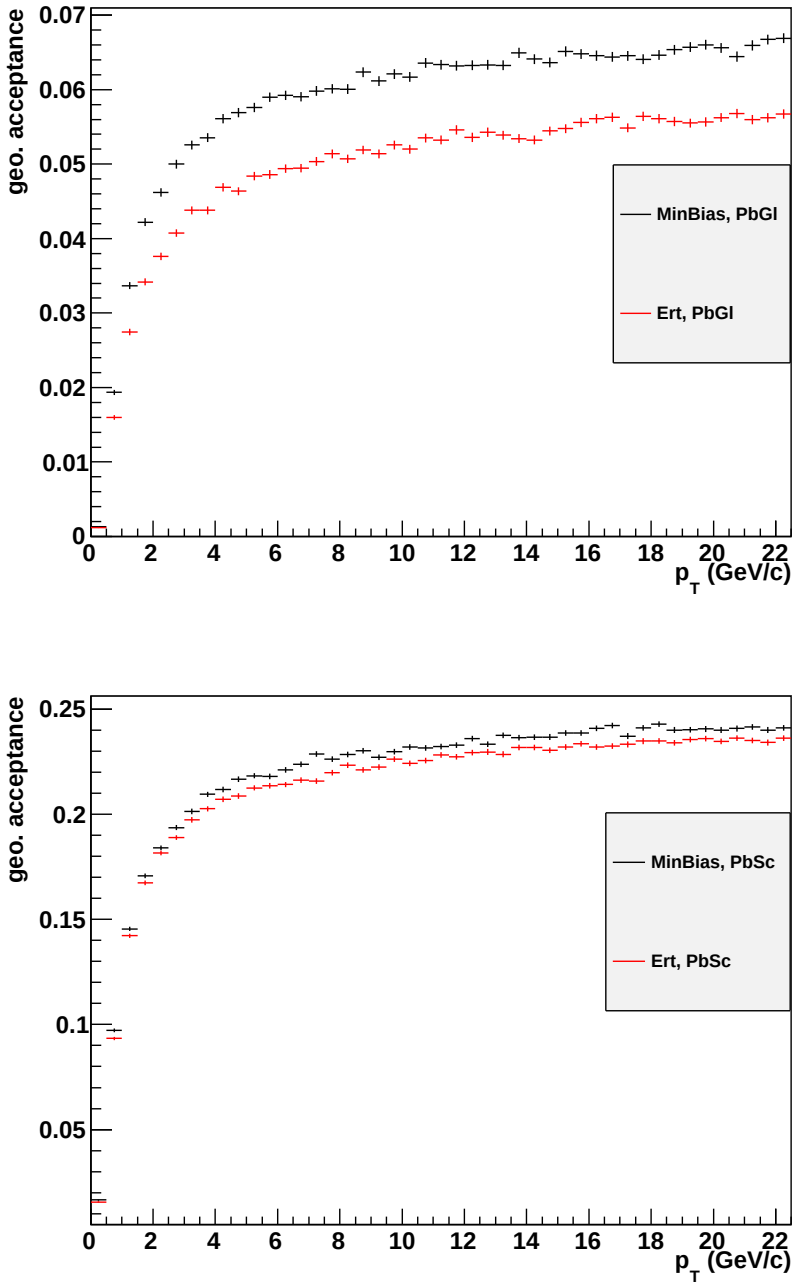

Figure 5.4: Geometric acceptance for π^0-mesons in PbSc and PbGl for MinBias and ERT triggered events.

explanation for this phenomenon is the increasing probability of both photons hitting the active surface of the EMCal with ascending transverse momentum because the opening angle of the decay photons becomes smaller. Therefore, it is more probable for photon pairs from a large momentum π^0 to hit the surface of the detector. A significant difference occurs between the PbGl and PbSc detector for the acceptance calculations. The acceptance in PbSc is larger because of the number of sectors and therefore a better coverage in ϕ. Additionally, the distance from the vertex is larger for the PbGl sectors which slightly decreases the rapidity coverage of the PbGl compared to PbSc.
The deviation between the ERT acceptance and the MinBias acceptance is due to the different bad module maps for ERT and MinBias events which decreases the ERT acceptance because of more rejected towers and hits, respectively.

Efficiency

Another correction provided by the fastMC is the reconstruction efficiency[5]. This efficiency $\epsilon(p_{\mathrm{T}})$ takes into consideration the difference between the physical input spectrum on the active detector surface $\mathrm{d}N/\mathrm{d}p_{\mathrm{T}}|_{\mathrm{input}}$ and the measured output spectrum $\mathrm{d}N/\mathrm{d}p_{\mathrm{T}}|_{\mathrm{output}}$. Thus the efficiency is determined via the ratio of the output and the input spectrum:

$$\epsilon(p_{\mathrm{T}}) = \frac{\frac{\mathrm{d}N}{\mathrm{d}p_{\mathrm{T}}}|_{\mathrm{output}}}{\frac{\mathrm{d}N}{\mathrm{d}p_{\mathrm{T}}}|_{\mathrm{input}}}. \tag{5.10}$$

Reasons for the difference between the input and output spectra can be found in the application of the PID and the analysis cuts. Moreover, the position and energy resolution of the EMCal detectors and the multiplicity[6] of a reaction causes a difference between the input and the output spectra. Therefore, particles with large transverse momentum deposit their energy at greater depth of the detector. In addition, clusters that hit the detector in an askew angle at the edges would not even be measured. Thus the efficiency will show a decreasing behaviour for larger p_{T}.

To simulate detector effects, the energy and position information on a particle have

[5] In the following denoted just as efficiency.
[6] Especially in d+Au collisions the multiplicity is of no relevance.

to be smeared. The parametrisation is chosen to be a function with an energy dependent term A and with a constant term B:

$$\sigma_E/E = \frac{A}{\sqrt{\frac{E}{\mathrm{GeV}}}} \oplus B. \tag{5.11}$$

To evaluate the correct parameters for the energy smearing, measured data of a calibration scan with a sharp asymmetry cut of $\alpha < 0.2$ has been used. Different parameters are tested until the peak positions and widths of the data and of the simulations show an adequate agreement. The parameters have been determined to the values presented in Table 5.2.

detector subsystem	**energy dependent term A**	**constant term B**
PbGl	0.073	0.070
PbSc	0.082	0.051

Table 5.2: Parameters used for energy smearing in the fastMC code.

The yield of π^0's is falling steeply towards higher transverse momenta. Hence, the centre of each bin does not represent the average value any more and the simulated spectrum of the pions has to be weighted with the real spectrum of the neutral pions. At the beginning of the analysis, the spectrum is not known. This problem is solved by assuming the expected spectra for the first pass, e.g. of older analyses or the raw yield. The analysis is done with the obtained efficiency correction which leads to a new distribution. This distribution is the baseline for a new simulation. Further iterations of this procedure lead to a convergence, which means that the spectrum used for the weighting is sufficiently consistent with the final spectrum of the analysis.
The determination of the efficiency also takes into account the PID cuts. In the simulation, the loss of photons and therefore the loss of neutral pions due to energy and dispersion cuts must be implemented. The dispersion cut is estimated with the ratio $p^{\pi^0}_{\mathrm{surv}}$ of the π^0 spectrum without any cut and the spectrum with the PID 2 cut applied. An example for the PbGl calorimeter for MinBias data is shown in Figure 5.5.

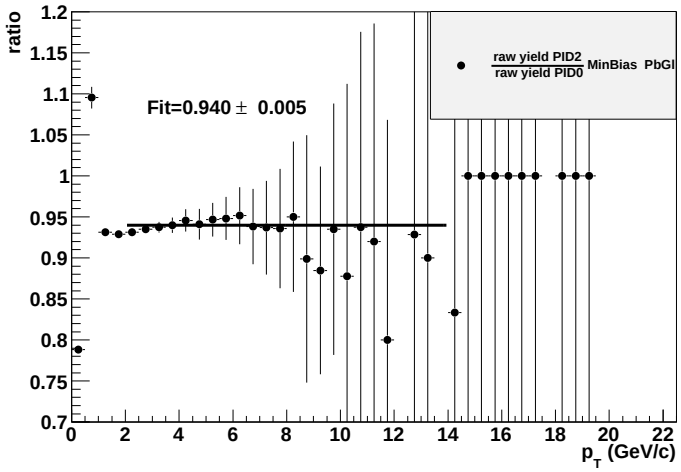

Figure 5.5: The ratio of the PID2 and PID0 cut of the raw π^0 spectrum. The fit is used to determine the survival probability of the PID2 cut for the simulation.

The result of this ratio is interpreted as the probability of the photons to survive the cut and is implemented in the fastMC. Therefore, the photon survival probability p^{γ}_{surv} is determined as:

$$p^{\gamma}_{\text{surv}} = \sqrt{p^{\pi^0}_{\text{surv}}}. \tag{5.12}$$

The energy cut is realised via rejecting simulated hits below an energy threshold of $E < 0.2$ GeV.

As discussed above, the spectrum of the π^0 analysis is needed in the simulation. Moreover, the information on π^0 peak positions as well as the width is taken into account in the fastMC. Only pions which lie in the integration window of $\pm 3\sigma$ are accepted in the simulation. This value is chosen due to the peak integration window, discussed in Section 5.4.

The results of the efficiency calculations for the PbSc and PbGl are shown in Figure 5.6.

Results of simulated peak positions and peak widths of the fastMC are shown in Figures 5.7 and 5.8 as a comparison with the measured data for the MinBias scan and for all centrality classes. The comparisons of measured data and simulation data for all centrality classes, sector combinations, and trigger conditions are presented in Appendix E.

In the Figure 5.7, a deviation in the position between the data points of the peak extraction and the simulation can be observed. This effect is due to a not optimal

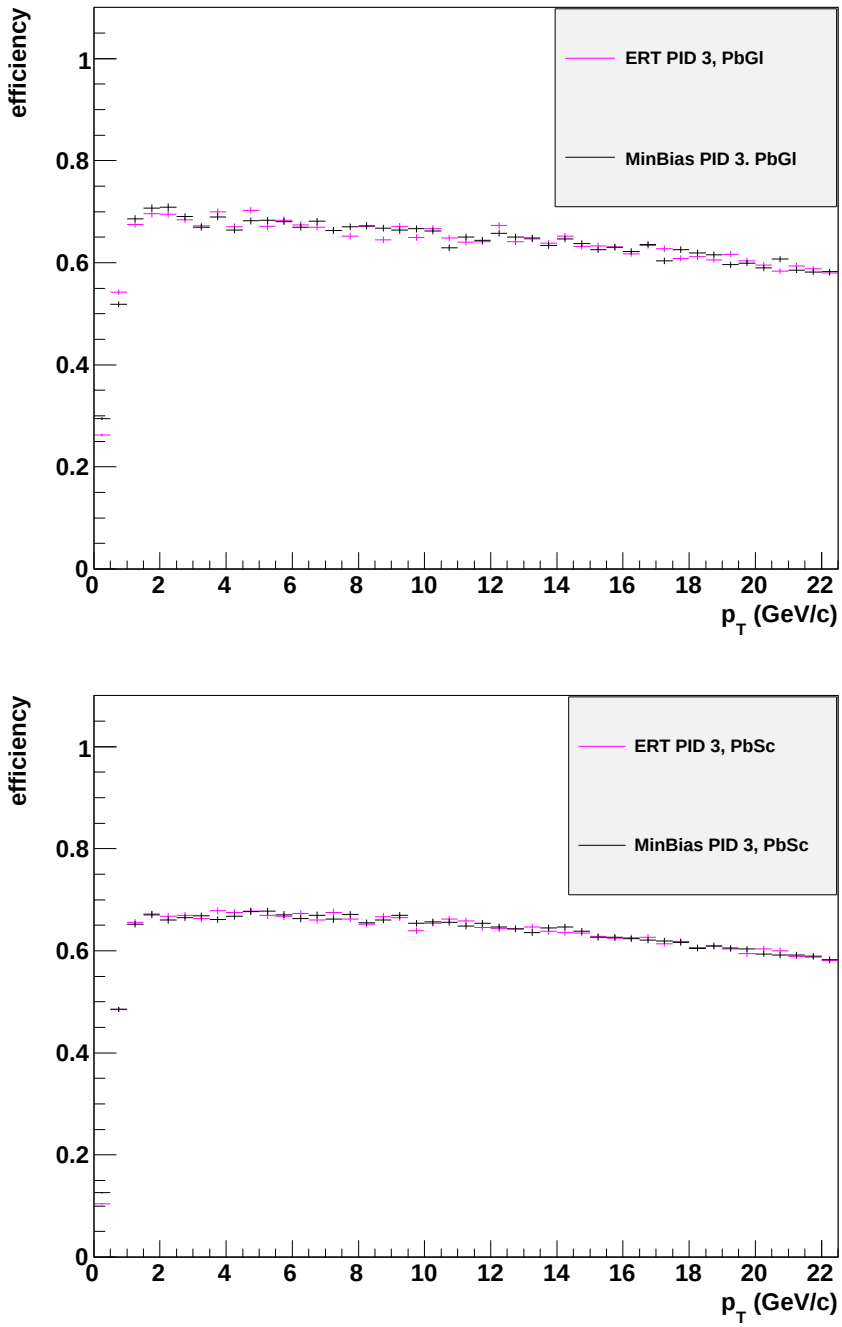

Figure 5.6: The result of the efficiency calculation with the fastMC simulation for π^0-mesons in the PbGl (upper panel) and PbSc (lower panel).

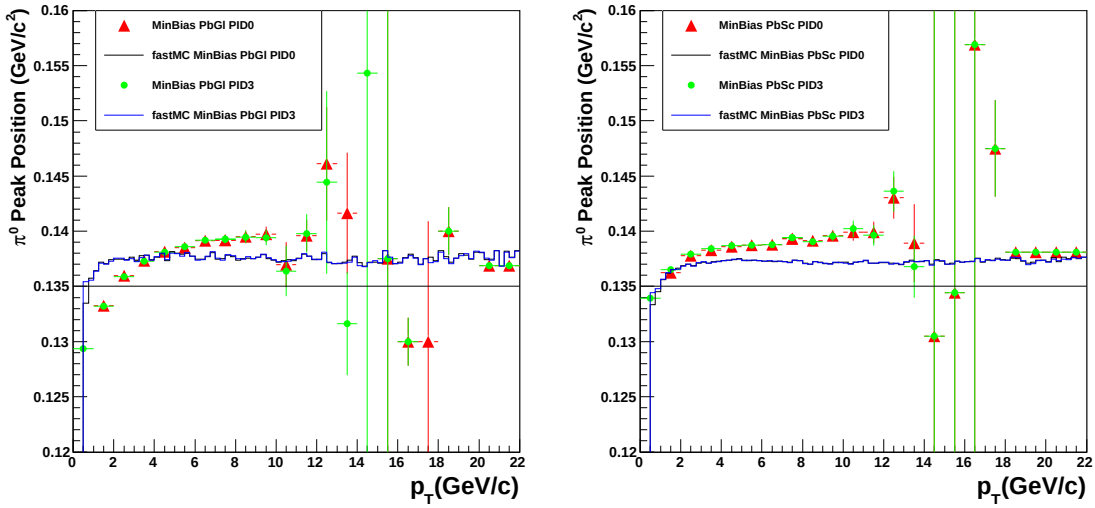

Figure 5.7: Comparison of the π^0 peak position from the fastMC simulation and from the measured data for MinBias triggered events. The black (PID0) and the blue (PID3) lines show the results of the simulation. The red (PID0) and green (PID3) points depict the peak position of the measured data. The straight line at 135 MeV/c^2 marks the nominal mass of the π^0. In the left column, the result for the lead glass calorimeter is shown. The right column shows the result of the lead scintillator.

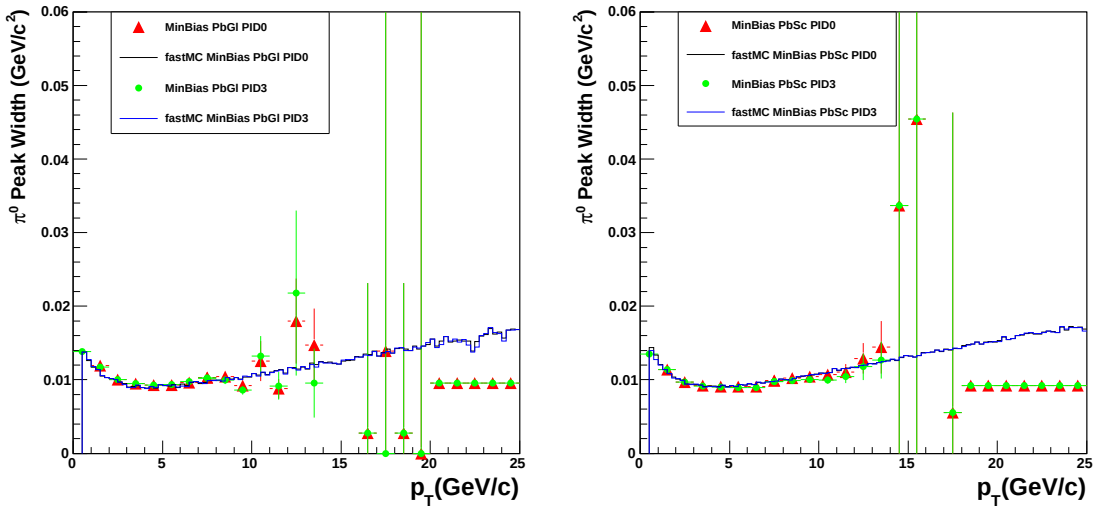

Figure 5.8: Comparison of π^0 the peak width from the fastMC simulation and from the measured data for MinBias triggered events. The black (PID0) and the blue (PID3) lines show the results of the simulation. The red (PID0) and green (PID3) points depict the peak width of the measured data. In the left column the result for the lead glass calorimeter is shown. The right column shows the result for the lead scintillator.

energy scaling and has to be corrected. Therefore, a correction is proposed, in which the calibration scan is used to determine the relative deviation $f_{\mathrm{rel}}(p_{\mathrm{T}})$ between the data $f_{\mathrm{data}}(p_{\mathrm{T}})$ and the simulation $f_{\mathrm{sim}}(p_{\mathrm{T}})$ for each single Sector of the EMCal. This correction should be applied in future scans.
The relative deviation is determined with Equation 5.13 and the results are fitted with a constant to quantify the correction.

$$f_{\mathrm{rel}}(p_{\mathrm{T}}) = \sqrt{\left(\frac{f_{\mathrm{data}}(p_{\mathrm{T}})}{f_{\mathrm{sim}}(p_{\mathrm{T}})} - 1\right)^2} \tag{5.13}$$

Examples of the determination of the correction for the PbSc and PbGl sector parts are shown in Figures 5.9 and 5.10. All results of the scaling correction are listed in Table 5.3.

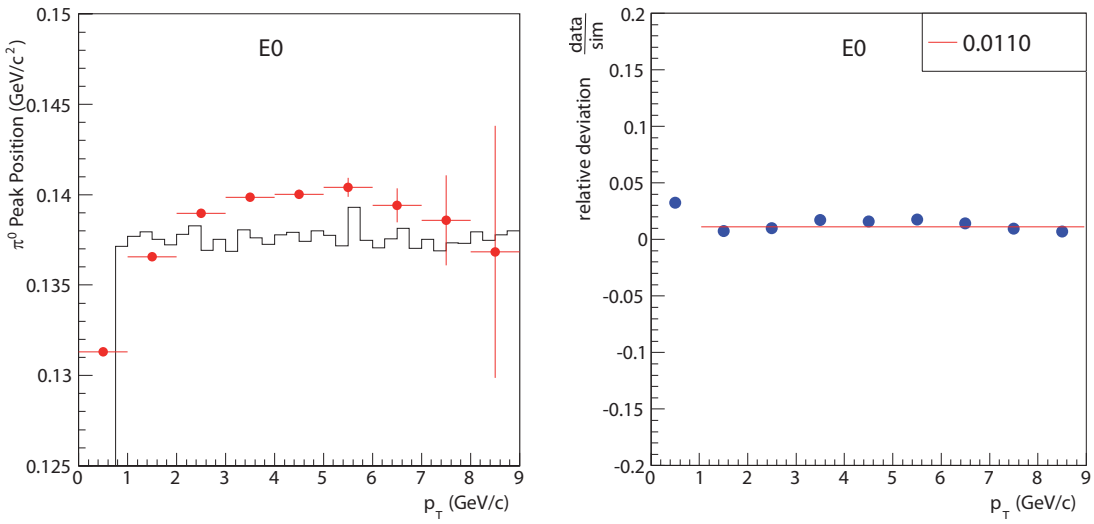

Figure 5.9: Comparison of the π^0 peak position from the fastMC simulation and from the calibration scan for the E0 sector of the PbGl. The results are shown in the left panel. The red dots represent the data and the black line represents the results of the simulation. The relative deviation from the ratio of the data point and the simulation is depicted in the right panel. This ratio (blue dots) is fitted with a constant (red line).

5.5.2 Trigger Efficiency

For the final spectrum, the MinBias and ERT data have to be combined to cover the entire p_{T} range. In this context, it is important to pay attention to the difference of

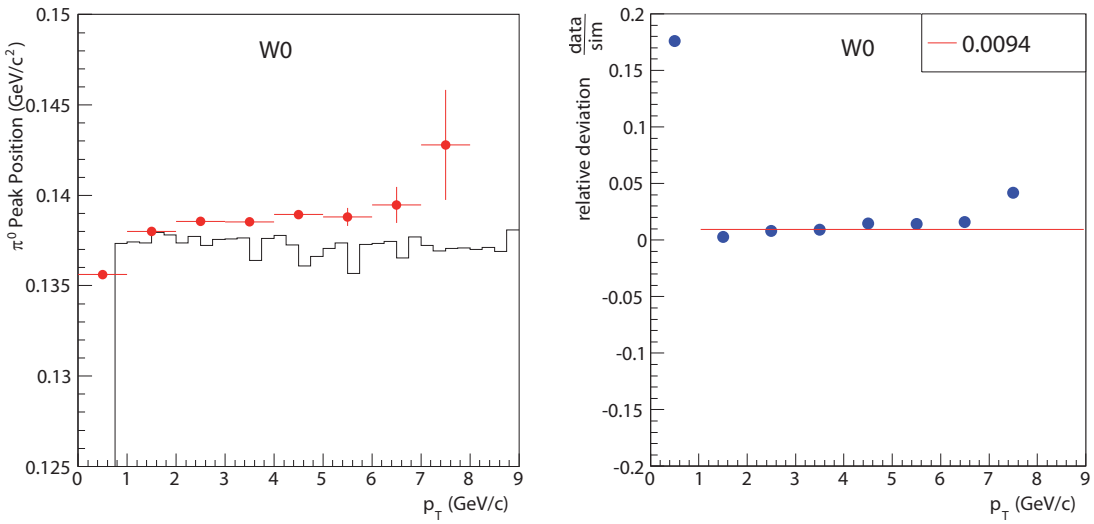

Figure 5.10: Comparison of the π^0 peak position from the fastMC simulation and from the calibration scan for the W0 sector of the PbSc. The results are shown in the left panel. The red dots represent the data and the black line represents the results of the simulation. The relative deviation from the ratio of the data point and the simulation is depicted in the right panel. This ratio (blue dots) is fitted with a constant (red line).

	Sector	relative deviation / correction
PbGl	E0	1.10%
	E1	1.46%
PbSc	E2	0.15%
	E3	1.41%
	W0	0.94%
	W1	1.58%
	W2	2.00%
	W3	1.99%

Table 5.3: Overview of the proposed future correction for the deviation of the peak position between data and simulation.

the bias of MinBias and ERT triggered events. In case of ERT events, the EMCal acts as a detector and as trigger.
Besides the difference of the number of events which is affected by scale down conditions, described in Section 4.1, the influence of the EMCal as a trigger becomes obvious when comparing ERT events scaled with underlying MinBias events to MinBias events:

$$\frac{\epsilon_{\text{trig}}^{\text{ERT}} \cdot N^{\text{mb\&ERT}}}{N^{\text{mb}}}, \tag{5.14}$$

with $\epsilon_{\text{trig}}^{\text{ERT}}$ from Equation 4.1.
Instead of a sharp energy cut-off at the energy thresholds of 2.8 GeV for PbGl and 3.5 GeV for PbSc (see Table 3.1), respectively, a slow increase over a range of 2-8 GeV/c can be observed (see Figure 5.11).
This development of the values expresses the deviation of the hit energy provided by offline clustering and the sum of a 4×4 tile. After the increase in the energy dependent trigger efficiency, a plateau at unity is expected where the full efficiency is reached. Due to active modules which lie in masked FEMs, the trigger efficiency is limited to the so-called geometrical limit $\epsilon_{\text{geom}}^{\text{trig}}$. The number of active modules is denoted as $N_{\text{mod}}^{\text{active}}$ and the number of active modules lying within a masked FEM is denoted as $N_{\text{mod}}^{\text{active\&masked}}$. The geometrical limit for the ERT trigger efficiency $\epsilon_{\text{geom}}^{\text{trig}}$ is given in the following equation:

$$\epsilon_{\text{geom}}^{\text{trig}} = 1 - \frac{N_{\text{mod}}^{\text{active\&masked}}}{N_{\text{mod}}^{\text{active}}}. \tag{5.15}$$

The numbers of active and masked modules are calculated using the active tower map and the FEM maps shown in the Appendix D. The geometrical limit for the PbGl is determined to be 100% and the limit for the PbSc is 97.12%. An overview of the values of the geometrical limit for each sector is given in Table 5.4.
The efficiency determined by comparing π^0's of minimum bias events with triggered data is shown in Figure 5.11 for PbSc and PbGl.
Considering the results given in Figure 5.11, the transition point – where the different triggered events are combined – is chosen as $p_{\text{T}} = 7.5$ GeV/c.

Trigger Efficiency Correction

The trigger becomes fully efficient at 7.5 GeV/c (see Figure 5.6). Because the ERT triggered data is considered for $p_{\text{T}} \geq 7.5$ GeV/c for the final combined spectra of

sector	$N_{\text{mod}}^{\text{active}}$	$N_{\text{mod}}^{\text{active\&masked}}$	$\epsilon_{\text{geom}}^{\text{trig}}$
E0	3708	0	100%
E1	3754	0	100%
PbGl	7462	0	100%
E2	2325	132	94.30%
E3	2219	0	100%
W0	2333	121	94.81%
W1	2298	0	100%
W2	2062	0	100%
W3	2151	132	93.50%
PbSc	13388	385	97.12%

Table 5.4: The table lists the results of the calculation of the geometrical limit for each sector of the PHENIX EMCal. The values are based on the information given in the ERT bad map and the FEM map in the Appendix D.

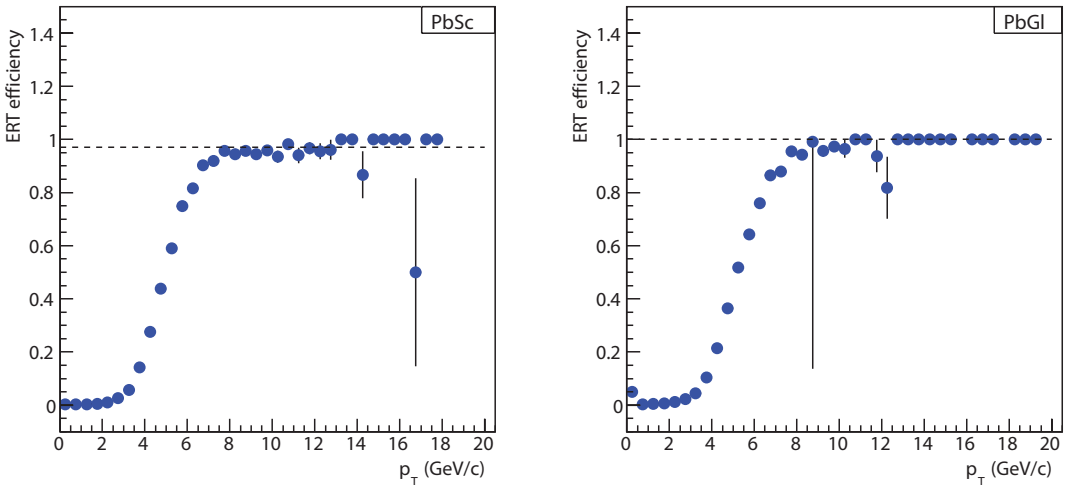

Figure 5.11: Trigger efficiency for both EMCal Sectors PbSc and PbGl. The dotted line marks the geometrical limit of the ERT trigger.

MinBias and ERT triggered data, a trigger efficiency correction does not have to be taken into account.

5.5.3 Shower Merging Correction

The angle between two decay photons originating from a π^0 becomes smaller for increasing p_{T} of the mother particle and the photons would be reconstructed as a single shower because of the limited position resolution of the EMCal. The effect of *merging showers* or *merging clusters* becomes noticeable for neutral pions above a transverse momentum of 10 GeV/c in the PbSc and above 15 GeV/c in the PbGl. The profile of such a merged shower is usually expanded compared to the shower of a single photon. Hence, the merged showers are rejected by the PID 2 cut. The PbGl calorimeter in this case is more beneficial because it has a finer granularity. This analysis contains measured pions which cover a momentum range above $p_{\mathrm{T}} = 10$ GeV/c, or $p_{\mathrm{T}} = 15$ GeV/c, and therefore the loss of π^0's due to merging showers has to be accounted for. The p_{T}-dependent probability of separating merged clusters is determined with a fast Monte Carlo simulation. The simulation takes into account the real EMCal geometry and the electromagnetic shower profile which is parametrised from test beam data [Bat05]. The separation probabilities of merging showers are shown in Figure 5.12. To correct the merging effect, the spectrum of the neutral pions has to be divided by this probability distribution for the PbSc and PbGl sector, respectively.

5.5.4 Bin Shift Correction

The data points of the π^0 spectrum lie in the centre of each bin whereas the data point, e.g. the bin, is related to the average yield. Because of the steep falling spectrum the average over a certain bin width does not represent the right value for the yield at the bin centre. In principle there are two ways to correct this effect via *bin shifting*. Either the data point is moved in x-direction to the position of the transverse momentum that corresponds to the yield of the data point or the point is moved in y-direction. In the case of the shift in y-direction the yield corresponds to the yield of the transverse momentum in the centre of the bin. During the analysis, ratios of different spectra are built and therefore it is useful to shift the bin in y-direction. In the analysis, the spectrum is described via a function $f_{\mathrm{spectrum}}(p_{\mathrm{T}})$,

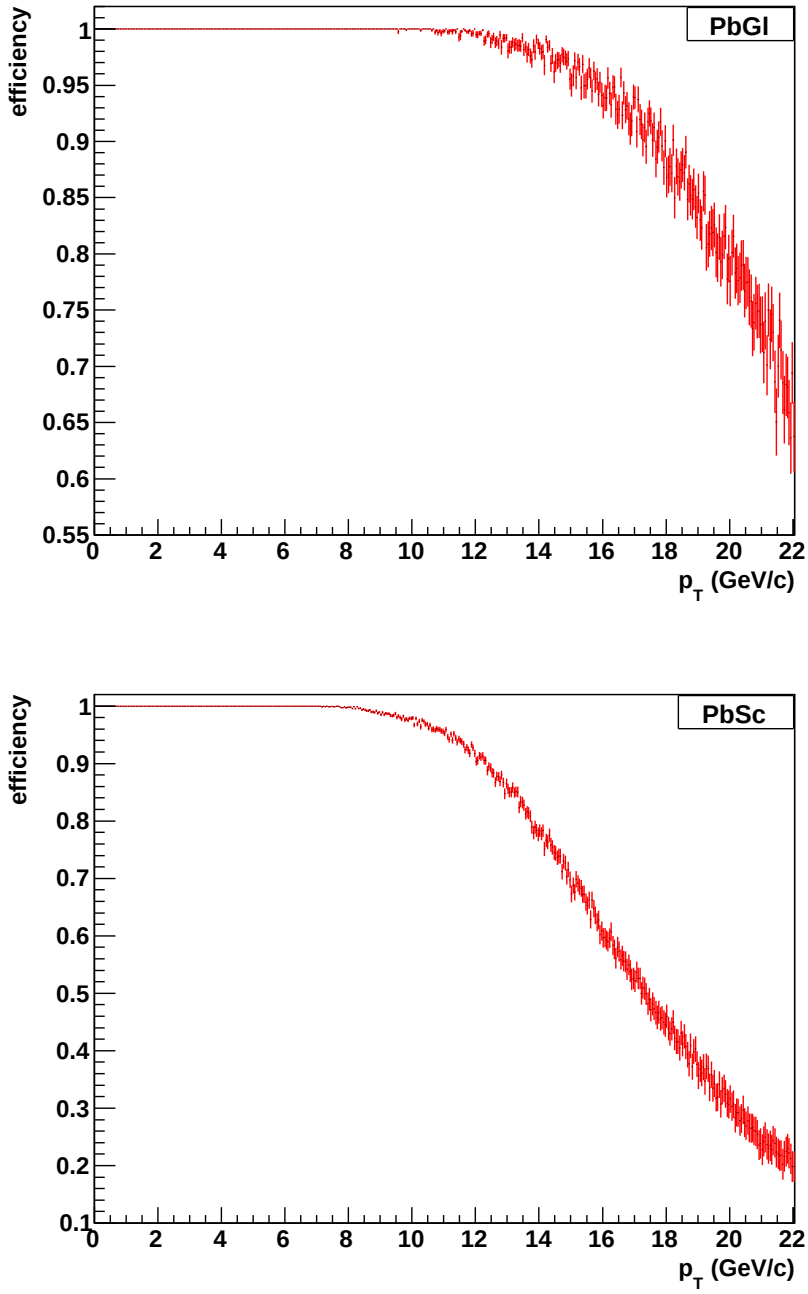

Figure 5.12: Shower merging correction for the PbGl (upper panel) calorimeter and the PbSc (lower panel) calorimeter.

composed of a Hagedorn-type parametrisation [Hag84] and a power law, connected with a Woods-Saxon type function $a_{\mathrm{WS}}(p_{\mathrm{T}})$ [Woo54]:

$$\begin{aligned} f_{\mathrm{spectrum}}(p_{\mathrm{T}}) &= a_{WS}(p_{\mathrm{T}}) \cdot a_0 \cdot \left(\frac{a_1}{a_1 \cdot p_{\mathrm{T}}}\right)^{a_2} \\ &\quad + (1 - a_{\mathrm{WS}}(p_{\mathrm{T}})) \cdot a_3 \cdot \left(\frac{1}{p_{\mathrm{T}}}\right)^{a_4}, \\ \text{with } a_{\mathrm{WS}}(p_{\mathrm{T}}) &= \frac{1}{1 + \mathrm{e}^{(\frac{p_{\mathrm{T}} - b_0}{b_1})}}. \end{aligned} \tag{5.16}$$

The parameters of a_{WS} are determined to $b_0 = 4.0$ and $b_1 = 0.194$.
This fit function 5.16 shows the best agreement with the spectrum. To determine the bin shift correction f_{corr} for a bin with the width Δp and the centre p_{c}, the integral of the fit function over the bin width, normalised to the bin width and the value of the fit function at the bin centre, is calculated:

$$f_{\mathrm{corr}} = \frac{\int_{p_{\mathrm{c}} - \frac{\Delta p}{2}}^{p_{\mathrm{c}} + \frac{\Delta p}{2}} f_{\mathrm{spectrum}} \mathrm{d}p_{\mathrm{T}}}{f_{\mathrm{spectrum}}(p_{\mathrm{c}})}. \tag{5.17}$$

After applying the correction, the function $f_{\mathrm{spectrum}}(p_{\mathrm{T}})$ is fitted again to the determined spectrum and the correction is repeated. This iterative procedure is applied in the analysis until the correction converges. Calculations show that four iteration steps are sufficient for an adequate accuracy. The corrected yield $\mathrm{d}N/\mathrm{d}p_{\mathrm{T}}\big|_{\mathrm{corr}}$ is given by:

$$\left.\frac{\mathrm{d}N}{\mathrm{d}p_{\mathrm{T}}}\right|_{\mathrm{corr}} = \frac{\left.\frac{\mathrm{d}N}{\mathrm{d}p_{\mathrm{T}}}\right|_{\mathrm{uncorrected}}}{f_{\mathrm{corr}}}. \tag{5.18}$$

5.5.5 Branching ratio

The probability for the neutral pions to decay in two photons has to be taken into consideration. Therefore, the spectrum has to be divided by the branching ratio for $\pi^0 \to \gamma\gamma$ with a value of (0.98798 ± 0.00032) [APDG09].

5.5.6 Conversion Correction

Photons can convert into e^+e^- in material after they have traversed a certain amount of matter, the radiation length X_0. Therefore, a correction has to be applied. The used values are extrapolated from [d'E04]. For the PbGl a value of (1.088 ± 0.02) and for the PbSc a value of (1.060 ± 0.02) is used.

5.5.7 Centrality Bias Correction

A problem regarding the determination of the centrality is a bias which appears by using any kind of trigger. It is for example known from p+p collisions that the BBC LVL1 trigger measures (52 ± 6)% of the real inelastic inclusive reactions, while (75 ± 2)% of all events containing π^0's are accepted in this trigger condition [Zha04].
This means that accepted events by the BBC are biased due to the centrality of a collision. For each centrality class, the average number of nucleon-nucleon collisions, N_{coll}, is calculated using a Glauber model [Dre03]. This number of binary nucleon collisions (N_{coll}) is important to determine the nuclear modification factor (see Section 2.5.1). Based on the values of p+p collisions, the bias for the different centrality classes in d+Au collisions can be determined using probability arguments under the assumption that d+Au collisions of a certain centrality range correspond to an ensemble of binary nucleon-nucleon collisions. Therefore, one corrects to the measured biased centrality class [Dre03]. The centrality bias correction is considered as presented in [Zha04] and the used values for the number of binary collisions as well as for the correction factors depending on the centrality class are shown in Table 5.5.

centrality class	N_{coll}	**uncertainty**	**bias correction**	**uncertainty**
0-20%	15.37	±1.0	0.95	±0.029
20-40%	10.63	±0.7	0.99	±0.007
40-60%	6.95	±0.6	1.03	±0.009
60-88%	3.07	±0.3	1.04	±0.027
0-88%	8.42	±0.3	0.94	±0.01

Table 5.5: Overview of the values for the number of binary collision and the centrality bias correction [Zha04].

5.6 Uncertainties

5.6.1 Statistical Uncertainties

During the determination of the number of π^0's, the statistical uncertainties are realised as presented in [Awe01b]. The calculation is based on the following argumentation:
Regarding the real event distribution, the measured number of photon pairs N is identified as the sum of the number of correlated photon pairs S and the number of uncorrelated γ-pairs B :

$$N = S + B. \tag{5.19}$$

The background can be estimated with the distribution of the mixed events as:

$$B' = k \cdot M \quad \text{with} \quad \overline{B'} = \overline{B}. \tag{5.20}$$

In Equation 5.20, M denotes the measured number of γ-pairs in the integration interval of the mixed-events distribution and k denotes the background scale factor as described in Section 5.4.2. The expected value $\langle B' \rangle$ is equal to the expectation of the background $\langle B \rangle$. Now the estimation of correlated pairs S' can be determined as:

$$S' = N - B' = N - kM \quad \text{with} \quad \overline{S'} = \overline{S}. \tag{5.21}$$

Therefore, the statistical uncertainty $\epsilon(S')$ of the estimated number of correlated pairs S' can be denoted as:

$$\epsilon^2(S') = \epsilon^2(N) + \epsilon^2(k)M^2 + k^2\epsilon^2(M) \tag{5.22}$$

$$= N + \epsilon^2(k)M^2 + k^2M \tag{5.23}$$

$$= S' + B' + \epsilon^2(k)M^2 + k^2M, \tag{5.24}$$

whereas the assumption is made that N and M underlay Poisson statistics. As $\epsilon^2(k)$, the fit uncertainty is used. Due to the steep falling spectra, the statistical uncertainty becomes larger for high p_{T} regions.

5.6.2 Systematic Uncertainties

During the analysis, several corrections and processes are applied to the raw data set which implicate systematic uncertainties due to finite accuracy. These sources

of systematic uncertainties have to be considered and are described in this section. The systematic uncertainties can be classified into three different categories:

- **Type A uncertainties**: These types of uncertainties are probably correlated in transverse momentum, but since the possible correlation is unknown, the uncertainties are treated as uncorrelated in p_{T}. Type A uncertainties are point-to-point uncertainties and basically belong to the category of statistical uncertainties.
- **Type B uncertainties**: These uncertainties reflect the systematic uncertainties which are correlated in p_{T} but allow the shape of the result to change.
- **Type C uncertainties**: Uncertainties of the type C are p_{T} correlated and move all data points in the same direction with the same value. The type C uncertainties are therefore normalisation uncertainties.

All systematic uncertainties are estimated as 1σ uncertainties. An overview of the systematic uncertainties for the different sector combination at three certain p_{T} values is presented in Table 5.6.

Peak Extraction

Systematic uncertainties occur due to the determination of the combinatorial background via a fit function. As mentioned in Section 5.4, the combinatorial background is parametrised with a Gaussian function together with a polynomial of second order in which the parameters of the polynomial are used to scale the background.
To estimate the systematic uncertainty, the mixed events distribution, i.e. the background, is parametrised with a different function, here with a linear function. Now the ratio of the linear function and the Gaussian function together with a polynomial of second order is calculated. This ratio leads to a p_{T}-dependent systematic uncertainty between 2% and 3%.

Acceptance

Another contribution to the systematic uncertainty is the correction of the acceptance. Although the geometry of the EMCal detectors is very well known, an uncertainty in the fastMC results from the parametrisation of the difference between the impact point of the photon on the detector surface and the position of the maximum

tower of a cluster [Rey03b]. In this analysis, this systematic uncertainty is estimated to 2.5%.

Efficiency

The reconstruction efficiency is another correction which is a source of a systematic uncertainty. To determine the value of this uncertainty, the photon identification cuts as well as the energy smearing of detectors have to be considered. The uncertainty due to the PID cuts is estimated by comparing the yield with all corrections applied for different PID categories. Additionally, the uncertainty because of energy and position smearing of the detector is determined via the change of the parameters for the energy smearing in the fastMC simulation (see Table 5.2). In conclusion, the two sources of systematic uncertainties are added in quadrature. The values lie between 6% and 10%, increased towards higher transverse momenta. Exemplary values for certain transverse momenta are shown in Table 5.6.

Trigger Normalisation Efficiency

Data from high-p_{T} triggered events has to be scaled for the combination. This normalisation correction can be determined in two different ways which are presented in [Rey03b] and [Aph03a]. The two methods provide a reasonable value for the scale down factor whereas both are estimated to lie within 1 σ. Therefore, a value of 5% is considered as a systematic uncertainty in the analysis.

Energy Scale

A main contribution to the systematic uncertainties is the determination of the absolute energy scale. The baseline for this uncertainty is the comparison of the π^0 peak positions of the invariant mass spectrum which can only be determined with a limited accuracy. As a consequence of this uncertainty, the yield for a given transverse momentum might as well represent the yield at a different transverse momentum shifted by the energy scale uncertainty.
Based on the tuning of the fastMC, the allowable energy shifts that can reproduce the peak positions vary by $\leq 2\%$. Therefore, the 1σ uncertainty in the energy scale is estimated to be 1.5% [Aph03a]. This uncertainty leads to an uncertainty in the π^0 yield which can be estimated by varying the energy scale in the fastMC by 1.5%. The systematic uncertainty can be determined by building the fractional difference

of the yields. However, a simple comparison of the spectrum described with the Equation 5.16 for different energy scales, p_{T} and $p'_{\mathrm{T}} = p_{\mathrm{T}} \cdot (1 \pm 0.02)$, provides the same result. The fractional difference is shown in Figure 5.13.

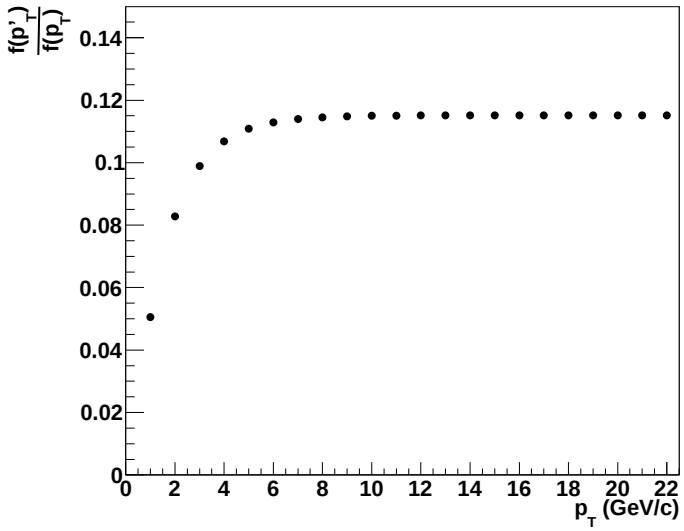

Figure 5.13: The histogram shows the discrete functional form of the systematic uncertainty due to the energy scaling.

Conversion

In this analysis the systematic uncertainty for the conversion correction is chosen to 2% (see Section 5.5.6).

Shower Merging

The correction of merging showers in the PHENIX EMCal is afflicted with an uncertainty because the characteristics of the merging cannot be simulated with full detail in the fastMC. Therefore, the uncertainty rises with increasing corrections towards higher transverse momenta. Based on the results for the merging correction f_{merg}, the systematic uncertainties $f_{\mathrm{sys}}(p_{\mathrm{T}})$ are estimated with Equation 5.25.

$$f_{\mathrm{sys}}(p_{\mathrm{T}}) = (1 - f_{\mathrm{merg}}(p_{\mathrm{T}}))^2 \tag{5.25}$$

Results for the systematic uncertainties are presented in Figure 5.14. Reasons for the difference of merging uncertainties between the PbSc and PbGl are found in the different position resolutions because of the different granularities.

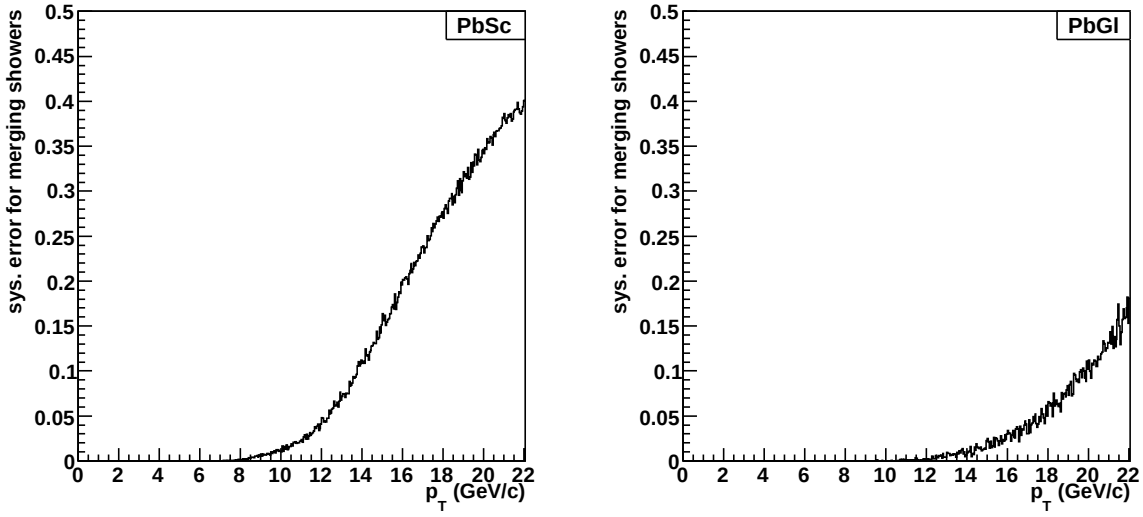

Figure 5.14: Estimation of the systematic uncertainty for the merging shower correction for the PbSc (left) and PbGl (right) calorimeter.

Centrality Bias Correction

The values which are used for the centrality bias correction also contain uncertainties. Therefore, the uncertainties presented in Table 5.5 are used for the systematic uncertainty determination of the nuclear modification factor.

p_{T}	3.25 (GeV/c)		9.75 (GeV/c)		17 (GeV/c)	
sys. uncertainty	PbGl	PbSc	PbGl	PbSc	PbGl	PbSc
peak extraction	2.4%	2.4%	2.1%	2.1%	2.1%	2.1%
acceptance	2.5%	2.5%	2.5%	2.5%	2.5%	2.5%
efficiency	6.5%	6.5%	8.5%	8.5%	9.0%	9.0%
energy scale	10.1%	10.1%	11.6%	11.6%	11.7%	11.7%
normalisation	5.0%	5.0%	5.0%	5.0%	5.0%	5.0%
conversion	2.0%	2.0%	2.0%	2.0%	2.0%	2.0%
shower merging	0.0%	0.0%	0.0%	1.0%	5.4%	26.0%
total sys	13.6%	13.6%	15.7%	15.8%	17.0%	30.6%
combined	9.6%		11.2%		15.2%	

Table 5.6: Overview of the systematic uncertainties of the π^0 analysis for three exemplary values of p_{T}. The calculation of the combined systematic error is based on the Equation 6.5 (under the assumption of no correlation). The centrality bias correction is not listed because it is first applied for the combined spectra.

6. Results of the π^0 Measurement

This chapter comprises the results of the π^0 measurement, i.e. the Lorentz-invariant yields for the two different calorimeters in different centrality classes. The results of the two detectors will be combined in a last step. All corrections and analysis steps described in the previous sections have been applied to the raw yields. The corrected yields are used to determine the nuclear modification factor $R_{d\mathrm{A}}$ which provides the opportunity to study initial state effects.
In addition, the results are compared to results from an earlier analysis in the same reaction system and centre-of-mass energy.

6.1 π^0 Invariant Yields

The invariant yield is presented as a combined spectrum of MinBias and ERT data. The choice for the transition from MinBias to ERT triggered events is based on the point where the ERT trigger reaches its geometrical limit (see Figure 5.11):

$$\frac{1}{2\pi p_{\mathrm{T}} N_{\mathrm{evt}}} \frac{\mathrm{d}^2 N}{\mathrm{d}p_{\mathrm{T}}\mathrm{d}y} = \begin{cases} \frac{1}{2\pi p_{\mathrm{T}} N_{\mathrm{evt}}} \frac{\mathrm{d}^2 N^{\mathrm{MinBias}}}{\mathrm{d}p_{\mathrm{T}}\mathrm{d}y} & p_{\mathrm{T}} < 7.5 \text{ GeV}/c, \\ \frac{1}{2\pi p_{\mathrm{T}} N_{\mathrm{evt}}} \frac{\mathrm{d}^2 N^{\mathrm{ERT}}}{\mathrm{d}p_{\mathrm{T}}\mathrm{d}y} & p_{\mathrm{T}} \geq 7.5 \text{ GeV}/c. \end{cases} \tag{6.1}$$

To demonstrate the consistency within the PbSc and PbGl, the spectra of both EMCal types for all five centrality selections are presented in Figure 6.1. A comparison of the different calorimeters is drawn via the ratio of the PbSc and the PbGl in Figure 6.2. The PbSc yield lies systematically below the yield of the PbGl. This behaviour is still subject to discussions and will be further investigated.

6.1.1 Combination of PbSc and PbGl

The spectra of the lead glass and the lead scintillator agree within the total uncertainties (Figure 6.2). Therefore, a combination of PbSc and PbGl is justified.

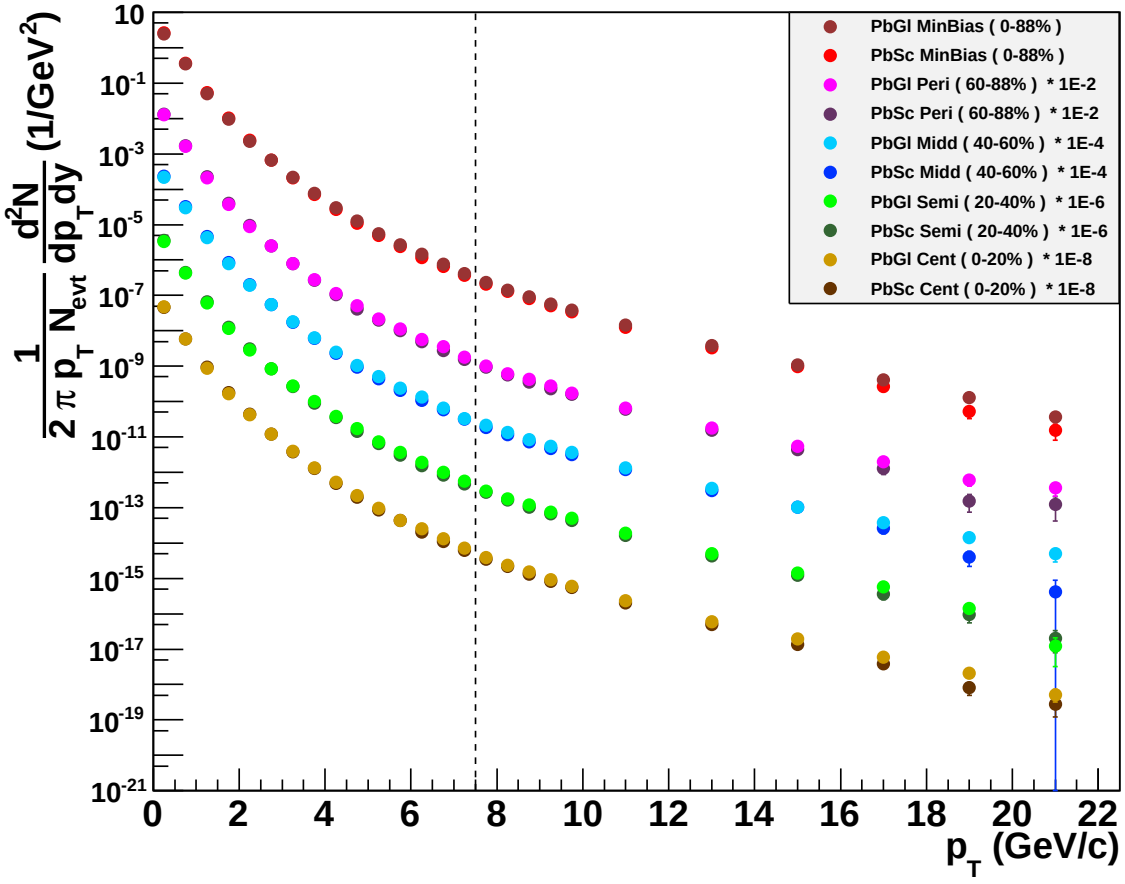

Figure 6.1: The Lorentz-invariant yield of neutral pions for the combination of MinBias and ERT data. The spectra are shown for all centrality classes with a PID 3 cut for the PbGl and the PbSc calorimeter. The dotted line depicts the transition from MinBias to ERT data. The error bars show the total uncertainties.

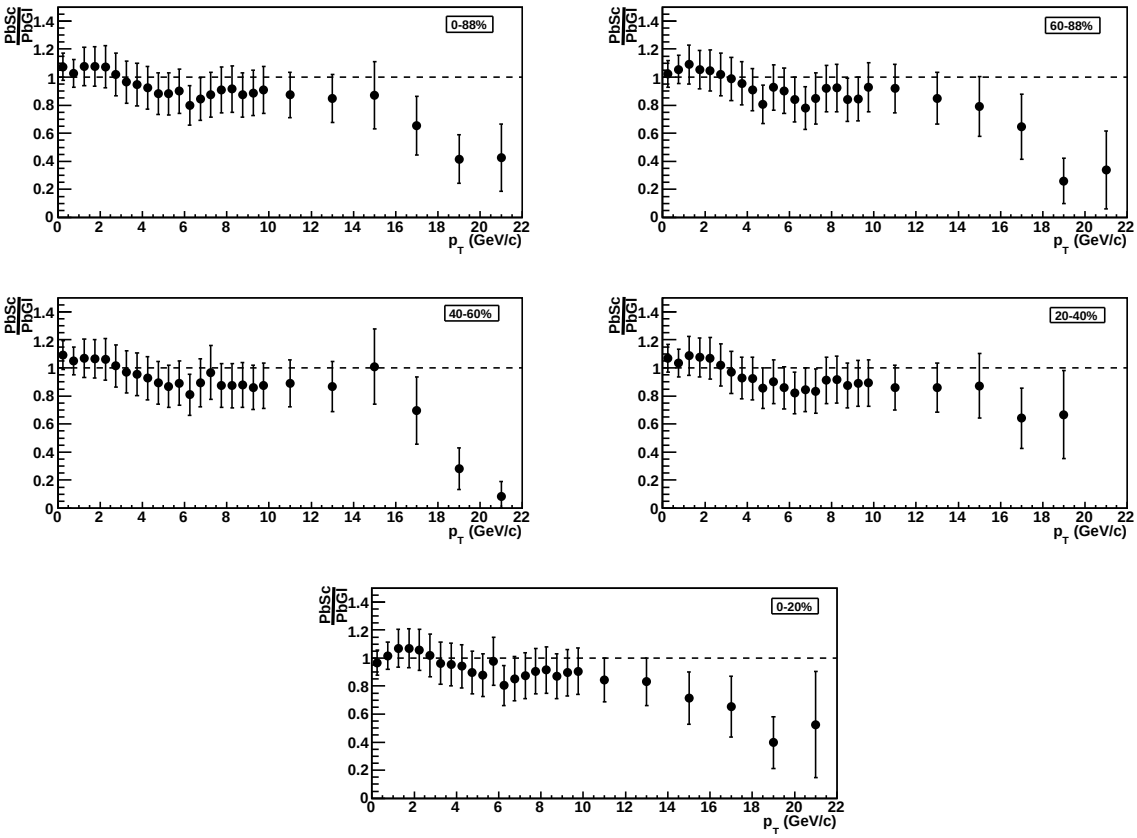

Figure 6.2: The ratio of the neutral pion spectra for PbGl and PbSc for each centrality class. The error bars represent the total uncertainties.

For the combination, the total uncertainties are used for weighting. The combined yield $\overline{x}(p_{\mathrm{T}})$ is calculated with the following equation:

$$\overline{x}(p_{\mathrm{T}}) = \frac{\sum_{\mathrm{i}=1}^{N} w_{\mathrm{i}}(p_{\mathrm{T}}) x_{\mathrm{i}}(p_{\mathrm{T}})}{\sum_{\mathrm{i}=1}^{N} w_{\mathrm{i}}(p_{\mathrm{T}})}, \quad \text{with} \quad w_{\mathrm{i}}(p_{\mathrm{T}}) = \frac{1}{\delta x_{\mathrm{i}}(p_{\mathrm{T}})^2}, \tag{6.2}$$

where $x_{\mathrm{i}}(p_{\mathrm{T}})$ and $\delta x_{\mathrm{i}}(p_{\mathrm{T}})$ indicate the yield and the total uncertainty of the yield for a certain p_{T} value, respectively, of PbGl (i = 1) and PbSc (i = 2) with $N = 2$. To obtain the total uncertainty $\delta\overline{x}^{\mathrm{tot}}$ of the combined yield, the quadratic sum of the statistical and systematic uncertainties is calculated:

$$\delta\overline{x}^{\mathrm{tot}}(p_{\mathrm{T}})^2 = \delta\overline{x}^{\mathrm{stat}}(p_{\mathrm{T}})^2 + \delta\overline{x}^{\mathrm{sys}}(p_{\mathrm{T}})^2, \tag{6.3}$$

with

$$\delta\overline{x}^{\mathrm{stat}}(p_{\mathrm{T}})^2 = \sum_{\mathrm{i}=1}^{N} \frac{1}{N} \frac{w_{\mathrm{i}}}{\sum_{\mathrm{j}=1}^{N} w_{\mathrm{j}}(p_{\mathrm{T}})} \cdot \delta x_{\mathrm{i}}^{\mathrm{stat}}(p_{\mathrm{T}})^2, \tag{6.4}$$

$$\delta\overline{x}^{\mathrm{sys}}(p_{\mathrm{T}})^2 = \sum_{\mathrm{i}=1}^{N} \frac{1}{N} \frac{w_{\mathrm{i}}}{\sum_{\mathrm{j}=1}^{N} w_{\mathrm{j}}(p_{\mathrm{T}})} \cdot \delta x_{\mathrm{i}}^{\mathrm{sys}}(p_{\mathrm{T}})^2. \tag{6.5}$$

Figure 6.3 shows the π^0 invariant yield for the combination of both EMCal types. All centrality classes are illustrated for the PID 3 cut. Results have been obtained up to a transverse momentum of $p_{\mathrm{T}} = 22$ GeV/c.

6.1.2 Nuclear Modification Factor

For studying initial state effects in d+Au collisions, the nuclear modification factor $R_{d\mathrm{A}}$ is determined from the invariant yield of the π^0's. Moreover, the calculation is performed with respect to the centrality of the collisions because initial state effects are expected to depend on the centrality.
To calculate $R_{d\mathrm{A}}$ for a centrality f, the yield of π^0's in d+Au collisions $\mathrm{d}^2N_{d\mathrm{A}}^{\pi^0}/\mathrm{d}p_{\mathrm{T}}\mathrm{d}y$ has to be divided by the yield of π^0's in p+p collisions $\mathrm{d}^2N_{pp}^{\pi^0}/\mathrm{d}p_{\mathrm{T}}\mathrm{d}y$ and normalised to the average of the number of binary collisions N_{coll}:

$$R_{\mathrm{dA}} = \frac{\mathrm{d}^2N_{\mathrm{dA}}^{\pi^0}/\mathrm{d}p_{\mathrm{T}}\mathrm{d}y}{\mathrm{d}^2N_{pp}^{\pi^0}/\mathrm{d}p_{\mathrm{T}}\mathrm{d}y \cdot \langle N_{\mathrm{coll}} \rangle_f}. \tag{6.6}$$

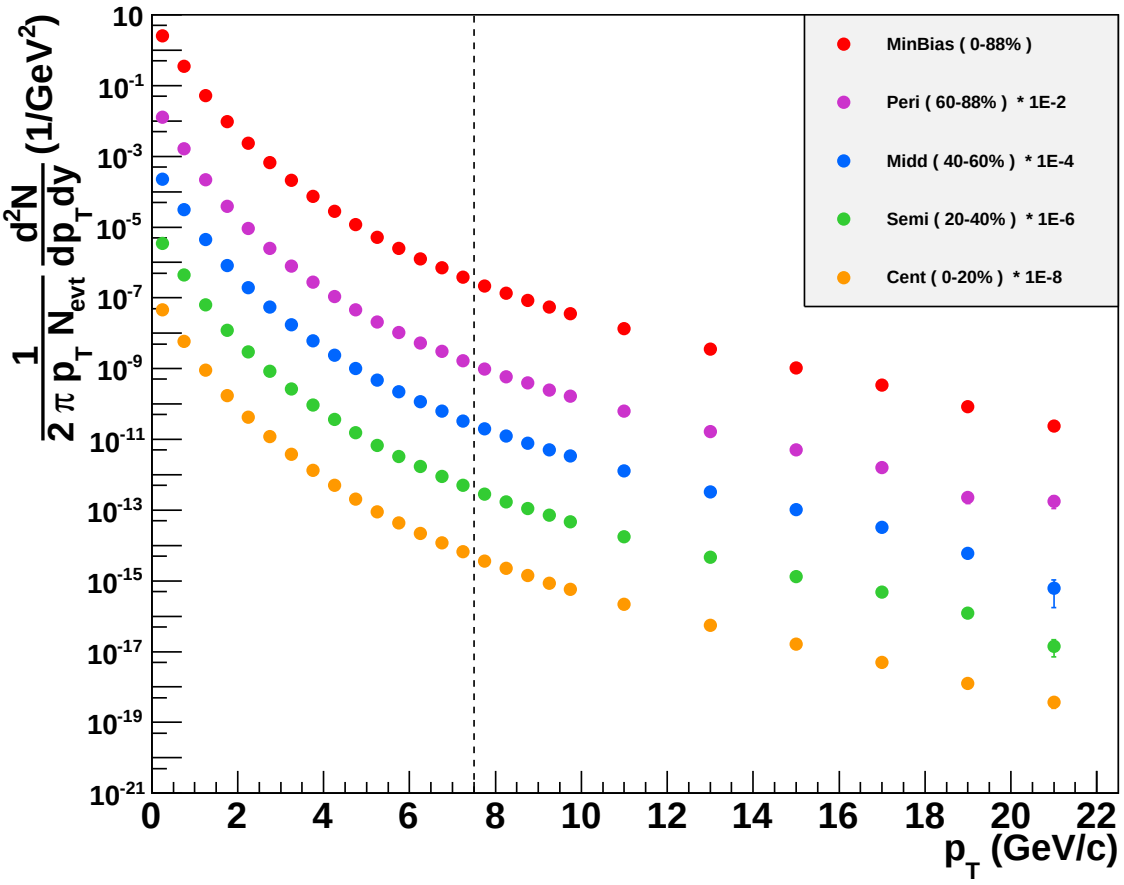

Figure 6.3: The Lorentz-invariant yields of neutral pions for the combination of MinBias and ERT data. The spectra are shown for all centrality classes with a PID 3 cut. The dotted line depicts the transition from MinBias to ERT data. The error bars show the total uncertainties.

centrality class	N_{coll}
0-20%	15.37 ± 1.0
20-40%	10.63 ± 0.7
40-60%	6.95 ± 0.6
60-88%	3.07 ± 0.3
0-88%	8.42 ± 0.3

Table 6.1: Overview of the values for the number of binary collision [Zha04].

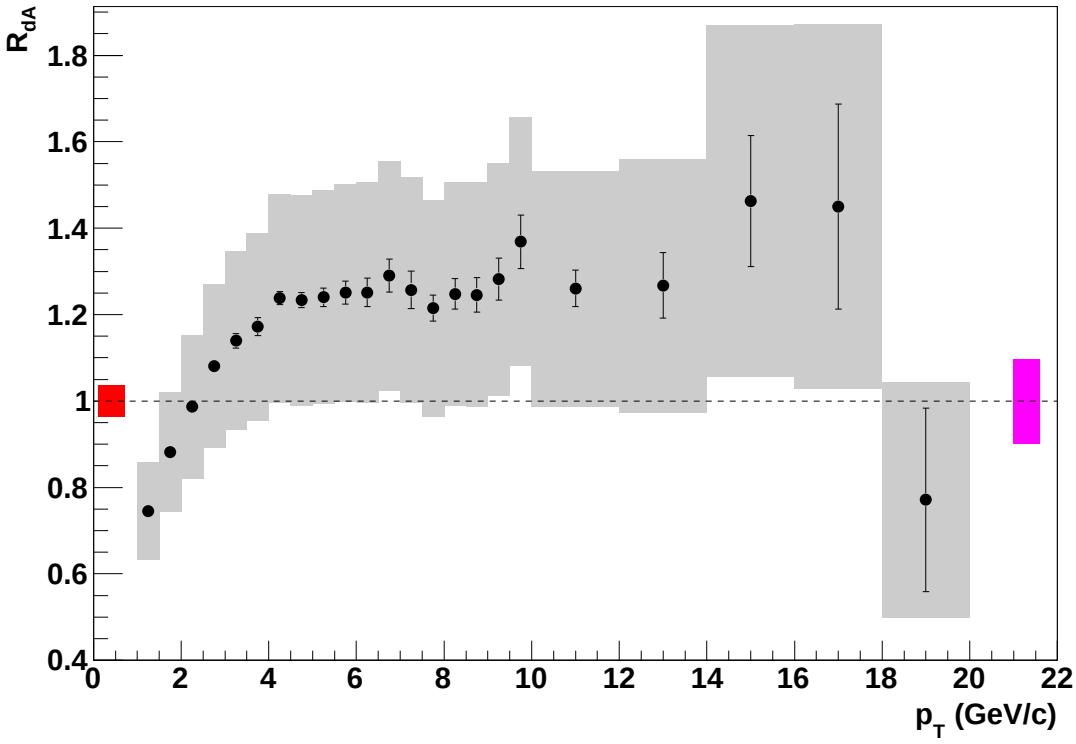

Figure 6.4: The nuclear modification factor for π^0 in d+Au collisions for $\sqrt{s_{\mathrm{NN}}} = 200$ GeV for MinBias events (00-88%). The systematic uncertainties are presented as grey boxes. The black vertical lines show the statistical uncertainties. The red box on the left reflects the systematic uncertainty of N_{coll} and the magenta box on the right reflects the normalisation uncertainty of σ_{pp} which is 9.7%.

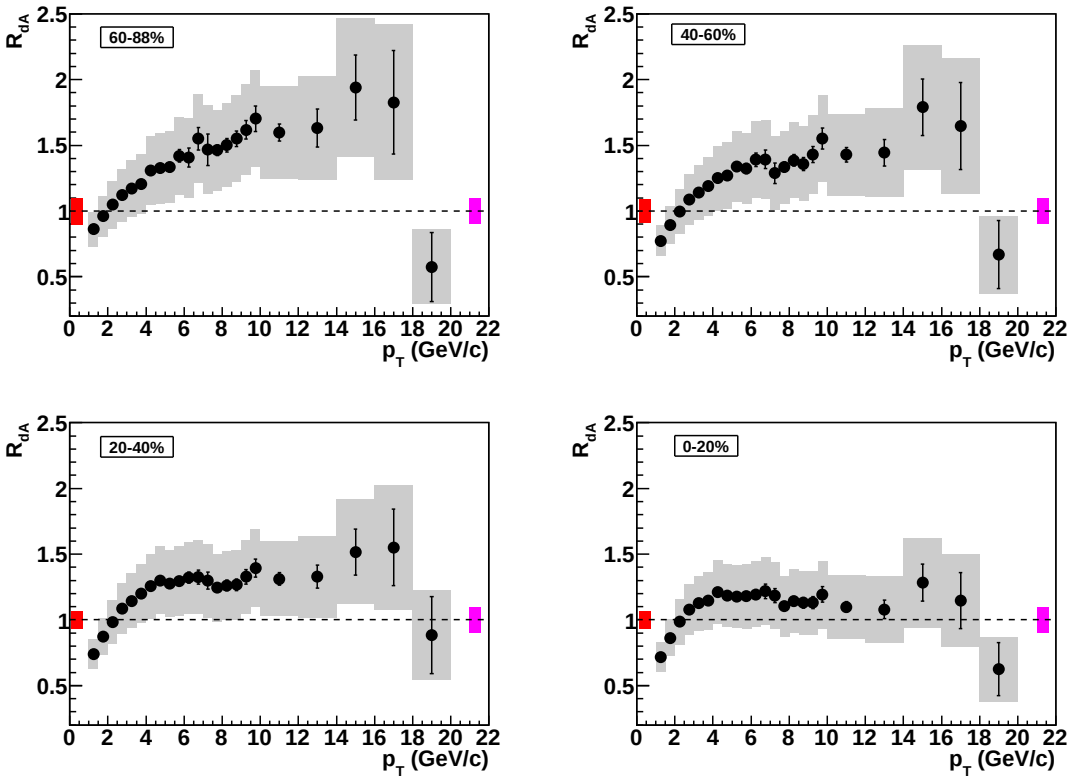

Figure 6.5: The nuclear modification factor for π^0 in d+Au collisions for $\sqrt{s_{\mathrm{NN}}} = 200$ GeV for the four centrality classes. The systematic uncertainties are presented as grey boxes. The black vertical lines show the statistical uncertainties. The red box on the left reflects the systematic uncertainty of N_{coll} and the magenta box on the right reflects the normalisation uncertainty of σ_{pp} which is 9.7%.

As baseline the p+p cross section of Run 5 is used [Ada07]. Furthermore, the values for N_{coll} are determined from Glauber simulations [Zha04]. A list of the values for the number of binary collisions is shown in Table 6.1.

Important information that can be extracted from the nuclear modification factor for MinBias events, shown in Figure 6.4, is the absence of a suppression of neutral pions with high transverse momentum. In addition, a Cronin-like enhancement is visible in the distribution of $R_{d\mathrm{A}}$. Values for the nuclear modification factor are determined up to a transverse momentum of $p_{\mathrm{T}} = 19$ GeV/c. This limit is due to the information on p+p collision data. The nuclear modification factor with respect to the centrality of the collision is given in Figure 6.5. Here, a dependence of the form of $R_{d\mathrm{A}}$ on the different centralities can be observed.

Systematic uncertainties in $R_{d\mathrm{A}}$

The systematic uncertainties for the nuclear modification factor are presented in Figures 6.4 and 6.5 as grey boxes. Due to the comparison to p+p collisions from another run and therefore a different analysis with a different setup of the EMCal and resulting different corrections, none of the systematic uncertainties are assumed to cancel. Thus all mentioned systematic uncertainties described in Section 5.6.2 must be taken into account. A general approach in the context of the uncertainty calculation is the separate presentation of the systematic uncertainties of the centrality bias correction and the normalisation uncertainty of the p+p cross section σ_{pp} instead of combining them into the whole systematic uncertainty of the measurement. These values are presented as the red box on the left side for the centrality bias uncertainty and as the magenta box on the right side for the normalisation uncertainty in the corresponding figures.

Ratio of Central and Peripheral R_{cp}

To verify the characteristics of initial state effects depending on the centrality of the d+Au collisions, another type of nuclear modification factor in form of the ratios of central and peripheral events, R_{cp}, is calculated:

$$R_{\mathrm{cp}} = \frac{R_{d\mathrm{A}}^{\mathrm{central}}}{R_{d\mathrm{A}}^{\mathrm{peripheral}}} = \frac{\mathrm{d}^2 N_{\mathrm{dA}}^{\pi^0}/\mathrm{d}p_{\mathrm{T}}\mathrm{d}y|_{\mathrm{central}}}{\langle N_{\mathrm{coll}}\rangle^{\mathrm{central}}} \cdot \frac{\langle N_{\mathrm{coll}}\rangle^{\mathrm{peripheral}}}{\mathrm{d}^2 N_{\mathrm{dA}}^{\pi^0}/\mathrm{d}p_{\mathrm{T}}\mathrm{d}y|_{\mathrm{peripheral}}}. \tag{6.7}$$

Figure 6.6 includes the results for R_{cp}. An advantage of this procedure is that the systematic uncertainties cancel and only the statistical uncertainties are considered.

By means of the size of the uncertainties, the transition from MinBias to ERT events can be observed.

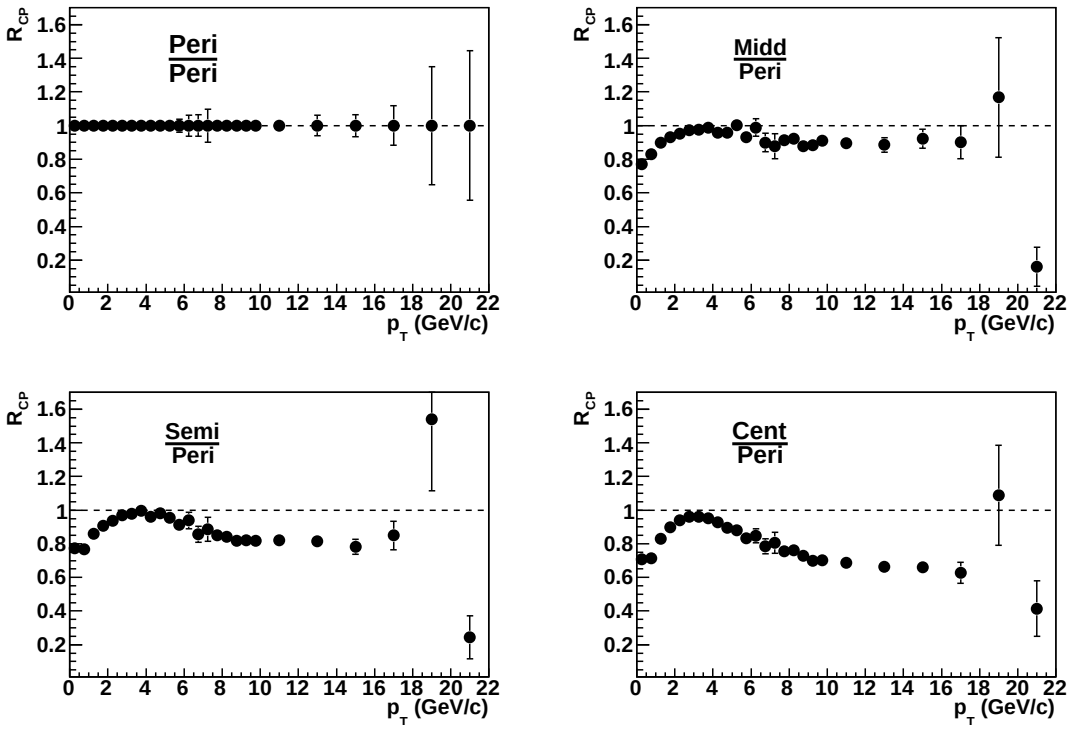

Figure 6.6: Ratio of central and peripheral events of d+Au collision at $\sqrt{s_{\mathrm{NN}}} = 200$ GeV, normalised to the average number of binary collisions $\langle N_{\mathrm{coll}} \rangle$ (see Equation 6.7). The error bars represent the statistical uncertainties.

6.2 Comparison with Previous Results

During Run 3 in 2002 and 2003 another measurement of d+Au collisions at $\sqrt{s_{\mathrm{NN}}} = 200$ GeV was performed. This former data set was analysed and the invariant yield of π^0's was determined [Adl07].

A comparison of the invariant yields of the analysis of Run 8 data and the former Run 3 data is provided in Figures 6.7 and 6.8. The current analysis offers information over a larger p_{T} region whereby a disagreement of the data points can be recognised in all centrality classes. Both data sets reveal a difference between the invariant yields. This difference is tending upwards towards higher transverse

momenta of the π^0's.

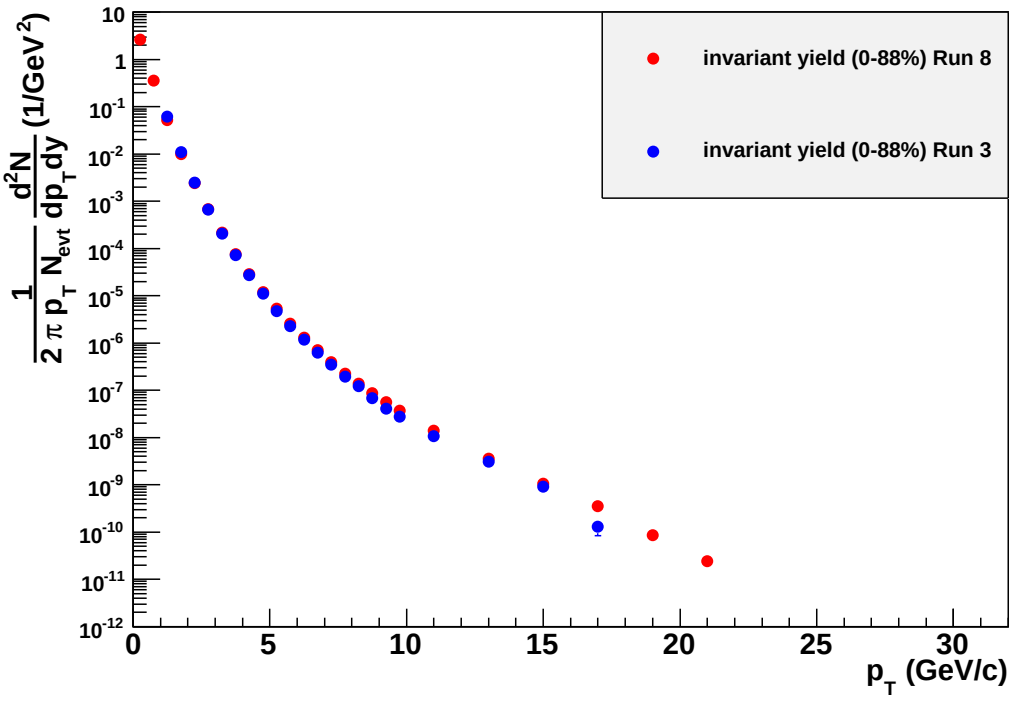

Figure 6.7: Comparison of the π^0 invariant yields for MinBias data of the results of Run 3 [Adl07] and the obtained yield in this thesis.

Moreover, the nuclear modification factors are compared with each other which is shown in the Figures 6.9. and 6.10.

The comparison exposes a surprising difference between the calculated results of the yield as well as the nuclear modification factor. Although the systematic uncertainties of the d+Au measurement in Run 8 are very large, a difference is still obvious for all centrality classes. In the distribution of the $R_{d\mathrm{A}}$, one observes a systematic enhancement of the results for the data of Run 8 compared to the analysis of Run 3. Upon submission of this thesis, the difference was still subject to discussions and will be further investigated.

An additional comparison is drawn with results of charged hadrons in deuteron-gold collisions at the same centre-of-mass energy. The analysis of those measurements exhibits a calculation of $R_{d\mathrm{A}}$ which is also enhanced compared to the results for neutral pions from Run 3. Moreover, it is expected that no difference will occur

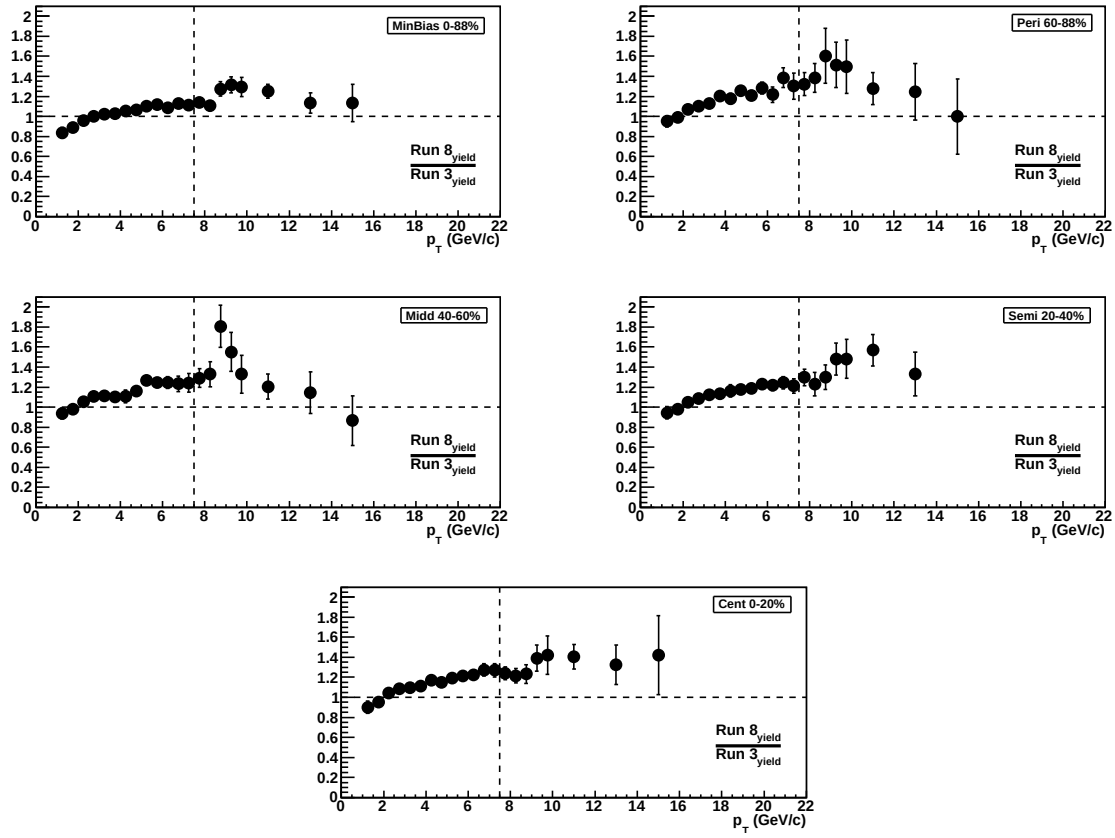

Figure 6.8: Ratio of the π^0 invariant yields for centrality dependent data of the results of Run 3 [Adl07] and the yields obtained in this thesis. The vertical dotted line marks the transition point from MinBias data to ERT data.

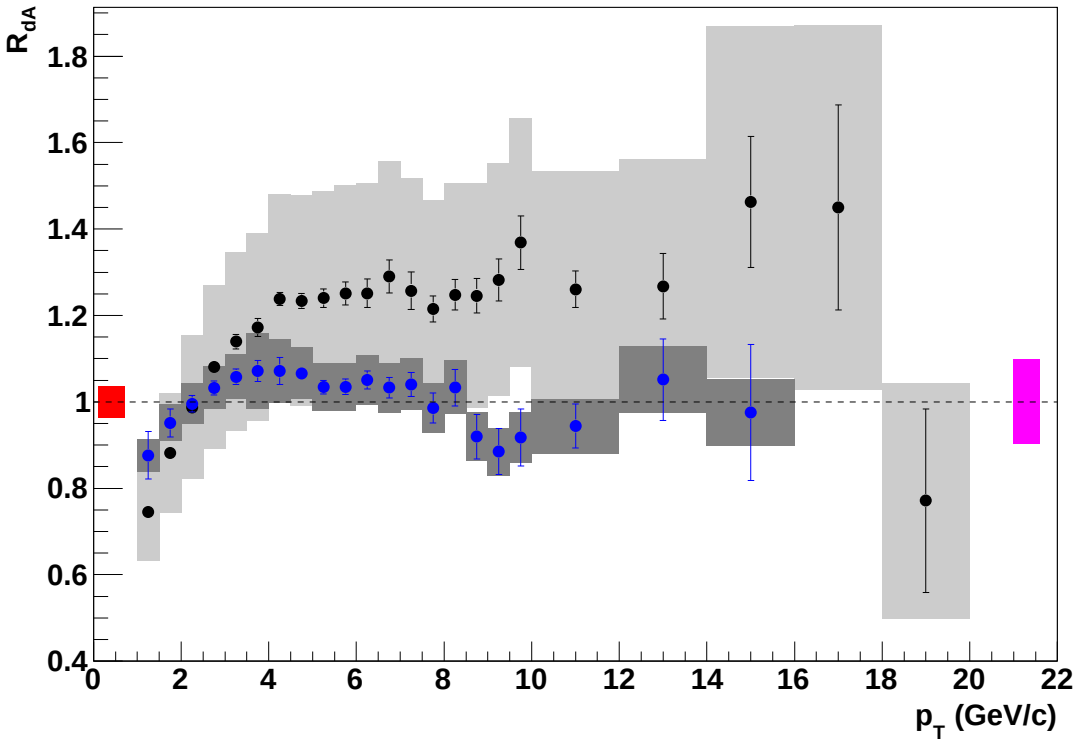

Figure 6.9: Comparison of the results for the nuclear modification factor of this thesis (black) and Run 3 (blue) [Adl07] for MinBias data. The results of Run 3 are depicted with the statistical uncertainties (blue vertical lines) as well as systematic uncertainties (dark grey boxes).

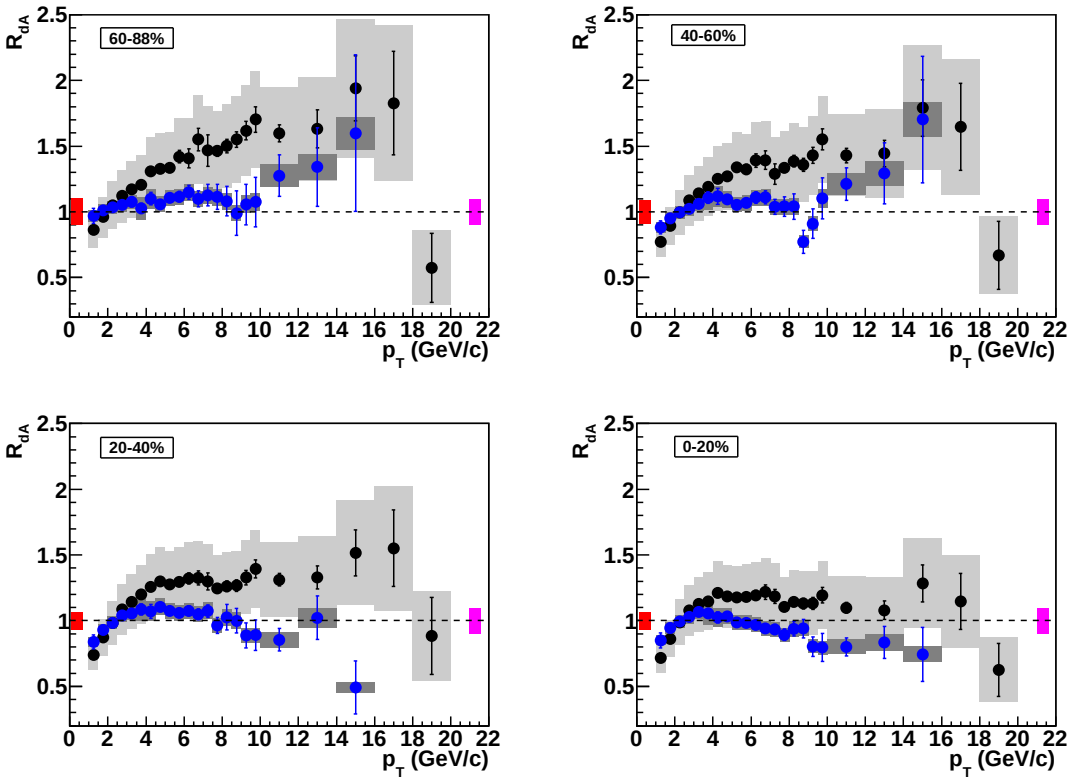

Figure 6.10: Comparison of the results for the nuclear modification factor of this thesis (black) and Run 3 (blue) [Adl07] for data of different centrality classes. The results of Run 3 are depicted with the statistical uncertainties (blue vertical lines) as well as systematic uncertainties (dark grey boxes).

between charged hadrons and neutral pions towards higher p_T because the charged hadrons would only consist of π^+ and π^-. In this context, data of charged hadrons for MinBias [Adl03b] and for the individual centrality classes [Adl08] is compared to the results of π^0's from this thesis.

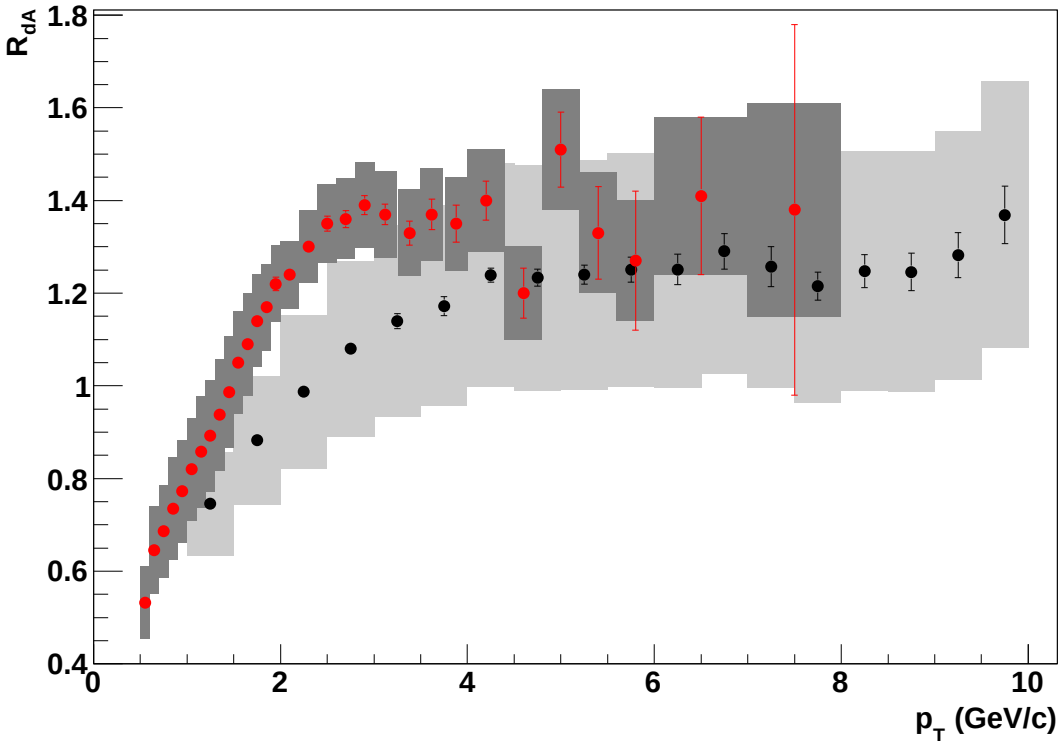

Figure 6.11: Nuclear modification factors for charged hadrons [Adl03b] and π^0's from this thesis for MinBias events. The red points mark the distribution of charged hadrons and the black dots indicate the results of neutral pions. Additionally, the statistical uncertainties are presented as vertical lines and the systematic uncertainties are represented as grey boxes. In this figure, no normalisation uncertainties are considered.

In the case of the R_{dA} distribution for the charged hadrons, a steeper increase is noticed. Towards higher p_T, 4 GeV/c < p_T < 8 GeV/c, an agreement of minimum bias data is observed. The comparisons of the different centralities show the same trend but another behaviour at p_T = 6.5 GeV/c of the charged hadron distribution (see Figure 6.12) which is displayed in a decrease of the nuclear modification factor.

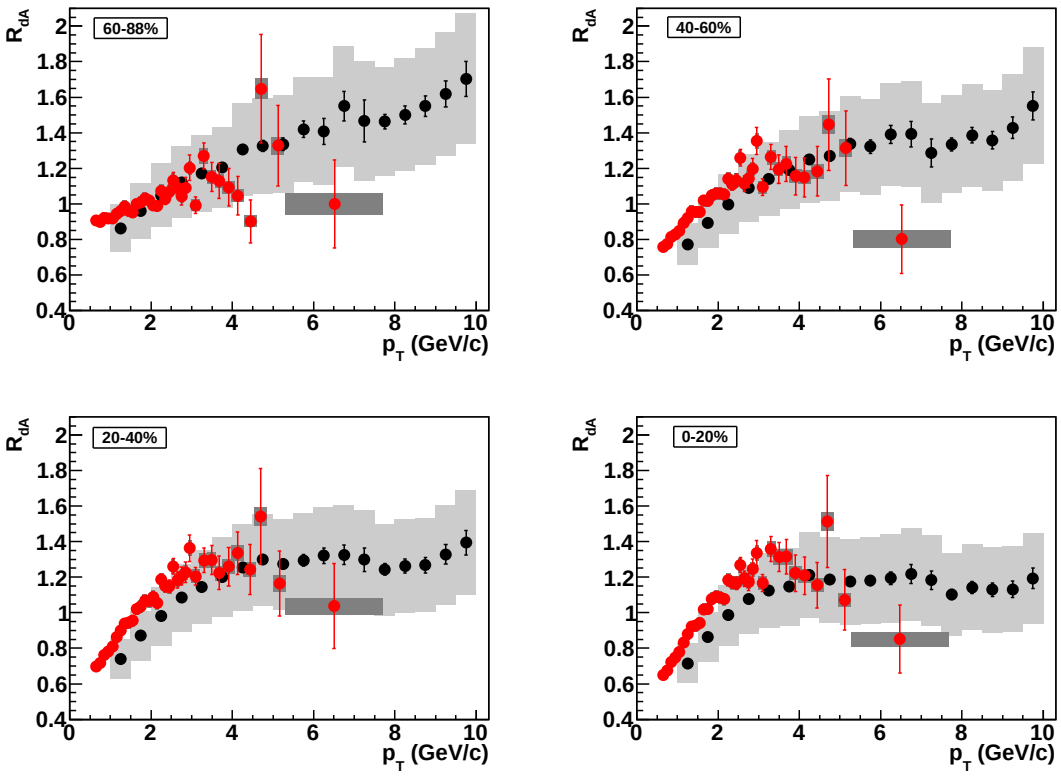

Figure 6.12: Centrality dependent nuclear modification factors for charged hadrons [Adl07] and π^0's from this thesis for the individual centrality classes. The red points mark the distribution of charged hadrons and the black dots indicate the results of neutral pions. Additionally, the statistical uncertainties are presented as vertical lines and the systematic uncertainties are presented as grey boxes. In this figure no normalisation uncertainties are considered.

6.3 Conclusion

In this thesis, the Lorentz-invariant yields of π^0's have been determined and the nuclear modification factors have been calculated. The nuclear modification factors of π^0's can be used to study possible initial state effects in the reaction of d+Au collisions and can be compared to other experimental results and theories.
In the light of the nuclear modification factor, no suppression of particle production can be observed which is consistent with the theoretical expectation that no QGP is created.
In addition, the fact that no high-p_{T} particle suppression can be recognised, no evidence of the occurrence of a colour-glass condensate can be found which indicates jet-quenching as a final state effect in central Au+Au collisions. Nevertheless, the nuclear modification factor is not consistent with unity and is increased towards higher transverse momenta which is displayed in Figure 6.5. Moreover, a flat distribution of $R_{d\mathrm{A}}$ in central collisions towards higher p_{T} is observed in Figure 6.5. The nuclear modification factor of d+Au collisions has already been studied [Adl07]. A comparison with this former analysis shows a difference in the results of the nuclear modification factor. The results obtained in this analysis lie above those from Run 3. However, both results show the same trend in the nuclear modification factor in peripheral and more central events. This characteristic, i.e. the similar development of the nuclear modification factor, can be observed in Figure 6.10.
Another comparison is drawn with the nuclear modification factor of charged hadrons. The Figures 6.11 and 6.12 display the comparison of the nuclear modification factors of charged hadrons and neutral pions. An agreement in the trend of the nuclear modification factor for charged hadrons and neutral pions can be noticed. Nevertheless, the results of the charged hadrons do not reach far enough in p_{T} to allow clear statements.

7. Summary

In this thesis, the production of π^0's in deuteron-gold collisions with a centre-of-mass energy $\sqrt{s_{\mathrm{NN}}} = 200$ GeV has been analysed. The measurement is performed with the electromagnetic calorimeter of the PHENIX experiment at the RHIC collider at BNL. The invariant yields of π^0's are determined and used to calculate the nuclear modification factor.

The neutral pions are reconstructed via their two-photon decay and the measurement of the decay photons with the EMCal. An invariant mass analysis is used to extract the π^0's. The results of the EMCal measurement are obtained with two different trigger conditions to cover π^0's with low transverse momenta as well as high-p_{T} π^0's. All necessary corrections and analysis steps to determine the Lorentz-invariant yields and to combine the two data sets have been applied and are described in this thesis. In addition, the data set is subdivided into different centrality classes. The data is analysed with the PbGl and the PbSc independently. After applying all corrections, the Lorentz-invariant yields for the π^0 have been determined for transverse momenta up to $p_{\mathrm{T}} = 22$ GeV/c. The result is used to calculate the nuclear modification factor $R_{d\mathrm{A}}$ which is the ratio of the yields of d+Au and $p+p$ collisions scaled by the number of binary nucleon-nucleon collisions. The nuclear modification factor offers an insight into the nuclear structure function and provides information on initial state effects. The study of these effects is important, particularly regarding the energy loss of hard scattered partons in a hot and dense medium, the quark-gluon plasma (QGP). In d+Au collisions, the formation of a QGP is not expected and therefore this system offers a qualified baseline for Au+Au collisions where a suppression of neutral pions has been observed [Adc02, Adl03c].
In this analysis, no suppression of the π^0's could be noticed. Compared to a former analysis of the same reaction system, the results are different which in particular is displayed in an increase of $R_{d\mathrm{A}}$. Nevertheless, the comparison of the trend of the nuclear modification factor of Run 3 and Run 8 shows the same shape in peripheral as well as in central collisions.

The possibility of a suppression of π^0 production due to a formation of a

Colour Glass Condensate (CGC) could not be approved by the results and can therefore not explain a suppression of neutral pion production in central Au+Au collisions.

The results outlined in this thesis show new results which are not consistent with a former analysis of neutral pions (Run 3). An enhancement in the invariant yields and therefore in the nuclear modification factor is noticed. Another interesting aspect is the comparison to the nuclear modification factor of charged hadrons for the same collision system. The results for minimum bias data especially show a good agreement. Nevertheless, the results for charged hadrons have a much smaller reach, reaching only up to $p_{\mathrm{T}} = 8$ GeV/c.
Possible explanations for deviations in the results can be found in the inaccurate energy calibration which can be observed in the π^0 peak positions of the data and the simulations. Thus, further analysis with an aligned energy scaling could improve the results in the future.

A. Kinematic Variables

To study heavy ion reactions it is useful to choose kinematic variables which can be simply transformed when changing the reference frame. A particle is characterised by its *four momentum*[1] P according to special relativity. In contravariant form the four momentum is denoted as:

$$P^{\mu} = (E, \vec{p}) = (E, \vec{p}_{\mathrm{T}}, p_z) = (E, p_x, P_y, p_z), \tag{A.1}$$

where E denotes the energy of the particle. For a free particle the relativistic energy-momentum-relation is determined as:

$$E^2 = m^2 + p^2, \tag{A.2}$$

with m identifying the rest mass of a particle.
For the description of a collision between a particle A and B, the *Mandelstam variable* s is used which contains the sum of the individual four momenta:

$$s = (P_{\mathrm{A}} + P_{\mathrm{B}})^2, \tag{A.3}$$

$\sqrt{s}$ denotes the centre-of-mass energy in the reaction system of the two nuclei.
The beam is considered to point in the direction of the z-axis of the coordinate system. The particle runs into the beam direction under the angle ϑ and can be subdivided into a longitudinal component p_{L} and a transversal component p_{T}:

$$p_{\mathrm{L}} = \; p \cdot \cos\vartheta = p_z, \tag{A.4}$$

$$p_{\mathrm{T}} = \; p \cdot \sin\vartheta = \sqrt{p_x^2 + p_y^2}, \tag{A.5}$$

with $p = |\vec{p}|$ the norm of the momentum.

The longitudinal velocity β_{L} of a particle can be described via the rapidity y:

$$y = \operatorname{arctanh} \beta_{\mathrm{L}}, \tag{A.6}$$

$$= \frac{1}{2} \ln \frac{E + p_{\mathrm{L}}}{E - p_{\mathrm{L}}}. \tag{A.7}$$

[1] Here and in the following the convention $c = \hbar = 1$ is used.

The rapidity depends on the reference system. The advantage compared to the longitudinal velocity β_{L} is the additive behaviour of the rapidity under a change of the reference frame which moves with a velocity β relative to the old reference frame in the longitudinal direction:

$$y' = y + \operatorname{arctanh}\,\beta. \tag{A.8}$$

For this reason the shape of the rapidity distribution of a variable is independent of the choice of the reference frame. The connection between the energy and rapidity is built via the transverse mass which is defined as:

$$m_{\mathrm{T}} = \sqrt{p_{\mathrm{T}}^2 + m^2}. \tag{A.9}$$

The connection of the energy and momentum to the rapidity is denoted as:

$$E = m_{\mathrm{T}} \cdot \cosh y, \tag{A.10}$$

$$p_{\mathrm{L}} = m_{\mathrm{T}} \cdot \sinh y. \tag{A.11}$$

In the limit case $E \gg m$, the rapidity can be approximated by the *pseudo-rapidity* η:

$$\eta = \frac{1}{2} \ln \frac{p + p_{\mathrm{L}}}{p - p_{\mathrm{L}}}, \tag{A.12}$$

$$= -\ln \left[\tan \left(\frac{\vartheta}{2} \right) \right]. \tag{A.13}$$

The pseudo-rapidity can be determined using the angle ϑ of the flight direction of a particle with respect to the beam direction. For this reason, the pseudo-rapidity offers the opportunity to measure the rapidity in an easy experimental way. Regarding the Equations A.12 and A.13, the energy and momentum can be expressed in terms of η:

$$E = p_{\mathrm{T}} \cdot \cosh \eta, \tag{A.14}$$

$$p_{\mathrm{L}} = p_{\mathrm{T}} \cdot \sinh \eta. \tag{A.15}$$

B. Lorentz-Invariant Cross Section

In high energy reactions, the production of particles is described with a Lorentz-invariant value, the cross section $E\frac{\mathrm{d}^3\sigma}{\mathrm{d}\vec{p}^{\,3}}$:

$$E\frac{\mathrm{d}^3\sigma}{\mathrm{d}\vec{p}^{\,3}} = E\frac{1}{p_\mathrm{T}}\frac{\mathrm{d}^3\sigma}{\mathrm{d}p_\mathrm{T}\mathrm{d}\varphi\mathrm{d}p_\mathrm{L}}. \tag{B.1}$$

Using the Equations A.10 and A.11, it follows $E = \mathrm{d}p_\mathrm{L}/y$. Inserted in B.1 one obtains:

$$E\frac{\mathrm{d}^3\sigma}{\mathrm{d}\vec{p}^{\,3}} = \frac{1}{p_\mathrm{T}}\frac{\mathrm{d}^3\sigma}{\mathrm{d}p_\mathrm{T}\mathrm{d}\varphi\mathrm{d}y}. \tag{B.2}$$

Under the consideration of the φ-symmetry, the integration over this variable can be determined as follows:

$$E\frac{\mathrm{d}^3\sigma}{\mathrm{d}\vec{p}^{\,3}} = \frac{1}{2\pi p_\mathrm{T}}\frac{\mathrm{d}^2\sigma}{\mathrm{d}p_\mathrm{T}\mathrm{d}y}. \tag{B.3}$$

Regarding the production of a certain particle species X in an inelastic collision, the integral over the associated Lorentz-invariant cross section results in the product of the average number of produced particles per collision $\langle N\rangle$ and the total inelastic cross section σ_inel:

$$\int E\frac{\mathrm{d}^3\sigma}{\mathrm{d}\vec{p}^{\,3}} = \int p_\mathrm{T}\mathrm{d}p_\mathrm{T}\mathrm{d}y\mathrm{d}\varphi E\frac{\mathrm{d}^3\sigma}{\mathrm{d}\vec{p}^{\,3}} = \langle N\rangle\cdot\sigma_\mathrm{inel}. \tag{B.4}$$

In this analysis the particle production normalised to the number of events N_evt of inelastic collisions is determined:

$$E\frac{\mathrm{d}^3N}{\mathrm{d}\vec{p}^{\,3}} = \frac{1}{2\pi p_\mathrm{T}N_\mathrm{evt}}\frac{\mathrm{d}^2N}{\mathrm{d}p_\mathrm{T}\mathrm{d}y}. \tag{B.5}$$

The value $E\frac{\mathrm{d}^3N}{\mathrm{d}\vec{p}^{\,3}}$ is denoted as the *invariant yield* or *invariant multiplicity* of a reaction. In experiments it is a common method to measure the invariant yield instead of the invariant cross section. These two quantities are connected via the total inelastic cross section, given in the following equation:

$$E\frac{\mathrm{d}^3\sigma}{\mathrm{d}\vec{p}^{\,3}} = E\frac{\mathrm{d}^3N}{\mathrm{d}\vec{p}^{\,3}}\cdot\sigma_\mathrm{inel}. \tag{B.6}$$

C. List of Analysed Runs

246444	246445	246451	246453	246457	246459	246466	246468	246469	246472
246474	246476	246479	246480	246483	246484	246485	246486	246487	246488
246490	246492	246496	246497	246498	246499	246500	246501	246502	246503
246510	246511	246512	246516	246542	246543	246546	246547	246548	246550
246551	246581	246583	246584	246585	246587	246594	246595	246597	246599
246600	246603	246605	246606	246610	246612	247037	247041	247044	247045
247054	247055	247169	247172	247173	247174	247176	247177	247179	247180
247182	247183	247184	247185	247186	247189	247190	247191	247229	247230
247231	247232	247234	247235	247236	247237	247238	247239	247240	247241
247242	247243	247244	247246	247247	247248	247249	247250	247251	247253
247254	247255	247256	247377	247378	247379	247381	247382	247385	247387
247388	247389	247391	247392	247397	247399	247400	247401	247402	247403
247404	247411	247413	247414	247416	247417	247418	247421	247426	247428
247429	247433	247434	247435	247436	247437	247438	247439	247440	247483
247484	247609	247616	247621	247622	247623	247624	247625	247626	247631
247782	247784	247786	247787	247788	247789	247815	247816	247817	247818
247820	247821	247935	247936	247938	247939	247940	247941	247942	247947
247948	247950	247952	247959	248033	248037	248039	248040	248045	248050
248051	248052	248054	248150	248170	248171	248173	248174	248175	248177
248178	248184	248287	248288	248289	248291	248293	248295	248298	248302
248304	248308	248309	248310	248311	248353	248355	248359	248363	248364
248365	248367	248368	248380	248382	248383	248473	248475	248476	248478
248479	248490	248526	248527	248528	248534	248535	248666	248667	248671
248781	248782	248784	248787	248788	248789	248790	248865	248871	248886
248887	249047	249048	249052	249065	249069	249070	249071	249072	249085

Table C.1: List of analysed d+Au runs at $\sqrt{s_{\mathrm{NN}}} = 200$ GeV.

249086	249090	249092	249093	249094	249111	249114	249115	249117	249123
249124	249127	249128	249129	249130	249131	249132	249135	249138	249146
249147	249148	249230	249231	249259	249391	249393	249394	249398	249399
249401	249403	249405	249433	249437	249440	249441	249452	249453	249454
249456	249458	249460	249463	249464	249466	249467	249469	249471	249473
249474	249485	249487	249488	249491	249495	249497	249499	249716	249720
249727	249728	249731	249738	249742	249746	249747	249748	249750	249751
249764	249768	249769	249771	249772	249837	249838	249839	249843	249844
249846	249847	249853	249854	249858	249865	249866	249867	249868	249869
250002	250003	250005	250006	250008	250010	250014	250016	250019	250020
250022	250024	250025	250026	250041	250042	250044	250045	250046	250047
250048	250095	250097	250101	250152	250153	250154	250155	250156	250157
250158	250159	250165	250166	250167	250170	250171	250172	250173	250174
250212	250213	250216	250217	250218	250220	250223	250224	250276	250277
250278	250279	250280	250281	250282	250306	250307	250308	250309	250310
250313	250318	250319	250322	250324	250325	250327	250328	250336	250482
250483	250593	250594	250595	250596	250597	250681	250698	250702	250703
250782	250786	250788	250790	250794	250795	250837	250838	250840	250842
250847	250848	250849	250862	250864	250865	250866	250873	250875	250877
250878	250879	250883	250885	250886	250887	250971	250972	250973	250975
250977	250978	251049	251050	251053	251054	251055	251059	251060	251061
251063	251064	251065	251101	251102	251105	251106	251107	251109	251111
251125	251127	251133	251136	251329	251331	251332	251333	251334	251338
251412	251416	251417	251419	251485	251486	251487	251489	251491	251492
251497	251498	251499	251500	251501	251502	251503	251510	251511	251512
251685	251687	251689	251690	251692	251694	251695	251697	251819	251822
251823	251824	251826	251827	251829	251836	251838	251839	251840	251841
251842	251843	251846	251849	251850	251851	251852	251853	251854	251855
251857	251858	251859	251860	251862	251863	251946	251947	251948	251949
251951	251952	251956	251960	251961	251962	251963	251964	251965	251969
251971	251975	251976	251977	251978	251979	251988	251989	251992	251993
252102	252103	252104	252105	252106	252107	252115	252116	252117	252118
252119	252120	252121	252123	252124	252125	252127	252128	252130	252131
252134	252135	252140	252141	252143	252144	252145	252146	252147	252148
252187	252190	252193	252196	252197	252201	252202	252203	252209	252210

Table C.2: List of analysed d+Au runs at $\sqrt{s_{\mathrm{NN}}} = 200$ GeV (continued).

252216	252219	252220	252222	252224	252225	252228	252232	252233	252235
252238	252239	252240	252242	252255	252256	252257	252259	252262	252501
252503	252504	252505	252506	252507	252514	252517	252520	252521	252524
252525	252526	252614	252616	252618	252622	252623	252625	252626	252632
252633	252634	252650	252654	252655	252656	252658	252661	252773	252774
252775	252776	252777	252781	252783	252787	252793	252927	252928	252929
252930	252931	252935	252936	252937	252939	252949	252950	252951	252952
252954	252956	252957	252961	252962	252966	252967	252968	252969	252973
252975	252976	252977	252979	252981	253020	253022	253023	253024	253025
253029	253036	253037	253038	253039	253040	253092	253093	253095	253097
253098	253101	253102	253140	253141	253143	253144	253145	253147	253151
253152	253153	253154	253156	253157	253161	253295	253296	253297	253298
253299	253301	253302	253317	253318	253428	253433	253434	253435	253436
253437	253440	253442	253443	253444	253445	253447	253450	253451	253456
253458	253459	253460	253462	253523	253524	253525	253526	253535	253536
253539	253540	253541	253567	253568	253569	253570	253571	253572	253629
253631	253632	253633	253634	253692	253693	253697	253698	253699	253700
253701									

Table C.3: List of analysed d+Au runs at $\sqrt{s_{\mathrm{NN}}} = 200$ GeV (continued).

D. Bad Module and Hit Maps

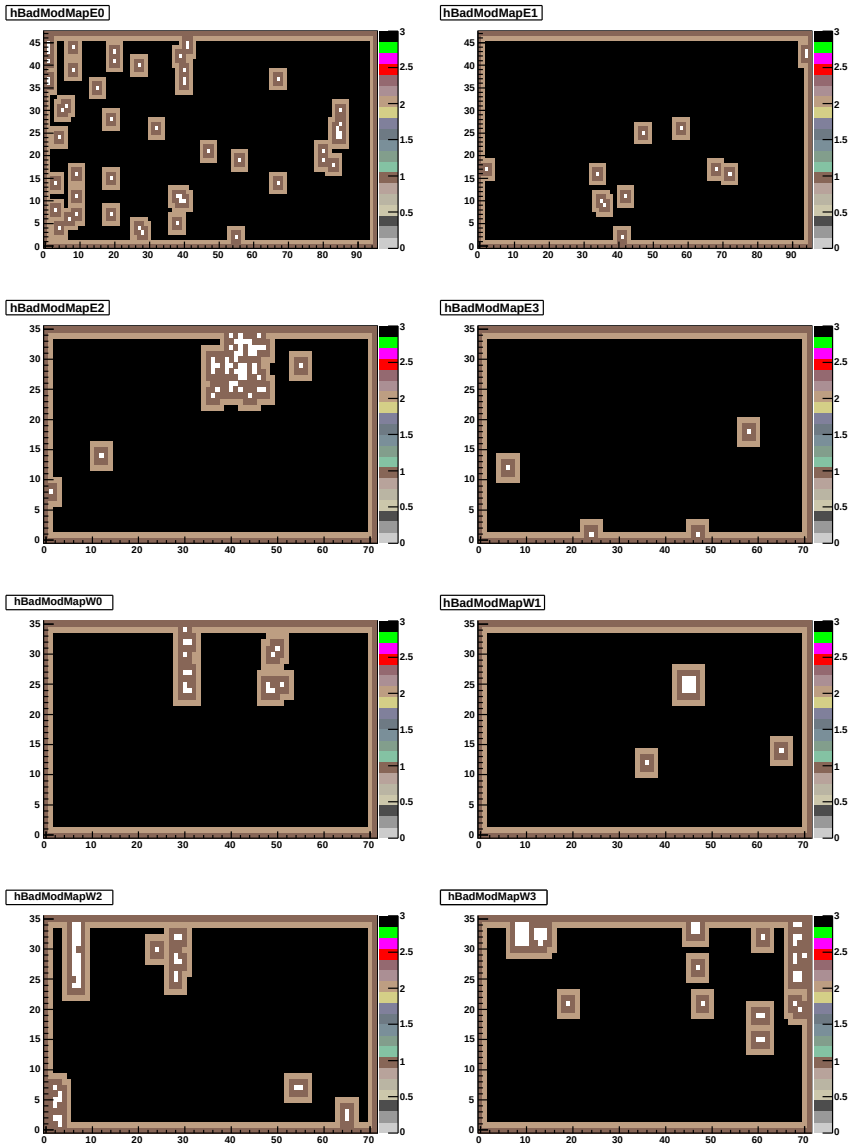

Figure D.1: Overview of the modules marked as bad for the individual sectors of the PHENIX EMCal for MinBias data. Bad modules are marked in white. The neighbours of rejected modules are marked in brown as well as the edges. Accepted modules are marked in black and beige.

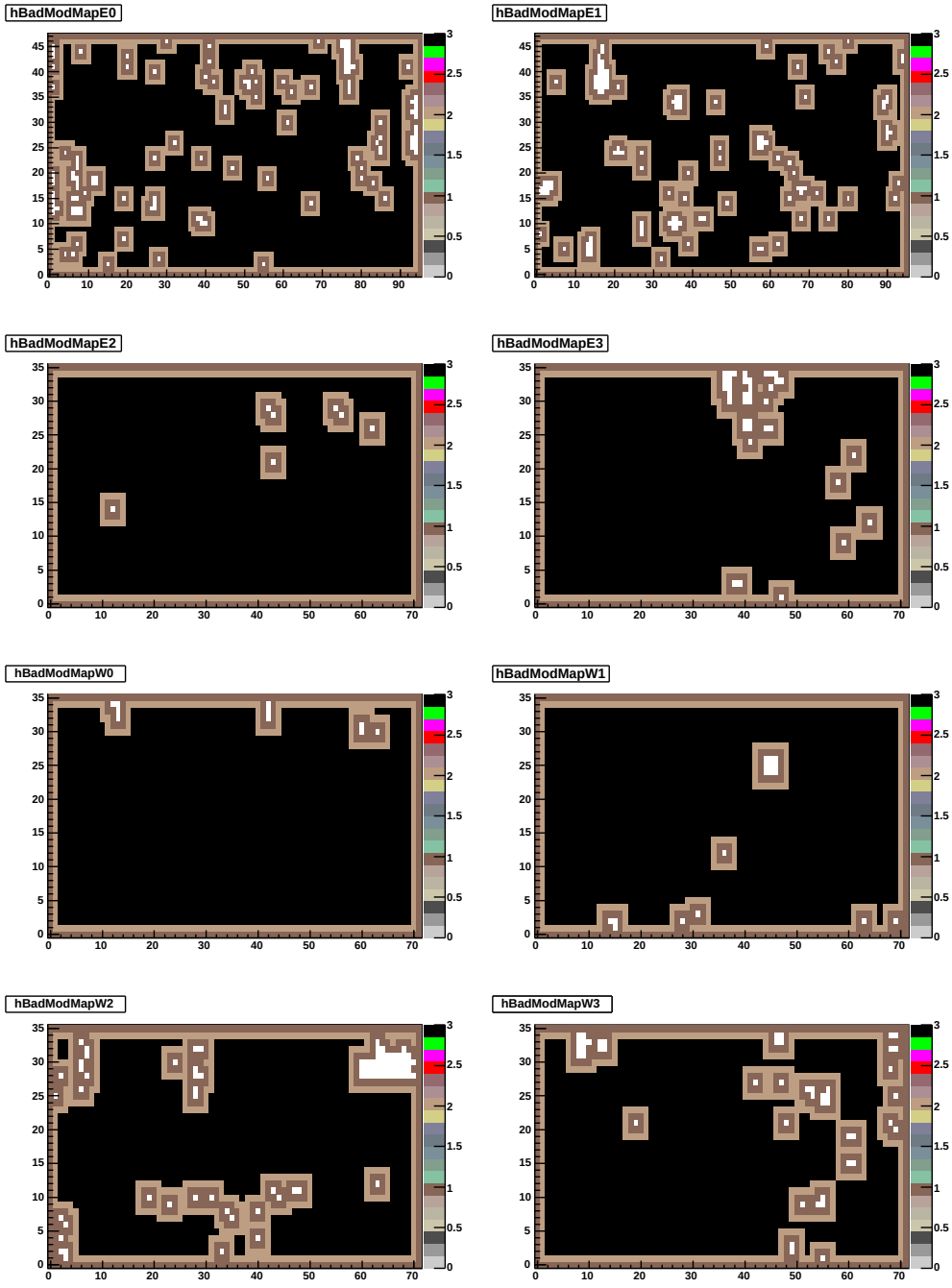

Figure D.2: Overview of the modules marked as bad for the individual sectors of the PHENIX EMCal for ERT data. Bad modules are marked in white. The neighbours of rejected modules are marked in brown as well as the edges. Accepted modules are marked in black and beige.

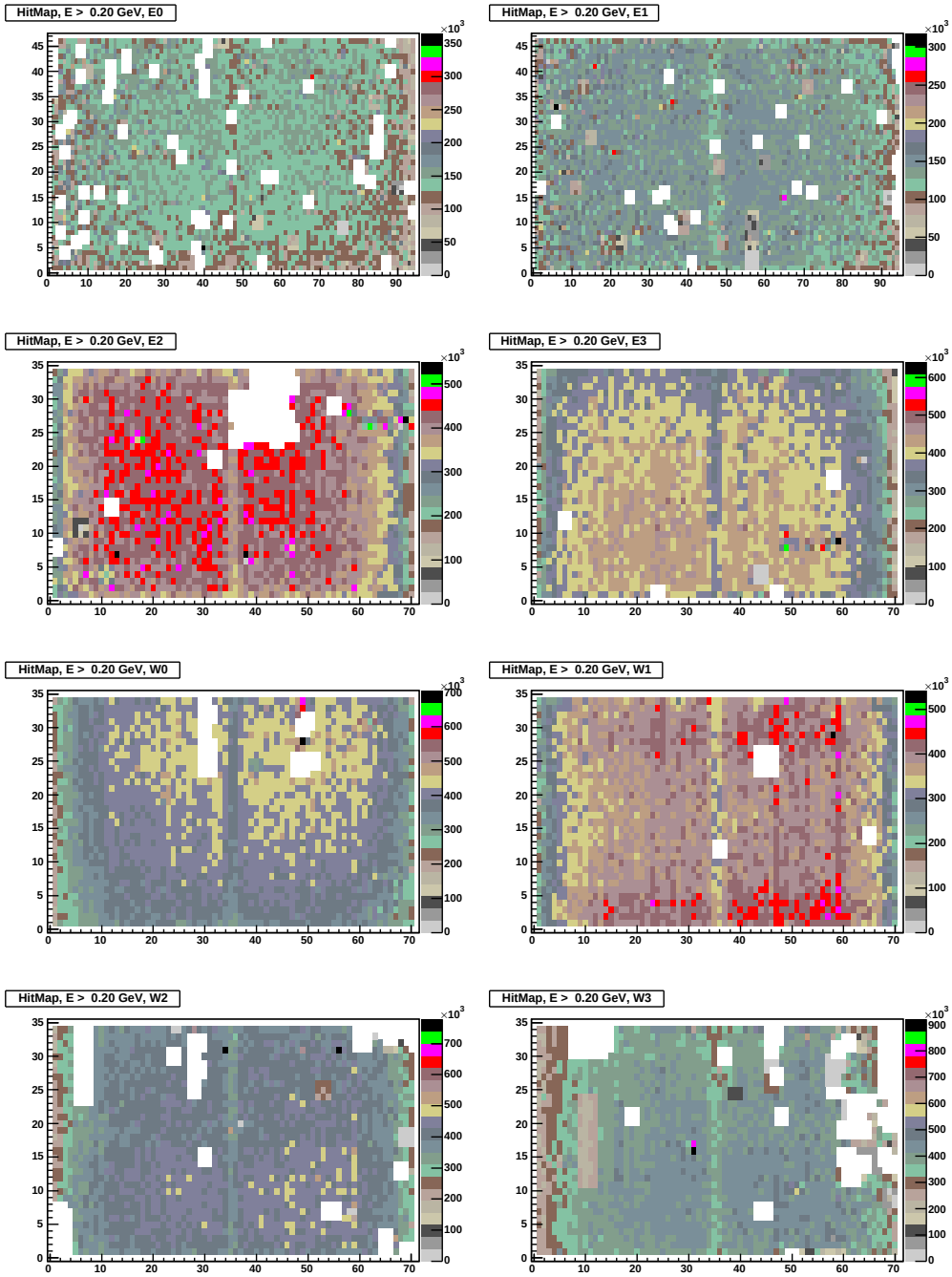

Figure D.3: Overview of the hits in each module for the individual sectors of the PHENIX EMCal for MinBias data with energies $E > 0.2$ GeV/c.

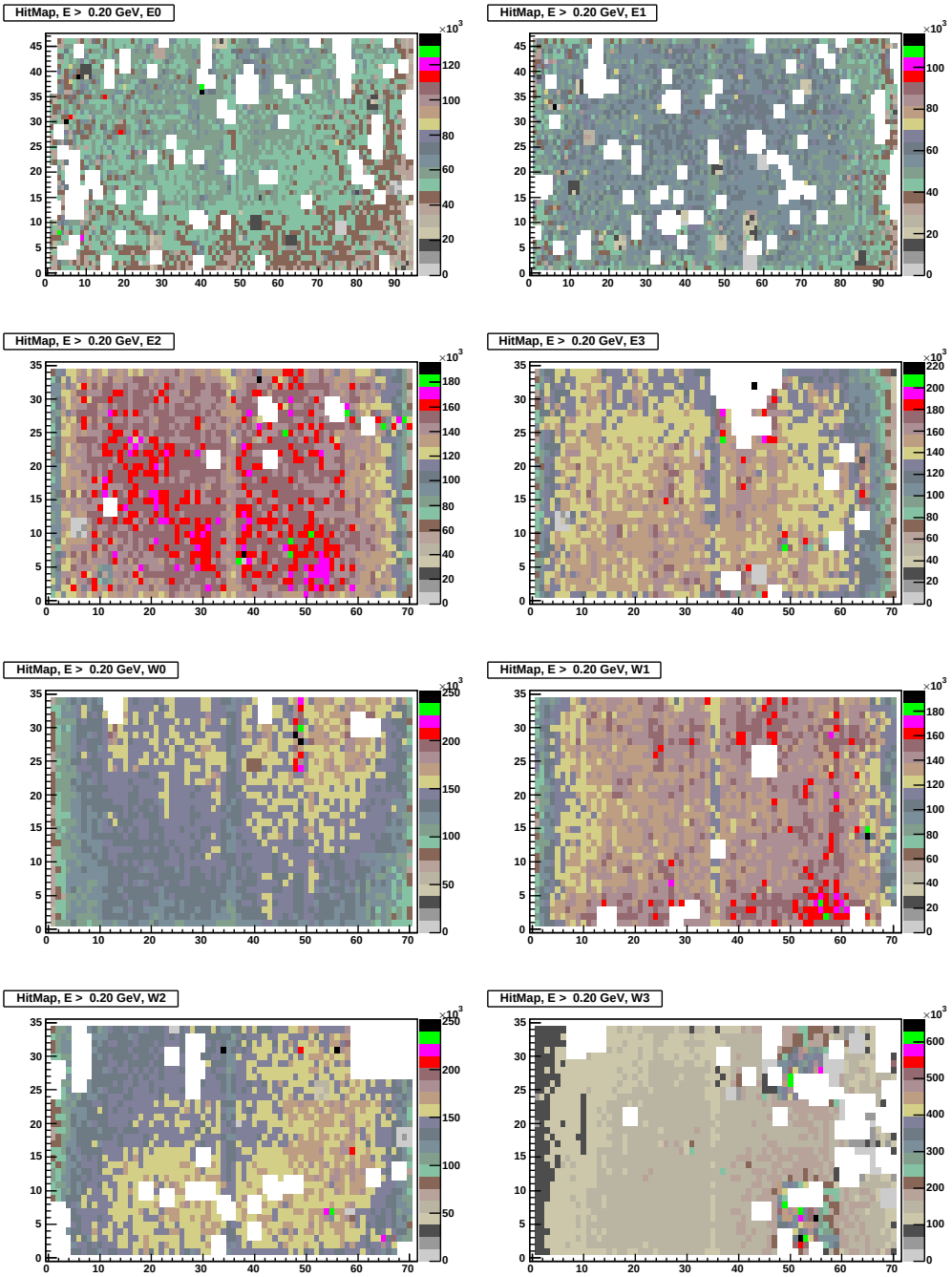

Figure D.4: Overview of the hits in each module for the individual sectors of the PHENIX EMCal for ERT data with energies $E > 0.2$ GeV/c.

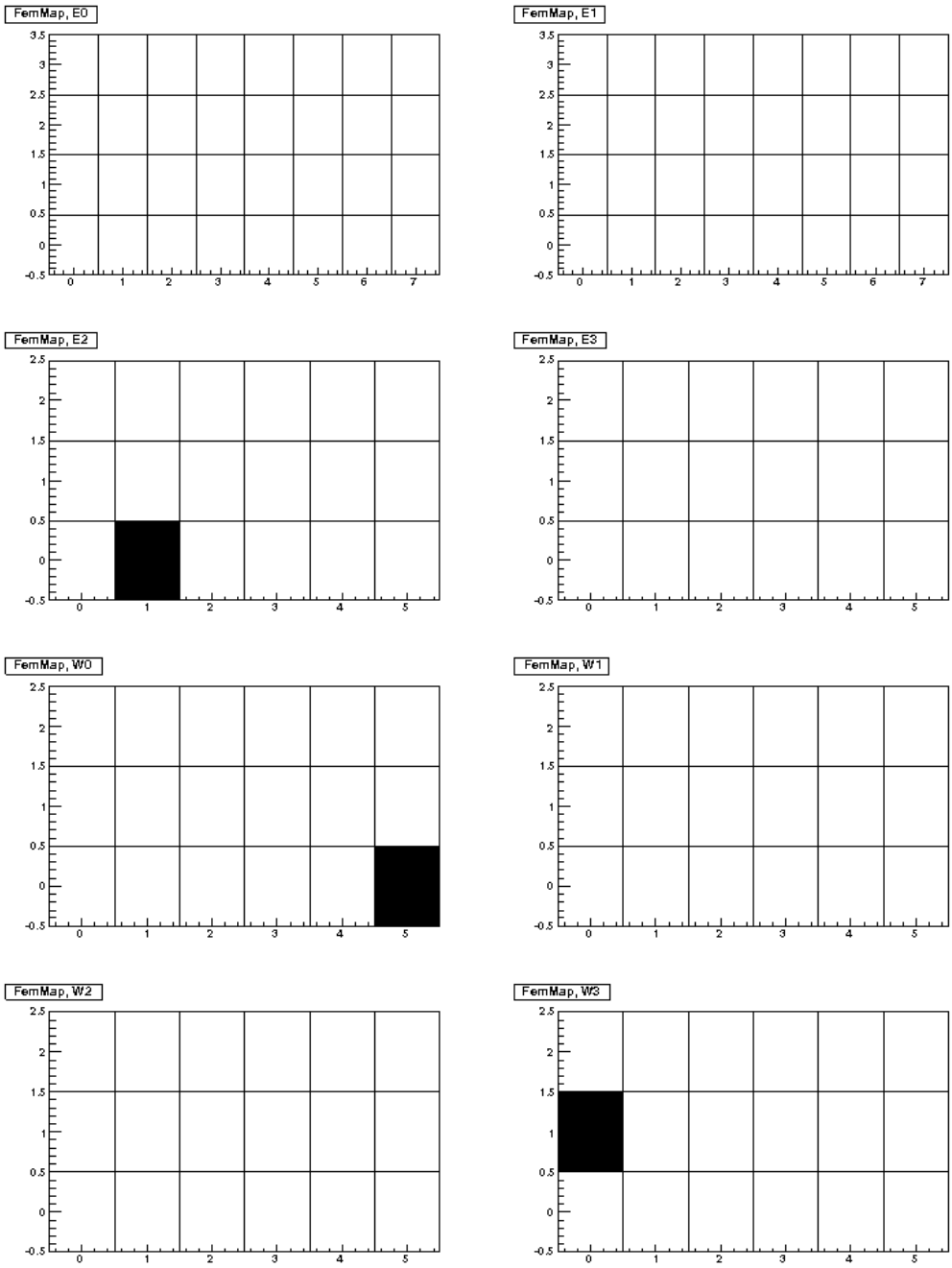

Figure D.5: Overview of the *Front-End-Modules* for the individual sectors of the PHENIX EMCal. Active modules are depicted in white and masked FEMs are depicted in black.

E. Peak Positions and Widths

Comparisons of the peak positions and peak widths of the analysed data and the simulations are depicted. The red and green dots represent the data points and the black and blue lines describe the results of the fastMC simulation. The comparison is shown for both detector types (PbSc and PbGl), all centrality classes, and two PID cuts.

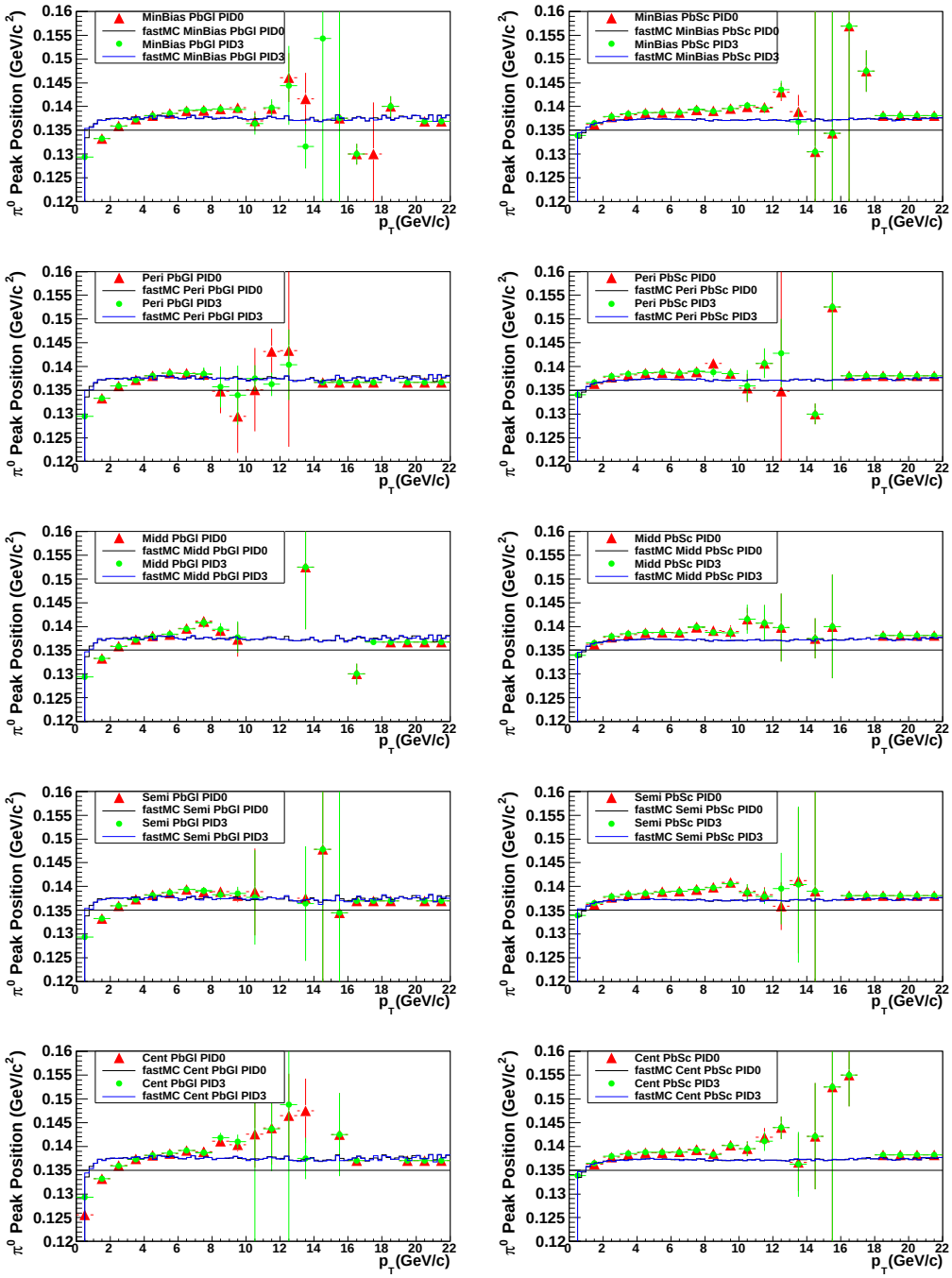

Figure E.1: Comparison of the peak position of the fastMC simulation and the measured data for MinBias triggered events. The black (PID0) and the blue (PID3) lines show the results of the simulation. The red (PID0) and green (PID3) points describe the peak position of the measured data. The straight line at 135 MeV/c^2 marks the expected mass of the π^0. In the left column, the results for the lead glass calorimeter are shown and the right column describes the result of the lead scintillator.

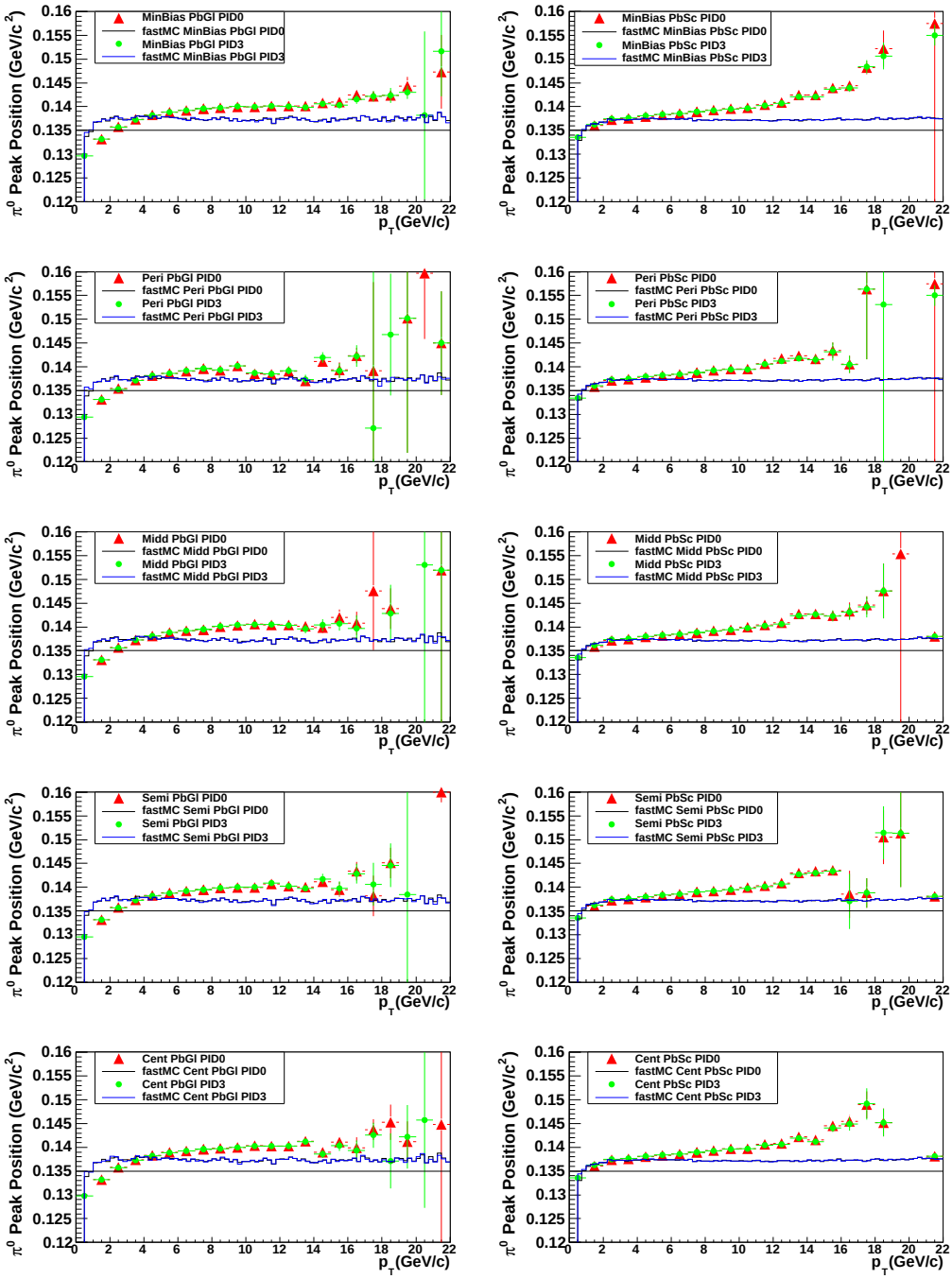

Figure E.2: Comparison of the peak position of the fastMC simulation and the measured data for ERT triggered events. The black (PID0) and the blue (PID3) lines show the results of the simulation. The red (PID0) and green (PID3) points describe the peak position of the measured data. The straight line at 135 MeV/c^2 marks the expected mass of the π^0. In the left column, the results for the lead glass calorimeter are shown and the right column describes the result of the lead scintillator.

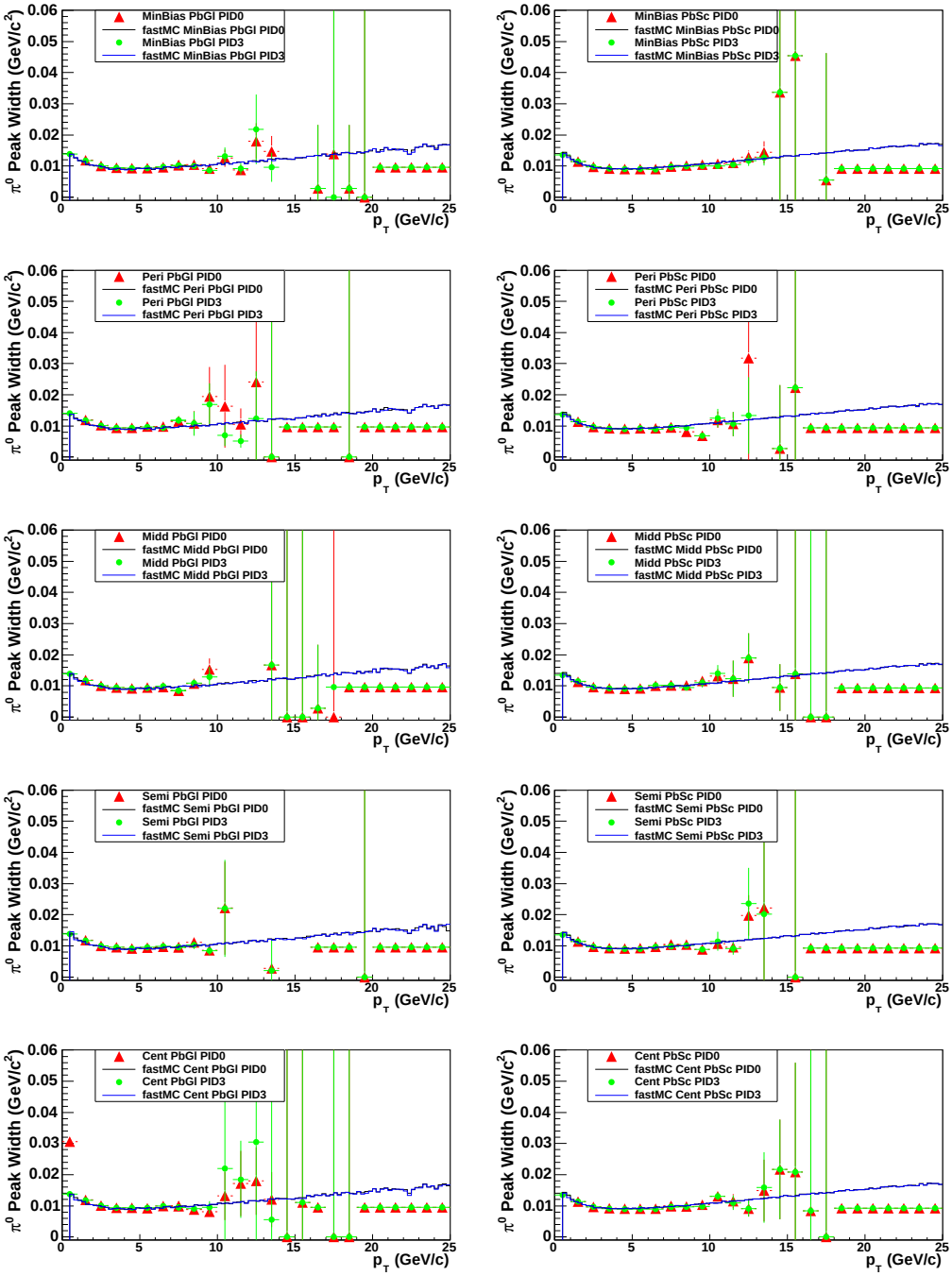

Figure E.3: Comparison of the peak width of the fastMC simulation and the measured data for MinBias triggered events. The black (PID0) and the blue (PID3) lines show the results of the simulation. The red (PID0) and green (PID3) points describe the peak width of the measured data. In the left column the results for the lead glass calorimeter are shown and the right column describes the result for the lead scintillator.

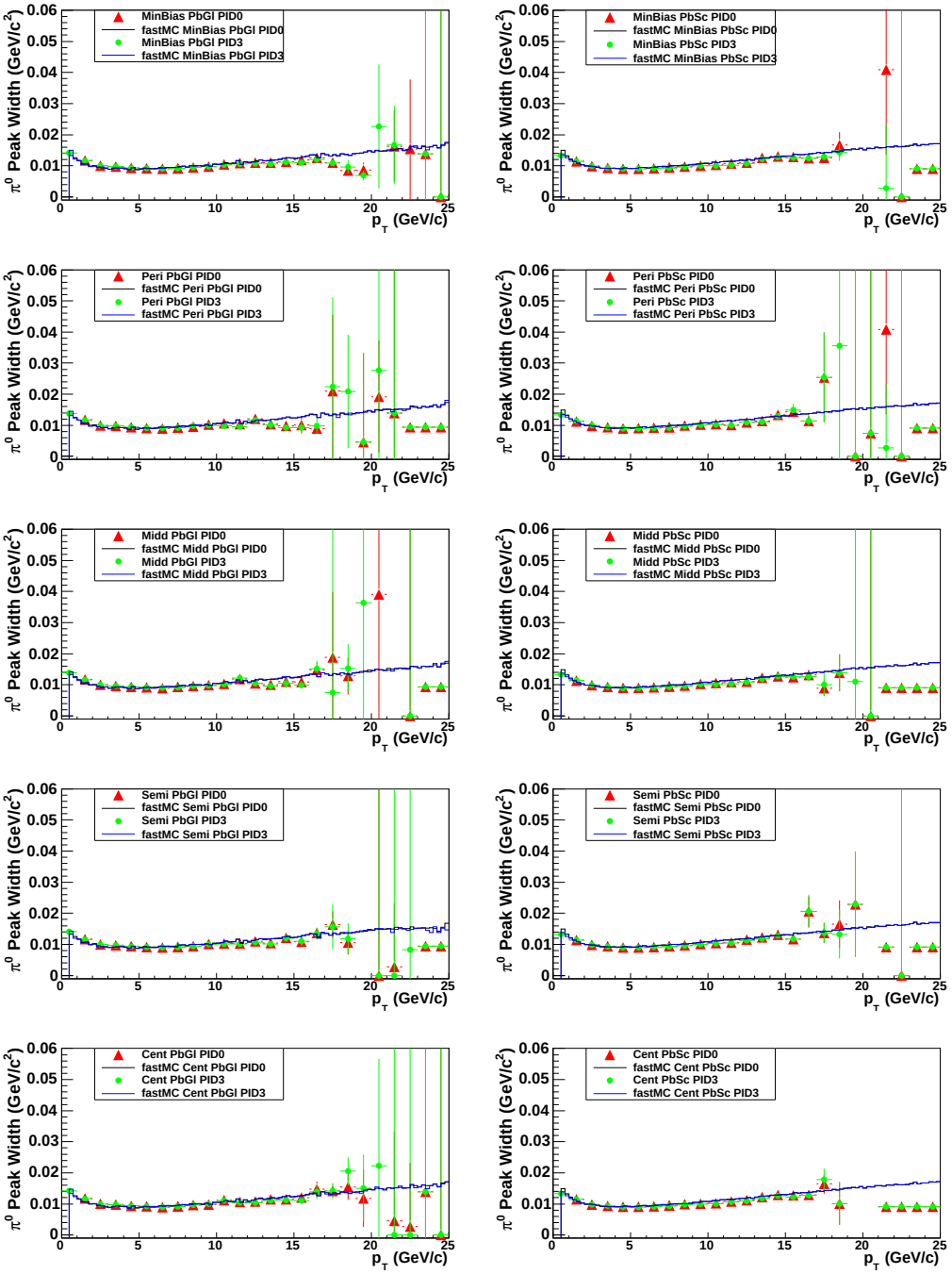

Figure E.4: Comparison of the peak width of the fastMC simulation and the measured data for ERT triggered events. The black (PID0) and the blue (PID3) lines show the results of the simulation. The red (PID0) and green (PID3) points describe the peak width of the measured data. In the left column the results for the lead glass calorimeter are shown and the right column describes the result for the lead scintillator.

F. Data Tables

This chapter comprises the data tables for the Lorentz-invariant yields of d+Au collisions at $\sqrt{s_{\mathrm{NN}}} = 200$ GeV as well as the results for the nuclear modification factor. The results are listed for all centrality classes. Uncertainties are partly abreviated with the notation *error*, systemetical uncertainties with *sys. err*, statistical uncertainties with *stat. err*, and total uncertainties with *tot. err*.

p_{T}	**inv. yield**	**tot. err**	**stat. err**	**sys. err**	**error B**	**error C**
0.25	2.5760	0.176882	0.0615981	0.165809	0.165809	0
0.75	0.353605	0.0227602	0.00401537	0.0224032	0.0224032	0
1.25	0.0512317	0.00420865	0.000521113	0.00417627	0.00417627	0
1.75	0.00975063	0.00081479	9.53248e-05	0.000809195	0.000809195	0
2.25	0.00236415	0.000210624	2.27972e-05	0.000209387	0.000209387	0
2.75	0.000664819	6.22837e-05	6.32735e-06	6.19615e-05	6.19615e-05	0
3.25	0.00021145	2.0599e-05	2.01423e-06	2.05003e-05	2.05003e-05	0
3.75	7.35674e-05	7.38904e-06	7.20002e-07	7.35388e-06	7.35388e-06	0
4.25	2.83971e-05	2.92359e-06	2.94672e-07	2.9087e-06	2.9087e-06	0
4.75	1.1676e-05	1.2294e-06	1.37382e-07	1.2217e-06	1.2217e-06	0
5.25	5.22056e-06	5.59078e-07	6.80784e-08	5.54917e-07	5.54917e-07	0
5.75	2.53513e-06	2.7663e-07	4.10647e-08	2.73565e-07	2.73565e-07	0
6.25	1.27248e-06	1.42158e-07	2.4579e-08	1.40017e-07	1.40017e-07	0
6.75	6.97093e-07	7.8803e-08	1.4199e-08	7.75132e-08	7.75132e-08	0
7.25	3.8759e-07	4.45393e-08	8.72494e-09	4.36763e-08	4.36763e-08	0
7.75	2.19063e-07	2.43267e-08	2.2142e-09	2.42258e-08	2.42258e-08	0
8.25	1.34491e-07	1.50236e-08	1.38844e-09	1.49593e-08	1.49593e-08	0
8.75	8.56033e-08	9.61779e-09	8.99501e-10	9.57564e-09	9.57564e-09	0
9.25	5.41518e-08	6.11446e-09	5.948e-10	6.08546e-09	6.08546e-09	0
9.75	3.61047e-08	4.09027e-09	4.15007e-10	4.06916e-09	4.06916e-09	0
11.00	1.35127e-08	1.54192e-09	1.27462e-10	1.53665e-09	1.53665e-09	0
13.00	3.5226e-09	4.23944e-10	4.79069e-11	4.21228e-10	4.21228e-10	0
15.00	1.02418e-09	1.62098e-10	2.25443e-11	1.60522e-10	1.60522e-10	0
17.00	3.4657e-10	5.37452e-11	1.07852e-11	5.26519e-11	5.26519e-11	0
19.00	8.14845e-11	1.68727e-11	5.43232e-12	1.59743e-11	1.59743e-11	0
21.00	2.27983e-11	6.95476e-12	3.33423e-12	6.10342e-12	6.10342e-12	0

Table F.1: Data table of the invariant yield measured in d+Au 0-88% events. The given uncertainties represent the absolute uncertainties. The total uncertainty reflect the stat. plus the sys. uncertainty; sys. uncertainties reflect the total sys. uncertainty; uncertainty B reflects the sys. uncertainties which are correlated in p_T but allow the shape of the result to change; uncertainty C reflects the normalisation uncertainty.

p_{T}	**inv. yield**	**tot. err**	**stat. err**	**sys. err**	**error B**	**error C**
0.25	1.29604	0.0967048	0.035371	0.090004	0.090004	0
0.75	0.165387	0.0113841	0.00194711	0.0112164	0.0112164	0
1.25	0.0215849	0.00184786	0.000223117	0.00183434	0.00183434	0
1.75	0.00386751	0.000336165	3.8372e-05	0.000333968	0.000333968	0
2.25	0.000915109	8.44469e-05	9.09799e-06	8.39553e-05	8.39553e-05	0
2.75	0.000251268	2.43365e-05	2.57828e-06	2.41995e-05	2.41995e-05	0
3.25	7.91645e-05	7.97154e-06	8.8658e-07	7.92209e-06	7.92209e-06	0
3.75	2.75486e-05	2.86799e-06	3.61458e-07	2.84512e-06	2.84512e-06	0
4.25	1.0921e-05	1.17115e-06	1.75112e-07	1.15798e-06	1.15798e-06	0
4.75	4.57646e-06	5.07118e-07	9.1892e-08	4.98723e-07	4.98723e-07	0
5.25	2.04927e-06	2.31969e-07	4.50168e-08	2.27559e-07	2.27559e-07	0
5.75	1.04907e-06	1.23107e-07	2.9065e-08	1.19627e-07	1.19627e-07	0
6.25	5.2192e-07	6.67876e-08	2.3084e-08	6.26714e-08	6.26714e-08	0
6.75	3.05179e-07	4.03441e-08	1.37065e-08	3.79444e-08	3.79444e-08	0
7.25	1.64804e-07	2.49238e-08	1.14493e-08	2.21384e-08	2.21384e-08	0
7.75	9.61298e-08	1.09904e-08	1.28741e-09	1.09147e-08	1.09147e-08	0
8.25	5.89842e-08	6.81017e-09	9.06458e-10	6.74958e-09	6.74958e-09	0
8.75	3.88286e-08	4.52132e-09	5.97595e-10	4.48165e-09	4.48165e-09	0
9.25	2.492e-08	2.9309e-09	4.34139e-10	2.89857e-09	2.89857e-09	0
9.75	1.63684e-08	1.96078e-09	3.88294e-10	1.92194e-09	1.92194e-09	0
11.00	6.24529e-09	7.38852e-10	1.03571e-10	7.31557e-10	7.31557e-10	0
13.00	1.6531e-09	2.23437e-10	7.04236e-11	2.12048e-10	2.12048e-10	0
15.00	4.95439e-10	7.72651e-11	2.26995e-11	7.38555e-11	7.38555e-11	0
17.00	1.59161e-10	3.22882e-11	1.32267e-11	2.94548e-11	2.94548e-11	0
19.00	2.20978e-11	9.23451e-12	5.47595e-12	7.43574e-12	7.43574e-12	0
21.00	1.75478e-11	8.92889e-12	5.50678e-12	7.02855e-12	7.02855e-12	0

Table F.2: Data table of the inv. yield measured in d+Au 60-88% peripheral events. The given uncertainties represent the absolute uncertainties. The total uncertainty reflect the stat. plus the sys. uncertainty; sys. uncertainties reflect the total sys. uncertainty; uncertainty B reflects the sys. uncertainties which are correlated in p_T but allow the shape of the result to change; uncertainty C reflects the normalisation uncertainty.

p_{T}	**inv. yield**	**tot. err**	**stat. err**	**sys. err**	**error B**	**error C**
0.25	2.2559	0.160634	0.0659149	0.146488	0.146488	0
0.75	0.311038	0.0198609	0.00368619	0.0195159	0.0195159	0
1.25	0.0438264	0.00357605	0.000451458	0.00354744	0.00354744	0
1.75	0.00814115	0.000675828	8.07379e-05	0.000670988	0.000670988	0
2.25	0.0019693	0.000174477	1.94673e-05	0.000173387	0.000173387	0
2.75	0.000552928	5.15862e-05	5.54497e-06	5.12873e-05	5.12873e-05	0
3.25	0.000174757	1.69805e-05	1.84023e-06	1.68805e-05	1.68805e-05	0
3.75	6.1629e-05	6.19398e-06	7.3763e-07	6.1499e-06	6.1499e-06	0
4.25	2.36458e-05	2.45094e-06	3.43828e-07	2.4267e-06	2.4267e-06	0
4.75	9.91188e-06	1.05787e-06	1.84919e-07	1.04158e-06	1.04158e-06	0
5.25	4.64852e-06	5.04629e-07	8.34671e-08	4.97679e-07	4.97679e-07	0
5.75	2.21283e-06	2.47976e-07	5.15111e-08	2.42567e-07	2.42567e-07	0
6.25	1.16781e-06	1.36752e-07	3.4617e-08	1.32298e-07	1.32298e-07	0
6.75	6.20627e-07	7.82698e-08	2.57439e-08	7.39149e-08	7.39149e-08	0
7.25	3.27532e-07	4.34949e-08	1.61208e-08	4.03971e-08	4.03971e-08	0
7.75	1.986e-07	2.20938e-08	2.45522e-09	2.1957e-08	2.1957e-08	0
8.25	1.23268e-07	1.382e-08	1.63075e-09	1.37235e-08	1.37235e-08	0
8.75	7.70337e-08	8.69652e-09	1.08391e-09	8.62871e-09	8.62871e-09	0
9.25	4.97976e-08	5.67543e-09	7.79145e-10	5.62169e-09	5.62169e-09	0
9.75	3.37775e-08	3.88296e-09	5.90101e-10	3.83786e-09	3.83786e-09	0
11.00	1.26395e-08	1.45259e-09	1.79033e-10	1.44151e-09	1.44151e-09	0
13.00	3.31201e-09	4.09623e-10	7.6494e-11	4.02417e-10	4.02417e-10	0
15.00	1.03467e-09	1.52856e-10	4.06039e-11	1.47365e-10	1.47365e-10	0
17.00	3.24655e-10	6.03625e-11	2.23613e-11	5.60678e-11	5.60678e-11	0
19.00	5.84007e-11	1.93404e-11	1.03273e-11	1.63523e-11	1.63523e-11	0
21.00	6.41851e-12	6.08827e-12	4.11992e-12	4.48256e-12	4.48256e-12	0

Table F.3: Data table of the inv. yield measured in d+Au 40-60% semiperipheral events. The given uncertainties represent the absolute uncertainties. The total uncertainty reflect the stat. plus the sys. uncertainty; sys. uncertainties reflect the total sys. uncertainty; uncertainty B reflects the sys. uncertainties which are correlated in p_T but allow the shape of the result to change; uncertainty C reflects the normalisation uncertainty.

p_{T}	**inv. yield**	**tot. err**	**stat. err**	**sys. err**	**error B**	**error C**
0.25	3.47034	0.351433	0.0997171	0.225966	0.225966	0
0.75	0.439159	0.0418506	0.00517714	0.0276919	0.0276919	0
1.25	0.0641394	0.00781549	0.00066127	0.00520935	0.00520935	0
1.75	0.0121644	0.00153731	0.000120387	0.00100573	0.00100573	0
2.25	0.00296675	0.000403627	2.91441e-05	0.000261909	0.000261909	0
2.75	0.000842758	0.000118548	8.30753e-06	7.83391e-05	7.83391e-05	0
3.25	0.000268008	3.87606e-05	2.72801e-06	2.59323e-05	2.59323e-05	0
3.75	9.50789e-05	1.37522e-05	1.03753e-06	9.49655e-06	9.49655e-06	0
4.25	3.63359e-05	5.43567e-06	4.58918e-07	3.72436e-06	3.72436e-06	0
4.75	1.55354e-05	2.25392e-06	2.23215e-07	1.6285e-06	1.6285e-06	0
5.25	6.7704e-06	1.01323e-06	1.21537e-07	7.23225e-07	7.23225e-07	0
5.75	3.31401e-06	4.96197e-07	6.39206e-08	3.6082e-07	3.6082e-07	0
6.25	1.6956e-06	2.59349e-07	4.29408e-08	1.89395e-07	1.89395e-07	0
6.75	9.04008e-07	1.47768e-07	2.85861e-08	1.03614e-07	1.03614e-07	0
7.25	5.05358e-07	8.29128e-08	1.96346e-08	5.99958e-08	5.99958e-08	0
7.75	2.83061e-07	4.17331e-08	3.27098e-09	3.12801e-08	3.12801e-08	0
8.25	1.71719e-07	2.59714e-08	2.16773e-09	1.91196e-08	1.91196e-08	0
8.75	1.09909e-07	1.64929e-08	1.42644e-09	1.23096e-08	1.23096e-08	0
9.25	7.08257e-08	1.02119e-08	1.00371e-09	7.99027e-09	7.99027e-09	0
9.75	4.64186e-08	6.7665e-09	7.31579e-10	5.25869e-09	5.25869e-09	0
11.00	1.77536e-08	2.54253e-09	2.15946e-10	2.02298e-09	2.02298e-09	0
13.00	4.661e-09	6.89536e-10	8.8105e-11	5.62227e-10	5.62227e-10	0
15.00	1.34104e-09	2.3984e-10	4.48923e-11	1.88648e-10	1.88648e-10	0
17.00	4.68187e-10	8.69633e-11	2.60573e-11	7.72384e-11	7.72384e-11	0
19.00	1.1778e-10	3.10645e-11	1.43907e-11	2.67193e-11	2.67193e-11	0
21.00	1.48566e-11	1.52761e-11	6.23439e-12	7.24845e-12	7.24845e-12	0

Table F.4: Data table of the inv. yield measured in d+Au 20-40% semicentral events. The given uncertainties represent the absolute uncertainties. The total uncertainty reflect the stat. plus the sys. uncertainty; sys. uncertainties reflect the total sys. uncertainty; uncertainty B reflects the sys. uncertainties which are correlated in p_T but allow the shape of the result to change; uncertainty C reflects the normalisation uncertainty.

p_{T}	**inv. yield**	**tot. err**	**stat. err**	**sys. err**	**error B**	**error C**
0.25	4.59721	0.351433	0.125623	0.328214	0.328214	0
0.75	0.592087	0.0418506	0.00696401	0.0412671	0.0412671	0
1.25	0.0897675	0.00781549	0.00092238	0.00776087	0.00776087	0
1.75	0.0173918	0.00153731	0.000171691	0.00152769	0.00152769	0
2.25	0.00431058	0.000403627	4.21242e-05	0.000401423	0.000401423	0
2.75	0.00120894	0.000118548	1.18074e-05	0.000117959	0.000117959	0
3.25	0.000381224	3.87606e-05	3.79436e-06	3.85744e-05	3.85744e-05	0
3.75	0.000131391	1.37522e-05	1.40154e-06	1.36806e-05	1.36806e-05	0
4.25	5.06704e-05	5.43567e-06	6.10978e-07	5.40122e-06	5.40122e-06	0
4.75	2.04911e-05	2.25392e-06	3.11161e-07	2.23234e-06	2.23234e-06	0
5.25	9.02996e-06	1.01323e-06	1.60679e-07	1.00041e-06	1.00041e-06	0
5.75	4.36818e-06	4.96197e-07	7.79346e-08	4.90038e-07	4.90038e-07	0
6.25	2.21598e-06	2.59349e-07	5.00612e-08	2.54472e-07	2.54472e-07	0
6.75	1.19987e-06	1.47768e-07	4.17925e-08	1.41734e-07	1.41734e-07	0
7.25	6.65392e-07	8.29128e-08	2.22309e-08	7.9877e-08	7.9877e-08	0
7.75	3.6287e-07	4.17331e-08	4.12035e-09	4.15292e-08	4.15292e-08	0
8.25	2.24676e-07	2.59714e-08	2.56367e-09	2.58445e-08	2.58445e-08	0
8.75	1.41683e-07	1.64929e-08	1.74558e-09	1.64003e-08	1.64003e-08	0
9.25	8.72181e-08	1.02119e-08	1.15063e-09	1.01469e-08	1.01469e-08	0
9.75	5.74518e-08	6.7665e-09	8.4773e-10	6.71319e-09	6.71319e-09	0
11.00	2.14888e-08	2.54253e-09	2.52718e-10	2.52994e-09	2.52994e-09	0
13.00	5.47733e-09	6.89536e-10	1.08359e-10	6.80969e-10	6.80969e-10	0
15.00	1.64098e-09	2.3984e-10	4.74969e-11	2.35089e-10	2.35089e-10	0
17.00	4.99861e-10	8.69633e-11	2.64157e-11	8.28543e-11	8.28543e-11	0
19.00	1.20361e-10	3.10645e-11	1.38806e-11	2.77909e-11	2.77909e-11	0
21.00	3.6386e-11	1.52761e-11	8.91095e-12	1.24079e-11	1.24079e-11	0

Table F.5: Data table of the inv. yield measured in d+Au 00-20% most central events. The given uncertainties represent the absolute uncertainties. The total uncertainty reflect the stat. plus the sys. uncertainty; sys. uncertainties reflect the total sys. uncertainty; uncertainty B reflects the sys. uncertainties which are correlated in p_T but allow the shape of the result to change; uncertainty C reflects the normalisation uncertainty.

p_{T}	R_{dA}	**tot. err**	**stat. err**	**sys. err**	**error B**	**error C**
1.25	0.745116	0.11518	0.00810214	0.111791	0.111791	0.0265261
1.75	0.88227	0.142536	0.00960921	0.1387	0.1387	0.0314088
2.25	0.987403	0.169412	0.0113843	0.165333	0.165333	0.0351515
2.75	1.08041	0.193507	0.0136644	0.189153	0.189153	0.0384627
3.25	1.13965	0.210515	0.0166015	0.205901	0.205901	0.0405716
3.75	1.17237	0.221698	0.0205771	0.216759	0.216759	0.0417364
4.25	1.23867	0.245193	0.0151809	0.240717	0.240717	0.0440965
4.75	1.23353	0.247693	0.0178683	0.243113	0.243113	0.0439138
5.25	1.24004	0.251781	0.0209086	0.246998	0.246998	0.0441453
5.75	1.25057	0.256932	0.0267917	0.251623	0.251623	0.0445202
6.25	1.25123	0.26085	0.0329568	0.254897	0.254897	0.0445436
6.75	1.29063	0.271605	0.0382321	0.264947	0.264947	0.0459465
7.25	1.25732	0.267866	0.042984	0.260579	0.260579	0.0447605
7.75	1.21518	0.255429	0.0301169	0.249931	0.249931	0.0432605
8.25	1.24802	0.264404	0.0357071	0.258187	0.258187	0.0444294
8.75	1.24574	0.266196	0.0402872	0.259366	0.259366	0.0443484
9.25	1.28201	0.276492	0.0489266	0.268274	0.268274	0.0456396
9.75	1.36878	0.298059	0.0620979	0.287417	0.287417	0.0487284
11.00	1.26045	0.278585	0.0424097	0.271657	0.271657	0.044872
13.00	1.26739	0.305544	0.0756294	0.292578	0.292578	0.0451193
15.00	1.46241	0.437285	0.151559	0.406864	0.406864	0.0520619
17.00	1.44989	0.486851	0.237188	0.422021	0.422021	0.0516161
19.00	0.771276	0.346877	0.212374	0.272887	0.272887	0.0274574

Table F.6: Data table of R_{dA} 0-88% events. The uncertainties are absolute uncertainties. The total uncertainty reflect the stat. plus the sys. uncertainty; sys. uncertainties reflect the total sys. uncertainty; uncertainty B reflects the sys. uncertainties which are correlated in p_T but allow the shape of the result to change; uncertainty C reflects the normalisation uncertainty from N_{coll}. The normalisation uncertainty of σ_{pp} (9.7%) is not included.

p_{T}	R_{dA}	**tot. err**	**stat. err**	**sys. err**	**error B**	**error C**
1.25	0.86101	0.156951	0.00950445	0.132162	0.132162	0.0841206
1.75	0.959787	0.180711	0.010593	0.154114	0.154114	0.0937711
2.25	1.04825	0.206471	0.0123994	0.178851	0.178851	0.102414
2.75	1.11995	0.228079	0.0149973	0.199556	0.199556	0.109419
3.25	1.17022	0.244315	0.0190051	0.215075	0.215075	0.114331
3.75	1.20407	0.256562	0.0251476	0.226612	0.226612	0.117638
4.25	1.30652	0.289346	0.0234043	0.258611	0.258611	0.127647
4.75	1.32605	0.298402	0.0302319	0.267105	0.267105	0.129555
5.25	1.33503	0.303847	0.0344279	0.272259	0.272259	0.130432
5.75	1.41933	0.328645	0.04674	0.294268	0.294268	0.138669
6.25	1.40755	0.338591	0.0721407	0.300879	0.300879	0.137517
6.75	1.54968	0.380187	0.0839409	0.338487	0.338487	0.151403
7.25	1.46627	0.383824	0.118986	0.335621	0.335621	0.143254
7.75	1.46253	0.339415	0.0410512	0.305123	0.305123	0.142889
8.25	1.50119	0.351456	0.0505228	0.315369	0.315369	0.146666
8.75	1.54976	0.365999	0.0576861	0.328181	0.328181	0.151411
9.25	1.61808	0.386271	0.0721686	0.344971	0.344971	0.158087
9.75	1.70195	0.413251	0.0980243	0.365401	0.365401	0.166281
11.00	1.59775	0.388572	0.0651843	0.349817	0.349817	0.1561
13.00	1.63125	0.44611	0.14465	0.390757	0.390757	0.159373
15.00	1.94025	0.610438	0.247267	0.524938	0.524938	0.189562
17.00	1.82622	0.733065	0.393685	0.592083	0.592083	0.178422
19.00	0.573664	0.390019	0.261873	0.283541	0.283541	0.056047

Table F.7: Data table of R_{dA} 60-88% events. The uncertainties are absolute uncertainties. The total uncertainty reflect the stat. plus the sys. uncertainty; sys. uncertainties reflect the total sys. uncertainty; uncertainty B reflects the sys. uncertainties which are correlated in p_T but allow the shape of the result to change; uncertainty C reflects the normalisation uncertainty from N_{coll}. The normalisation uncertainty of σ_{pp} (9.7%) is not included.

p_{T}	R_{dA}	**tot. err**	**stat. err**	**sys. err**	**error B**	**error C**
1.25	0.772232	0.133545	0.0084969	0.115416	0.115416	0.0666436
1.75	0.892447	0.159907	0.00984586	0.139791	0.139791	0.0770181
2.25	0.996454	0.187611	0.0117303	0.166328	0.166328	0.085994
2.75	1.08863	0.212539	0.0143247	0.190108	0.190108	0.093949
3.25	1.14111	0.228799	0.0177689	0.205756	0.205756	0.0984775
3.75	1.18985	0.243724	0.02348	0.219786	0.219786	0.102684
4.25	1.24957	0.26672	0.0205177	0.243083	0.243083	0.107838
4.75	1.26864	0.274818	0.0271179	0.250605	0.250605	0.109484
5.25	1.3377	0.29278	0.0291305	0.267477	0.267477	0.115444
5.75	1.32246	0.294035	0.0376951	0.268348	0.268348	0.114128
6.25	1.39119	0.316105	0.0510098	0.287934	0.287934	0.120059
6.75	1.3921	0.327869	0.0706272	0.296777	0.296777	0.120138
7.25	1.28722	0.311701	0.0783858	0.280487	0.280487	0.111087
7.75	1.33468	0.299839	0.0360884	0.274471	0.274471	0.115183
8.25	1.38581	0.313822	0.043676	0.286834	0.286834	0.119595
8.75	1.35814	0.310144	0.048761	0.282974	0.282974	0.117208
9.25	1.42829	0.329704	0.0611681	0.299616	0.299616	0.123261
9.75	1.5514	0.362384	0.0796537	0.327188	0.327188	0.133886
11.00	1.42837	0.336541	0.0548182	0.308318	0.308318	0.123268
13.00	1.44367	0.372051	0.0998576	0.336048	0.336048	0.124589
15.00	1.78988	0.542022	0.216337	0.472363	0.472363	0.154467
17.00	1.64548	0.627095	0.331315	0.513141	0.513141	0.142005
19.00	0.669699	0.394907	0.258184	0.293176	0.293176	0.057795

Table F.8: Data table of R_{dA} 40-60% events. The uncertainties are absolute uncertainties. The total uncertainty reflect the stat. plus the sys. uncertainty; sys. uncertainties reflect the total sys. uncertainty; uncertainty B reflects the sys. uncertainties which are correlated in p_T but allow the shape of the result to change; uncertainty C reflects the normalisation uncertainty from N_{coll}. The normalisation uncertainty of σ_{pp} (9.7%) is not included.

p_{T}	R_{dA}	**tot. err**	**stat. err**	**sys. err**	**error B**	**error C**
1.25	0.738905	0.121154	0.00813672	0.110639	0.110639	0.0486938
1.75	0.871841	0.148676	0.00960062	0.13679	0.13679	0.0574543
2.25	0.981475	0.176723	0.0114933	0.16406	0.16406	0.0646792
2.75	1.08485	0.203179	0.0140895	0.189663	0.189663	0.0714913
3.25	1.14417	0.220522	0.0174146	0.206498	0.206498	0.0754009
3.75	1.20017	0.236546	0.0224156	0.221802	0.221802	0.0790912
4.25	1.25544	0.258347	0.018215	0.244062	0.244062	0.0827334
4.75	1.30004	0.271312	0.0222143	0.25647	0.25647	0.0856728
5.25	1.27383	0.269324	0.027734	0.2544	0.2544	0.0839453
5.75	1.29491	0.277178	0.0317426	0.261797	0.261797	0.0853345
6.25	1.32065	0.288043	0.0427212	0.271236	0.271236	0.087031
6.75	1.32576	0.295175	0.0541906	0.276692	0.276692	0.0873673
7.25	1.29852	0.297204	0.0656133	0.276952	0.276952	0.0855727
7.75	1.24374	0.270494	0.0326259	0.255704	0.255704	0.0819627
8.25	1.26218	0.276945	0.0390155	0.261262	0.261262	0.0831779
8.75	1.26692	0.280331	0.0441022	0.26395	0.26395	0.0834903
9.25	1.32816	0.297063	0.0549214	0.278512	0.278512	0.0875256
9.75	1.39393	0.315237	0.0691853	0.293512	0.293512	0.0918598
11.00	1.31174	0.299742	0.0477175	0.283012	0.283012	0.0864438
13.00	1.32833	0.331657	0.0863096	0.308033	0.308033	0.0875372
15.00	1.51674	0.445613	0.174577	0.397621	0.397621	0.0999535
17.00	1.55146	0.564154	0.291871	0.471834	0.471834	0.102241
19.00	0.883047	0.451787	0.292174	0.339646	0.339646	0.0581928

Table F.9: Data table of R_{dA} 20-40% events. The uncertainties are absolute uncertainties. The total uncertainty reflect the stat. plus the sys. uncertainty; sys. uncertainties reflect the total sys. uncertainty; uncertainty B reflects the sys. uncertainties which are correlated in p_T but allow the shape of the result to change; uncertainty C reflects the normalisation uncertainty from N_{coll}. The normalisation uncertainty of σ_{pp} (9.7%) is not included.

p_{T}	R_{dA}	**tot. err**	**stat. err**	**sys. err**	**error B**	**error C**
1.25	0.715225	0.120477	0.00785116	0.110838	0.110838	0.0465611
1.75	0.86209	0.150858	0.00947189	0.139709	0.139709	0.0561221
2.25	0.986263	0.181745	0.0114988	0.169637	0.169637	0.0642057
2.75	1.07629	0.205922	0.0138806	0.193136	0.193136	0.0700667
3.25	1.1256	0.221295	0.0168777	0.208128	0.208128	0.0732763
3.75	1.14705	0.230319	0.0211421	0.21685	0.21685	0.0746732
4.25	1.2108	0.253503	0.0168748	0.240345	0.240345	0.0788231
4.75	1.18593	0.251906	0.0212334	0.238841	0.238841	0.077204
5.25	1.17501	0.252532	0.0253976	0.239325	0.239325	0.0764932
5.75	1.18044	0.255894	0.0272291	0.242559	0.242559	0.0768469
6.25	1.19368	0.263138	0.0353507	0.248904	0.248904	0.0777088
6.75	1.21698	0.275415	0.0536502	0.258261	0.258261	0.0792253
7.25	1.18246	0.270491	0.0533132	0.253766	0.253766	0.0769783
7.75	1.10271	0.243645	0.0287048	0.231053	0.231053	0.0717864
8.25	1.14215	0.254126	0.0339193	0.240626	0.240626	0.0743537
8.75	1.12952	0.253547	0.0385759	0.239565	0.239565	0.0735316
9.25	1.13116	0.256281	0.0456679	0.241188	0.241188	0.0736385
9.75	1.19319	0.273272	0.0580231	0.255494	0.255494	0.0776769
11.00	1.09808	0.25453	0.0395025	0.24107	0.24107	0.071485
13.00	1.07958	0.273287	0.0710974	0.254345	0.254345	0.0702809
15.00	1.28361	0.377636	0.141927	0.339828	0.339828	0.0835631
17.00	1.14559	0.415499	0.212298	0.349295	0.349295	0.0745782
19.00	0.624104	0.318406	0.202217	0.24257	0.24257	0.0406292

Table F.10: Data table of R_{dA} 00-20% events. The uncertainties are absolute uncertainties. The total uncertainty reflect the stat. plus the sys. uncertainty; sys. uncertainties reflect the total sys. uncertainty; uncertainty B reflects the sys. uncertainties which are correlated in p_T but allow the shape of the result to change; uncertainty C reflects the normalisation uncertainty from N_{coll}. The normalisation uncertainty of σ_{pp} (9.7%) is not included.

G. Overview of PHENIX Runs

	Year	Species	$\sqrt{s_{NN}}$ [GeV]	$\int \mathbf{L}dt$	N_{tot} (sampled)	Data Size
Run 1	2000	Au - Au	130	1 μb^{-1}	10 $\cdot 10^6$	3 TB
Run 2	2001/02	Au - Au	200	24 μb^{-1}	170 $\cdot 10^6$	10 TB
		Au - Au	19		$< 1 \cdot 10^6$	
		p - p	200	0.15 pb^{-1}	3.7 $\cdot 10^9$	20 TB
Run 3	2002/03	d - Au	200	2.74 nb^{-1}	5.5 $\cdot 10^9$	46 TB
		p - p	200	0.35 pb^{-1}	6.6 $\cdot 10^9$	35 TB
Run 4	2003/04	Au - Au	200	241 μb^{-1}	1.5 $\cdot 10^9$	270 TB
		Au - Au	62.4	9 μb^{-1}	58 $\cdot 10^6$	10 TB
Run 5	2005	Cu - Cu	200	3 nb^{-1}	8.6 $\cdot 10^9$	173 TB
		Cu - Cu	62.4	0.19 nb^{-1}	0.4 $\cdot 10^9$	48 TB
		Cu - Cu	22.4	2.7 μb^{-1}	9 $\cdot 10^6$	1 TB
		p - p	200	3.8 pb^{-1}	85 $\cdot 10^9$	262 TB
Run 6	2006	p - p	200	10.7 pb^{-1}	233 $\cdot 10^9$	310 TB
		p - p	62.4	0.1 pb^{-1}	28 $\cdot 10^9$	25 TB
Run 7	2007	Au - Au	200	813 μb^{-1}	5.1 $\cdot 10^9$	650 TB
Run 8	2007/08	d - Au	200	80 nb^{-1}	160 $\cdot 10^9$	437 TB
		p - p	200	5.2 pb^{-1}	115 $\cdot 10^9$	118 TB
		Au - Au	9.2		few k	

Table G.1: Overview of the several RHIC runs between the years 2000 and 2008. The information on the collision species, the number of events and the data amount is shown in the columns. The integrated luminosity means the real experimental recorded luminosity [phe09].

H. List of Acronyms

ACC Aerogel Cherenkov Detector

AGS Alternating Gradient Synchrotron

APD Avalanche Photodiode

ASIC Application Specific Integrated Circuit

ATP Assembly Trigger Processors

BBC Beam-Beam-Counters

BBCLL1 Beam-Beam-Counter Local Level 1

BNL Brookhaven National Laboratory

BRAHMS Broad Range Hadron Magnetic Spectrometer

CERN Conseil Européen pour la Recherche Nucléaire

cent central

CGC Colour Glass Condensate

CM Central Magnet

DAQ Data Acquisition

DC Drift Chamber

DCC Disoriented Chiral Condensate

DCM Data Collection Moduls

DESY Deutsches Elektronen-Synchrotron

DST Data Summary Table

EMCal Electromagnetic Calorimeter

ERT EMCal RICH Trigger

EvB Event Builder

fastMC fast Monte Carlo Simulation

FEE Front End Electronic

FEM Front End Module

FF Fragmentation Function

GL1 Global Level-1 System

GTM Granule Timing Module

HBT Hanbury Brown-Twiss Interferometry

HPSS High Performance Storage System

LHC Large Hadron Collider

LL1 Local Level 1

LPM Landau-Pomeranchuk-Migdal (effect)

LVL-1 Level1-Trigger System

midd semiperipheral

MinBias Minimum Bias

MPC Muon Piston Calorimeter

MRPC Multi-Gap Resistive Plate

MuID Muon Identifier

MuTr Muon Tracker

PbGl Lead Glas

PbSc Lead Scintillator

PC Pad Chamber

PDF Parton Distribution Function

peri peripheral

PID Photon Identification

PHENIX Pioneering High Energy Nuclear Interactions Experiment

PMT Photo Multiplier

pQCD pertubative Quantum Chromodynamics

PRDF PHENIX Raw Data Format

RHIC Relativistic Heavy Ion Collider

RICH Ring-Imaging-Cherenkov

RxNP Reaction Plane Detector

semi semicentral

SM Standard Model

SMD Super Module

STAR Solenoidal Tracker at RHIC

SVD Silicon Vertex Detector

TEC Time-Expansion-Chamber

TOF Time of Flight

TPC Time-Projection Chamber

TRD Transition Radiation Detector

QCD Quantum Chromodynamics

QED Quantum Electrodynamics

QGP Quark Gluon Plasma

ZDC Zero-Degree-Calorimeter

Bibliography

[Ack03] K. H. Ackermann et al. *Nucl. Instrum. Meth.* **A499** (2003) 624.

[Ada03] M. Adamczyk et al. *Nucl. Instrum. Meth.* **A499** (2003) 437.

[Ada07] A. Adare et al. *Inclusive cross section and double helicity asymmetry for π^0 production in p+p collisions at $\sqrt{s}$=200 GeV: Implications for the polarized gluon distribution in the proton*. (2007). `0704.3599`.

[Adc02] K. Adcox et al. *Phys. Rev. Lett.* **88** (2002) 022301. `nucl-ex/0109003`.

[Adc03a] K. Adcox et al. *Nucl. Instrum. Meth.* ***A499*** (2003) 489.

[Adc03b] K. Adcox et al. *Nucl. Instrum. Meth.* ***A499*** (2003) 469.

[Adl00] C. Adler et al. *Nucl. Instrum. Meth.* ***A470*** *nucl-ex/0008005* (2000) 480.

[Adl03a] C. Adler et al. *Nucl. Instrum. Meth.* ***A499*** (2003) 560.

[Adl03b] S. S. Adler et al. *Physical Review Letters* **91** (2003) 072303.

[Adl03c] S. S. Adler et al. *Phys. Rev. Lett.* **91** (2003) 072301. `nucl-ex/0304022`.

[Adl07] S. S. Adler et al. *Physical Review Letters* **98** (2007) 172302.

[Adl08] S. Adler et al. *Physical Review C* **77** (2008) 014905.

[Aiz03] M. Aizawa et al. *Nucl. Instrum. Meth.* ***A499*** (2003) 508.

[Aki03] H. Akikawa et al. *Nucl. Instrum. Meth.* ***A499*** (2003) 537.

[All03] M. Allen et al. *Nucl. Instrum. Meth.* ***A499*** (2003) 549.

[Ant79] D. Antreasyan, J. W. Cronin, H. J. Frisch et al. *Phys. Rev. D* **19 3** (1979) 764.

[APDG09] C. Amsler (Particle Data Group) et al. *Physics Letters B667, 1 (2008) and 2009 partial update for the 2010 edition* .

[Aph03a] L. Aphecetche, T. Awes, S. Bathe et al. *PHENIX Internal Analysis Note AN203,* 2003 .

[Aph03b] L. Aphecetche et al. *Nucl. Instrum. Meth.* ***A499*** (2003) 521.

[Arn94] M. Arneodo. *Phys. Rep. 240* (1994) 301.

[Awe01a] T. Awes, S. Bathe, H. Buesching et al. *PHENIX Internal Analysis Note AN073,* 2001 .

[Awe01b] T. Awes, S.Bathe, H. Buesching et al. *PHENIX Internal Analysis Note AN069,* 2001 .

[Bac03] B. B. Back et al. *Nucl. Instrum. Meth.* **A499** (2003) 603.

[Bai97a] R. Baier, Y. L. Dokshitzer, A. H. Mueller et al. *Nuclear Physics B* **484** (1997) 265.

[Bai97b] R. Baier, Y. L. Dokshitzer, A. H. Mueller et al. *Nuclear Physics B* **483** (1997) 291.

[Bat03] S. Bathe, H. Buesching, C. Klein-Boesing et al. *PHENIX Internal Analysis Note 234,* 2003 .

[Bat05] S. Bathe, A. Bazilevsky and H. Buesching. *PHENIX Internal Analysis Note AN470,* 2005 .

[Bjo83] J. D. Bjorken. *Phys. Rev. D* **27 1** (1983) 140.

[BM96] P. Braun-Munzinger and J. Stachel. *Nuclear Physics A* **606** (1996) 320.

[BM07] P. Braun-Munzinger and J. Stachel. *Nature* ***448*** (2007) 302.

[BM09] P. Braun-Munzinger and J. Wambach. *Rev. Mod. Phys.* ***81*** (2009) 1032.

[Bow86] J. B. Bowlin and A. S. Goldhaber. *Phys. Rev. D* **34 3** (1986) 778.

[Bus84] W. Busza and A. Goldhaber. *Phys. Lett. 139B, 234* (1984) .

[Cas98] C. Caso et al. *Eur. Phys. J.* **C3** (1998) 1.

[Cha32] J. Chadwick. *Nature 129* (1932) 312.

[Che03] S. Chekanov, D. Krakauer, S. Magill et al. *Phys. Rev. D* **67 1** (2003) 012007.

[Chi07] M. Chiu. *Single Spin Transverse Asymmetries of Neutral Pions at Forward Rapidities in sqrt(s) = 62.4 GeV Polarized Proton Collisions in PHENIX*. 2007.

[Cho74] A. Chodos, R. L. Jaffe, K. Johnson et al. *Phys. Rev. D* **9 12** (1974) 3471.

[Cot07] W. Cottingham and D. Greenwood. *An introduction to the standard model of particle physics*. Cambridge University, 2007.

[Cre77] M. Creutz. *Phys. Rev. D* **15 4** (1977) 1128.

[Cro75] J. Cronin et al. *Production of hadrons at large transverse momentum at 200, 300, and 400 GeV*, Band 11. 1975.

[CVS09] PHENIX CVS Repository /offline/framework/fun4all/, 2009.

[d'E04] D. d'Enterria. *PHENIX Internal Analysis Note AN322,* 2004 .

[d'E09] D. d'Enterria. *arXiv:0902.2488v1 [nucl-ex]* textit Jet quenching in QCD matter: from RHIC to LHC, 2009.

[Dem05] W. Demtröder. *Experimantalphysik 4 Kern-, Teilchen- und Astrophysik*. 2005.

[Dre70] S. D. Drell and T.-M. Yan. *Phys. Rev. Lett.* **25 5** (1970) 316.

[Dre03] A. Drees, T. Hemmick, B. Jacak et al. *PHENIX Internal Analysis Note 210,* 2003 .

[Gei13] H. Geiger and E. Marsden. *Phil. Mag. 25,* 1913 .

[GM64] M. Gell-Man. *Physics Letters 8 (3): 214-215,* 1964 .

[Gre64] O. W. Greenberg. *Phys. Rev. Lett.* **13 20** (1964) 598.

[Gro73] D. J. Gross and F. Wilczek. *Phys. Rev. Lett.* **30 26** (1973) 1343.

[Gyu94] M. Gyulassy and X.-N. Wang. *Nuclear Physics B* **420** (1994) 583.

[Hag84] R. Hagedorn. *Riv. Nuovo Cim.* **6N10** (1984) 1.

[Ian03] E. Iancu and R. Venugopalan. *The Color Glass Condensate and High Energy Scattering in QCD*, 2003.

[Kar00] F. Karsch. *Nuclear Physics B - Proceedings Supplements* **83** (2000) 14.

[Kar02] F. Karsch. *Lect. Notes Phys.* **583** (2002) 209.

[KB00] C. Klein-Boesing. *Simulation der Detektoreigenschaften des Bleiglaskalorimeters in den Experimenten WA98 and PHENIX*. Diplomarbeit, 2000.

[KB03] C. Klein-Boesing, K. Reygers, T.Awes et al. *PHENIX Internal Analysis Note AN167,* 2003 .

[KB04] C. Klein-Boesing. *Production of Neutral Pions and Direct Photons in Ultra-Relativitic Au+Au collisions*. Dissertation, 2004.

[Kha02] D. E. Kharzeev and J. Raufeisen. *High energy nuclear interactions and QCD: an introduction*, 2002.

[Lev98] E. Levin. *An introduction to Pomerons*, 1998.

[Lov09] B. T. Love. *The Design, Implementation and Performance of the PHENIX Time-of-Flight West Detector*. Diplomarbeit, Vanderbilt University, Nashville TN, 2009.

[Mer09] B. Meredith. *Probing High Parton Densities at Low-x in d+Au Collisions at PHENIX Using the New Forward and Backward Muon Piston Calorimeters*. Dissertation, 2009.

[Mik09] K. Miki. *Azimuthal Anisotropy Measurement of Neutral Pion and Direct Photon in* $\sqrt{s}_{NN}$ *= 200 GeV Au + Au Collisions at RHIC-PHENIX*. Dissertation, University of Tsukuba, 2009.

[Mil07] M. L. Miller, K. Reygers, S. J. Sanders et al. *Glauber Modeling in High Energy Nuclear Collisions*, 2007.

[Nag09] J. Nagle. *PHENIX analysis note AN844,* 2009 .

[Nam60] Y. Nambu. *Phys. Rev. Lett.* (1960) 380.

[Nam61a] Y. Nambu and G. Jona-Lasinio. *Phys. Rev.* **122 1** (1961) 345.

[Nam61b] Y. Nambu and G. Jona-Lasinio. *Phys. Rev.* **124 1** (1961) 246.

[Pei97] T. Peitzmann. *Kernmaterie unter extremen Bedingungen - Die experimentelleSuche nach dem Quark-Gluon-Plasma*. Muenster, 1997. Habilitation.

[phe09] https://www.phenix.bnl.gov/WWW/run/drawing/, 2009.

[Pil00] G. Piller and W. Weise. *Phys. Rep. 330* (2000) 1.

[Pol73] H. D. Politzer. *Phys. Rev. Lett.* **30 26** (1973) 1346.

[Pov06] B. Povh, K. Rith, C. Scholz et al. *Teilchen und Kerne*. Heidelberg, 2006.

[Rey03a] K. Reygers. *PHENIX Internal Analysis Note AN169,* 2003 .

[Rey03b] K. Reygers, C. Klein-Boesing, T. Awes et al. *PHENIX Internal Analysis Note AN175,* 2003 .

[Rey04] K. Reygers. *Die Suche nach dem Quark-Gluon-Plasma mit dem PHENIX-Experiment am RHIC*. Muenster, 2004. Habilitation.

[Sjo94] T. Sjostrand. *Comput. Phys. Commun.* **82** (1994) 74.

[Sus03] Susumu. *"http://www.phenix.bnl.gov/WWW/upgrades/highpt" Conceptual Design Report for High pt Upgrade,* 2003.

[Tan03] M. Tannenbaum. *PHENIX Internal Analysis Note AN209,* 2003 .

[Tho01] A. Thomas and W. Weise. *The Structure of the Nucleon*. WILEY-VCH, Berlin, 2001.

[Vel05] J. Velkovska et al. *"http://phenix.vanderbilt.edu/tofw/CDR tofw.doc" Conceptual Design Report: Multi-gap Resistive Plate Chambers: Time-of-Flight system of the PHENIX high-pT Detector,* 2005.

[Wes09] J. Wessels and C. Klein-Boesing. *Vorlesung: Quarks, Gluons, and the Quark-Gluon Plasma*. Institut fuer Kernphysik, Universitaet Muenster, 2009.

[Won94] J. Wong. *Introduction to High-Energy Heavy-Ion Collisions*. World Scientific, 1994.

[Woo54] R. D. Woods and D. S. Saxon. *Phys. Rev.* **95 2** (1954) 577.

[Yag05] K. Yagi, T. Hatsuda and Y. Miake. *Quark-Gluon Plasma*. Cambridge University Press, 2005.

[Yan54] C. N. Yang and R. L. Mills. *Phys. Rev.* **96 1** (1954) 191.

[Zau07] O. Zaudtke. *Measurement of Direct-Photon Production and Neutral Pion Double Helicity Asymmetry in Ultra-Relativistic p + p Collisions*. Dissertation, 2007.

[Zha04] C. Zhang and J. Nagle. *PHENIX Internal Analysis Note AN342,* 2004 .

[Zwe64a] G. Zweig. *An SU(3) Model for Strong Interaction Symmetry and its Breaking*. 1964. CERN Report No.8181/Th 8419.

[Zwe64b] G. Zweig. *An SU(3) Model for Strong Interaction Symmetry and its Breaking: II*. 1964. CERN Report No.8419/Th 8412.

Danksagung

Abschließend möchte ich mich bei denjenigen Personen bedanken, die maßgeblich zu dem Gelingen dieser Arbeit beigetragen haben.
Mein Dank gilt allen voran Herrn Prof. Dr. Johannes P. Wessels, für die Möglichkeit in der Arbeitsgruppe zu arbeiten, für das aufregende Thema und den spannenden Aufenthalt am BNL.
Bei Dr. Baldo Sahlmüller möchte ich mich ganz besonders für die unermütliche Unterstützung und Betreuung der Arbeit, für die Beantwortung zahlreicher Fragen und allem was ich durch Ihn gelernt habe bedanken. Außerdem bedanke ich mich bei Dr. Christian Klein-Bösing, der mir immer mit hilfreichen Ratschlägen und Anregungen zur Seite stand und bei Dr. Klaus Reygers, der grundlegend zum Thema der Diplomarbeit beigetragen hat.
Dr. Stefan Bathe danke ich für die vielen Erklärungen rund um das Experiment.
Für den angenehmen Aufenthalt in Brookhaven gilt mein Dank Dr. Christoph Baumann und Dr. Baldo Sahlmueller. Des Weiteren möchte ich der "Photon Working Group" des PHENIX Experiments für die kritische Auseinandersetzung mit vielen Fragestellungen meinen Dank aussprechen.
Meinen Bürokollegen danke ich für die nette und freundschaftliche Stimmung: Jonas Anielski, Stefan Korsten, Michael Kowalik, Eva Sicking, Svenja Wulff und Andrea Nustede. Für die gute Arbeitsatmosphäre in der Arbeitsgruppe im Institut für Kernphysik möchte ich mich bei allen aktuellen und ehemaligen Mitglieder bedanken: Björn Albrecht, Jonas Anielski, Bastian Bathen, Dr. Christoph Baumann, Cyrano Bergmann, Dr. Tom Dietel, David Emschermann, Henriette Gatz, Holger Gottschlag, Markus Heide, Dr. Matus Kalisky, Dr. Melanie Klein-Bösing, Dr. Christian Klein-Bösing, Stefan Korsten, Michael Kowalik, Friederike Poppenborg, Markus Rammler, Dr. Baldo Sahlmüller, Eva Sicking, Anton Sperling, Don Vernekohl, Matthias Walter, Uwe Westerhoff, Alexander Wilk und Svenja Wulff.

Des Weiteren bedanke ich mich für die kritische Durchsicht und Korrektur der Arbeit bei Dr. Baldo Sahlmüller, Dr. Christian Klein-Bösing, Sally Bennett und Rilana Müller.

Ein ganz besonderer Dank gilt meinen Eltern und meiner Familie, die mich während meines gesamten Studiums immer unterstützt und mich in all meinen Entscheidungen bestärkt haben. Ohne sie wäre dies nicht möglich gewesen. Vielen Dank!!!

Außerdem danke ich all meinen Freunden, die immer für die nötige Ablenkung während des Studiums gesorgt haben. Danke für die gemeinsamen Parties, Urlaube, und alle weiteren Erlebnisse, die ich mit Euch teilen durfte. Auch allen Mitgliedern vom Capoeira Verein Biriba Brasil danke ich für den sportlichen Ausgleich zum Studium durch das tolle Training und die vielen guten Rodas. Axé!

Rilana danke ich für Ihre Unterstützung, Aufmunterung und alle gemeinsamen Erfahrungen während der letzten Jahre. Danke!

Eigenständigkeitserklärung

Hiermit versichere ich, dass ich diese Arbeit selbstständig verfasst und keine anderen als die angegebenen Hilfsmittel und Quellen verwendet habe.

Münster, 15. Februar 2010

Sebastian Klamor